NATIONAL AND KAPODISTRIAN UNIVERSITY OF ATHENS

SCHOOL OF SCIENCE
DEPARTMENT OF INFORMATICS AND TELECOMMUNICATION
INTERDEPARTMENTAL MSc PROGRAM IN MICROELECTRONICS

MSc THESIS

Study of non-linear dynamics in Quantum Dot Lasers for Neuromorphic Processing

Georgios C. Sarantoglou

Supervisor: **Charis Mesaritakis,** Associate Professor, University of the Aegean

ATHENS

FEBRUARY 2022

ΕΘΝΙΚΟ ΚΑΙ ΚΑΠΟΔΙΣΤΡΙΑΚΟ ΠΑΝΕΠΙΣΤΗΜΙΟ ΑΘΗΝΩΝ

ΣΧΟΛΗ ΘΕΤΙΚΩΝ ΕΠΙΣΤΗΜΩΝ
ΤΜΗΜΑ ΠΛΗΡΟΦΟΡΙΚΗΣ ΚΑΙ ΤΗΛΕΠΙΚΟΙΝΩΝΙΩΝ

ΔΙΑΤΜΗΜΑΤΙΚΟ ΠΡΟΓΡΑΜΜΑ ΜΕΤΑΠΤΥΧΙΑΚΩΝ ΣΠΟΥΔΩΝ ΣΤΗ ΜΙΚΡΟΗΛΕΚΤΡΟΝΙΚΗ

ΔΙΠΛΩΜΑΤΙΚΗ ΕΡΓΑΣΙΑ

Μελέτη μη γραμμικών δυναμικών σε λέιζερ κβαντικών τελειών για χρήση τους ως νευρομορφικοί επεξεργαστές

Γεώργιος Χ. Σαράντογλου

Επιβλέπων: **Χάρης Μεσαριτάκης,** Αν. Καθηγητής Πανεπιστήμιο Αιγαίου

ΑΘΗΝΑ

ΦΕΒΡΟΥΑΡΙΟΣ 2022

MSc THESIS

Study of non-linear dynamics in Quantum Dot Lasers for Neuromorphic Processing

Georgios C. Sarantoglou
S.N.: MM284

SUPERVISOR: **Charis Mesaritakis,** Associate Professor, University of the Aegean

ΔΙΠΛΩΜΑΤΙΚΗ ΕΡΓΑΣΙΑ

Μελέτη μη γραμμικών δυναμικών σε λέιζερ κβαντικών τελειών για χρήση τους ως νευρομορφικοί επεξεργαστές

Γεώργιος Χ. Σαράντογλου

Α.Μ.: ΜΜ284

ΕΠΙΒΛΕΠΩΝ: **Χάρης Μεσαριτάκης,** Αν. Καθηγητής Πανεπιστήμιο Αιγαίου

ABSTRACT

This thesis studies the quantum dot lasers from the scope of neuromorphic processors. Neuromorphic processors are a new generation of processors which contrary to conventional devices, its architecture does not consist of two separate systems for processing and memory, but it has a different form that assimilates the neural system of living beings. The neural system in human and other animals is significantly efficient when it performs operations related to cognition and decision making. Such functionality is extremely important for artificial intelligence, with neuromorphic processors being the ideal paradigm to support future intelligent systems.

Although photonics is of fundamental importance in telecommunication systems, since Internet is based on technologies such as the laser and optical fibers, this area has not achieved similar remarkable results with respect to information processing, which is based exclusively on electronics. Due to increased necessity for neuromorphic computers, the similarity between the laser and the biological neurons has become the object of many new studies. Lasers have properties similar to biological neurons but in a different time scale that is 1000000 times smaller, which renders them ideal for cognitive processing of high bandwidth signals.

In this work, a special laser that is based on the technology of quantum dots is studied. Quantum dots contrary to other active materials can lead to lasing silicon devices by creating silicon substrates carefully doped with quantum dots. Additionally, quantum dot lasers have lower energy consumption compared to other lasers and they have the ability to generate coherent light from multiple quantum states.

For these reasons, in this work a detailed mathematical study of the quantum dot laser under optical injection takes place from the viewpoint of non-linear systems theory, in order to highlight their neural properties. Under this mathematical prism, the similarity between the quantum dot lasers and the biological neurons is examined. The mathematical analysis focuses on the ability of the quantum dot laser for multi-waveband emission and provides useful conclusions for the deployment of the quantum dot laser neuron in a large neural system consisting of multiple neuromorphic nodes for cognitive processing at the speed of light.

ΠΕΡΙΛΗΨΗ

Η συγκεκριμένη διπλωματική εργασία αφορά την μελέτη ενός λέιζερ κβαντικών τελειών για χρήση του ως νευρομορφικός επεξεργαστής. Οι νευρομορφικοί επεξεργαστές είναι μια νέα οικογένεια επεξεργαστών που σε αντίθεση με του τυπικούς επεξεργαστές που συναντώνται στα σημερινά υπολογιστικά συστήματα, η αρχιτεκτονική τους δεν στηρίζεται σε δύο ξεχωριστά συστήματα επεξεργασίας και μνήμης, αλλά παίρνοντας έμπνευση από τον χώρο της νευροεπιστήμης μιμείται τον σχεδιασμό του νευρικού συστήματος των έμβιων όντων. Το νευρικό σύστημα στον άνθρωπο αλλά και τα υπόλοιπα ζώα είναι εξαιρετικά αποδοτικό όταν εκτελεί λειτουργίες που σχετίζονται με την νόηση και την λήψη αποφάσεων, Τέτοιες λειτουργίες είναι εξαιρετικά σημαντικές για τον κλάδο της τεχνητής νοημοσύνης με τους νευρομορφικούς επεξεργαστές να αποτελούν την ιδανική αρχιτεκτονική για την υποστήριξη μελλοντικών ευφυών συστημάτων.

Ενώ η επιστήμη της φωτονικής είναι εξαιρετικά σημαντική για τα τηλεπικοινωνιακά συστήματα, με το διαδίκτυο να στηρίζεται εξολοκλήρου σε τεχνολογίες όπως τα λέιζερ και οι οπτικές ίνες, δεν συναντάται ανάλογη προσφορά στον τομέα της επεξεργασία των δεδομένων, που γίνεται εξολοκλήρου από ηλεκτρονικές συσκευές. Με την ανάγκη όμως για νευρομορφικούς επεξεργαστές, έχει αναδειχτεί τα τελευταία χρόνια η ομοιότητα ανάμεσα στα λέιζερ και τους βιολογικούς νευρώνες. Τα λέιζερ εμφανίζουν αντίστοιχες ιδιότητες, σε χρονική κλίμακα που είναι 1000000 φορές μικρότερη από εκείνη των νευρώνων, καθιστώντας τα ιδανικά για την επεξεργασία υψίρυθμων σημάτων.

Στην δουλειά αυτή μελετάται υπό αυτό το πρίσμα μια ειδική μορφή λέιζερ που στηρίζεται στην τεχνολογία κβαντικών τελειών. Οι κβαντικές τελείες σε αντίθεση με άλλα ενεργά υλικά για την παραγωγή φωτός, μπορούν να εμποτιστούν στο πυρίτιο δίνοντας για πρώτη φορά την δυνατότητα να παραχθεί φως από διατάξεις πυριτίου, έχει χαμηλότερες ενεργειακές απαιτήσεις σε σχέση με άλλα λέιζερ και μπορεί να παράγει φως από πολλαπλές κβαντικές στάθμες.

Για αυτούς του λόγους σε αυτή την διπλωματική εργασία πραγματοποιείται για πρώτη φορά μια ενδελεχής μαθηματική ανάλυση ενός λέιζερ κβαντικών τελειών σε τοπολογία οπτική έγχυσης, από την σκοπιά της θεωρία μη γραμμικών συστημάτων με στόχο την ανάδειξη των νευρωνικών του ιδιοτήτων. Υπό αυτό το μαθηματικό πρίσμα εξετάζεται η ομοιότητα αυτού του φωτονικού νευρώνα με τους βιολογικούς νευρώνες. Η μαθηματική ανάλυση δίνει ιδιαίτερη προσοχή στην δυνατότητα των λέιζερ κβαντικών τελειών για παραγωγή φωτός από πολλαπλές ενεργειακές στάθμες και εξάγει χρήσιμα συμπεράσματα για τον μελλοντικό συνδυασμό αυτού του φωτονικού νευρώνα με άλλους παρόμοιους νευρώνες για την υλοποίηση σύνθετων γνωσιακών λειτουργιών με την ταχύτητα του φωτός.

Αφιερώνεται στους γονείς μου και στην αδελφή μου,

Χρήστο, Λένα και Βίκυ

ΕΥΧΑΡΙΣΤΙΕΣ

CONTENTS

LIST OF FIGURES

Information flows from axons via active synapses to neurons. Neuron behaviors are individually programmable, with two examples shown. (h) Functional chip architecture is a two-dimensional array of cores where long-range connections are implemented by sending spike events(packets) over a mesh routing network to activate a target axon. Axonal delay is implemented at the target. (i) Routing network extends across chip boundaries through peripheral merge and split blocks. (j) Physical layout of core in 28-nm CMOS fits in a $240\,\mu m$ -by- $390\,\mu m$ footprint. A memory (static random-access memory) stores all the data for each neuron, a time-multiplexed neuron circuit updates neuron membrane potential, a scheduler buffers incoming spike events to implement axonal delays, a router delays spike events, and an event-driven controller orchestrates the core's operation. (k) Chip layout of 64-by-64 core array, wafer, and chip package. (l) Chip periphery to support multichip networks. I/O. input/output [20]..............................29

Figure 1-10 : Differences in time scales between biological neurons (left), current electronic neurons (middle) and photonic neurons (right) [12]......................................30

Figure 1-11 : The experimental implementation of an all optical SNN based on MRRs and PCMs [36]...32

Figure 1-12 : (a) The 2-layered topology used in the experiment. This system is used 4 times so as to implement the desired neural network. An instance is a weight matrix implemented with MZIs, whereas the non-linear activation function is achieved by simulating a saturable absorber on a conventional computer. (b) The experimental feedback and control loop used in the experiment. (c) A MZI which is configured by modifying the phase delay. It can be seen that its re-configuration, which is achieved by changing the applied voltage, results in a change of the light transmission. (d) The photonic chip used in the experiment. The colors illustrate the propagation path of the 4 inputs (red) towards the 4 outputs (light blue) [31]..33

Figure 2-1 : The flow of a two-dimensional system starting from the initial condition $X = x0, y0$ [15]...34

Figure 2-2 : State space diagrams for (a) a stable node, (b) an unstable node [47]. 37

Figure 2-3: A saddle node equilibrium in (a) z- coordinates, (b) X – coordinates [47]. ..38

Figure 2-4: State space diagrams for (a) a stable focus, (b) an unstable focus, (c) a center [47]...38

Figure 2-5: The state space diagram for (a) $\lambda 1 < 0$ and (b) $\lambda 2 > 0$ [47]. 39

LIST OF TABLES

No table of figures entries found.

INTRODUCTION

The theoretical results that are presented in this thesis have been performed in the department of Informatics and Telecommunications of the National and Kapodistrian University of Athens.

1. NEUROMORPHIC COMPUTING

1.1 Neuromorphic Engineering

Of the various phenomena observed in nature, one of the most intriguing is that of emergence [1], [2]. Emergence is a term that refers to the ability of multi-part systems to spontaneously generate global and complex behaviors. Some notable examples are : social interactions between large populations [3], physical processes such as protein folding [4], and biological systems such as the human brain [5]. It can be understood from this comprehensive list, that complexity in nature and emergence are two terms that are strongly related. Although the study of such systems is a crucial goal for a variety of scientific fields such as physics, biology, medicine and sociology, the technological means that are currently in our disposal to tackle such tasks are highly inefficient. Moreover, it is highly desirable not only to study such systems but also to emulate them, thus harnessing their strength for the development of new groundbreaking technologies. Software-based solutions are currently being developed to tackle such tasks, but since they run on traditional von – Neumann architectures they face fundamental limitations. The origin of such limitations can be found in the hardware architecture; the physical distance between the memory where the data is stored and the processor, where information is processed. The transferring of data back and forth from the memory to the processor is a highly demanding task that not only sets a limit to the processing speed but also requires huge storage facilities. Considering both ecological and economic factors the development of energy efficient hardware that is capable to handle such tasks is highly important.

To this scope, researchers have turned their focus towards the most complex and computationally efficient system in the known universe, namely the human brain. The human brain consists of approximately 10^{11} neurons, with each neuron forming up to 10,000 connections with other neurons. Neurons communicate with each other via as many as 10^{15} synaptic connections. With respect to computational efficiency, it is impressive that the human brain is able to perform between 10^{13} and 10^{16} operations per second while consuming only 25 W [6]. Such exceptional performance is linked mainly to the neuron biochemistry, its underlying dynamical structure and the biophysics of neuronal computational algorithms. These remarkable results have given rise to the field of neuromorphic computing, where brain – inspired algorithms and architectures are developed as an alternative to traditional computer solutions.

Conventional computers are based on the von – Neumann architecture [7] (also known as the Princeton architecture). As shown in Figure 1-1, it consists of a memory that stores both data and instructions, a central processor unit (CPU), inputs and outputs. From this scheme emerges the von – Neumann bottleneck [8] which fundamentally limits the performance of computing tasks. This is a problem that becomes much more important as the speed of CPUs increases and memory units get larger. The von – Neumann paradigm has been successfully used for over 50 years, by satisfying both the Moore's [9] and the Koomey's law [10] for energy efficiency (multiply – accumulate operations (MAC) per joule). Unfortunately, as it is shown by recent studies, the Kommey's law is reaching a plateau meaning that in the recent years conventional computing schemes are unable to meet the increasing computational demands (see Figure 1-2). The computation efficiency levels off below 10 MMAC/mW (or 10 GMAC/W or 100 pJ per MAC) [11]. The reasons behind this trend can be traced in the way information is represented in traditional schemes and the relationship between the processing and memory in an architectural level.
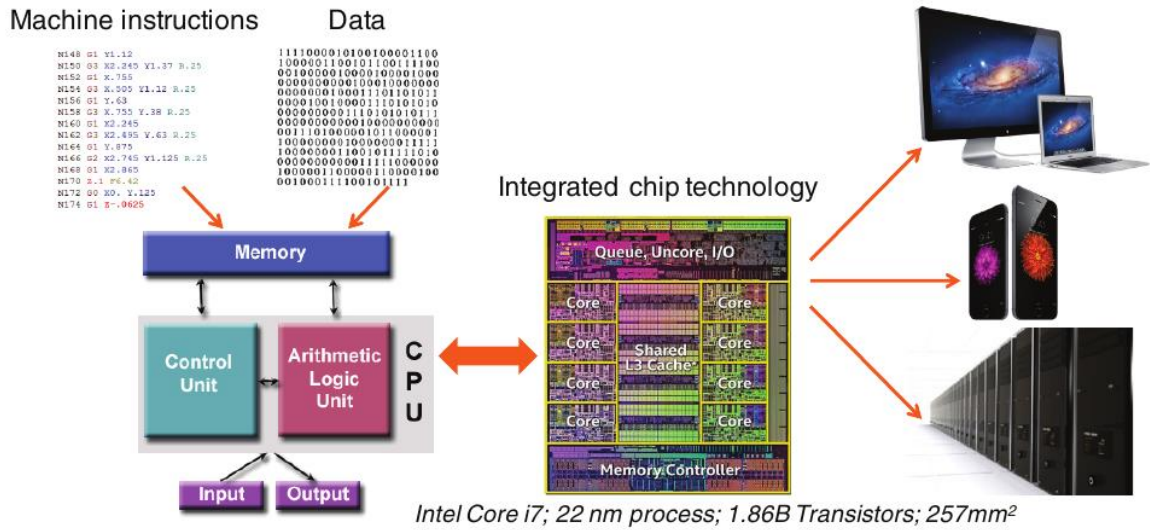
Figure 1-1: Conventional Von - Neumann architecture. Memory stored data and instructions, whereas the central processor unit processes the data. The physical distance between these two units causes fundamental processing [12].
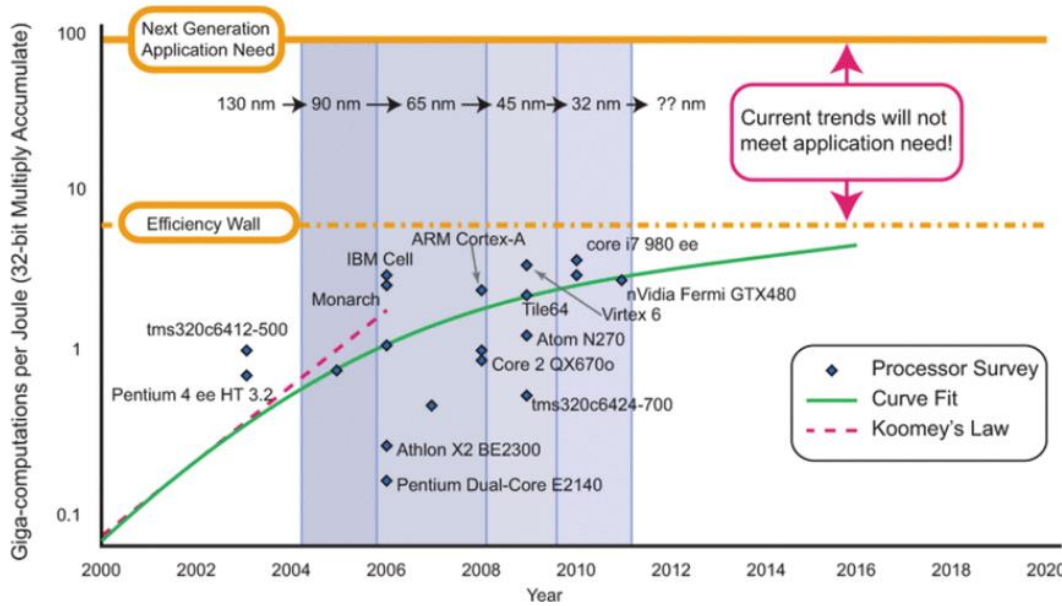
Figure 1-2 : The energy efficient in giga multiply - accumulated per Joule versus year. The MAC operations are normalized to 32-bit size computation. It can be seen that since 2005 the Koomey's law for energy efficiency does not hold, whereas current processing schemes are unable to efficiently meet the modern demands [13].

With respect to Moore's law, it is known that the CMOS technology has reached its limit in terms of the its physical size. For example, although physical narrowing of the gate oxide, whose role is to separate as an insulator the gate from the channel, down to 1.2 nm (5 atoms thick layer) permits higher conductivity, it gives rise to current leakage due to the quantum tunneling effect [14]. This leakage leads to increased power consumption. Combining these results with the fact that biological systems reach efficiencies as low as 1aJ per MAC, which is eight orders of magnitude lower than the efficiency limit of conventional computational systems - 100 pJ per MAC - reveals the importance of developing new biology inspired architectures so as to meet the ever-increasing societal demands.

To this scope, the field of neuromorphic engineering has emerged, where brain inspired components are designed along with new radical algorithms that can efficiently process huge amount of data by leveraging the inherent parallelism of neural structures. These architectures bridge the gap between the physical world and the processing procedure, while promising extraordinary results in domains such as machine vision and speech recognition with very low power consumption.

1.2   The biological neuron

The neuron is arguably the most important concept in brain science and it is also the basic block used by the field of neuromorphic engineering to build complex, energy efficient unconventional computing schemes. A basic sketch of the biological neurons is illustrated in Figure 1-3. The neuron receives input by other neurons by the dendritic tree through contacts known as synapses. The inputs (which can be up to 10,000) produce transmembrance currents known also as synaptic currents that cause changes in the membrane potential of the neuron. These changes are known as post-synaptic potentials (PSP). Large synaptic currents can cause the triggering of voltage-sensitive channels upon the neuron membrane. Such triggering is able to generate a large membrane potential of relatively constant amplitude that propagates through the axon to other neurons. This is the activation potential and it travels in the form of a spike event.
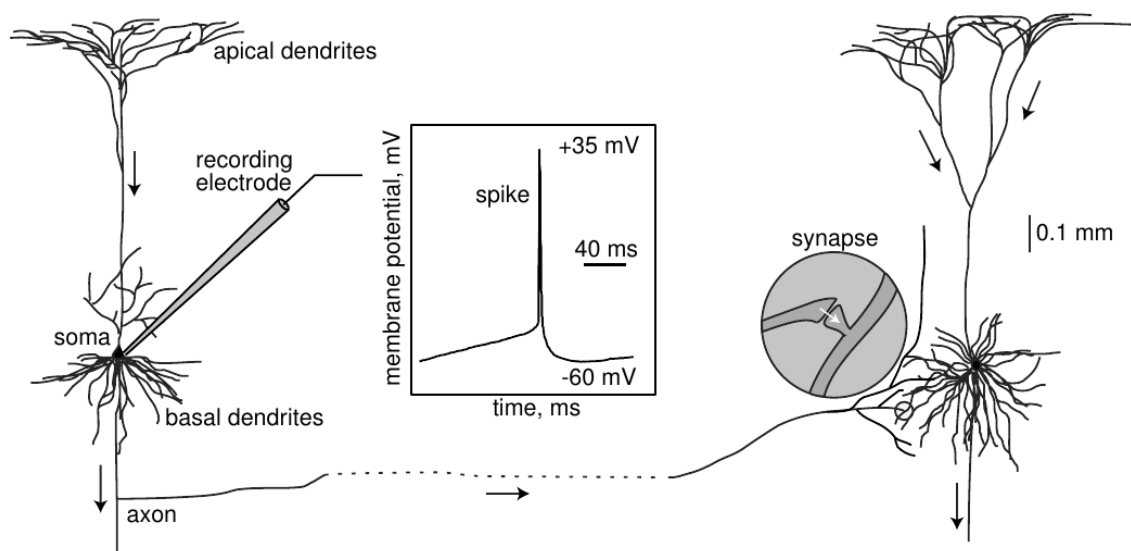
Figure 1-3: The connection between two cortical pyramidal neurons [15].

The simplest explanation of the operation of a biological neuron and the most famous one in introductory neuroscience books is given by the leaky integrate and fire neuron (LIF). The behavior of this neuron can be summarized in Figure 1-4. The neuron's inputs are weighted, which means that the spike amplitudes are multiplied by a certain real value w_j, $j = 1 \dots N$, where the index j denotes the j-th pre-synaptic neuron. If a weight holds the 0 value, then it is said that there is no connection between the main neuron and the respective pre-synaptic one. Moreover, all the inputs are delayed by τ_j, a fact that reflects the delay imposed by the propagation of spike events up to the neuron's membrane in the form of PSPs. The neuron integrates the sum of all weighted and delayed synaptic currents, thus increasing its transmembrane potential y. When it receives no inputs, it tends to return to its resting state which is connected to a certain transmembrane potential and takes values around -60 mV. As a result, there are two opposing forces, the incoming spikes that tend to increase the transmembrane potential and the relaxation mechanism that tends to decrease it. However, if the total

transmembrance potential at a given instance overcomes a certain threshold value, then the neuron is said to be excited and its potential rapidly increases, reaching values as high as 40 mV. Then inhibitory mechanisms drive the system output back to its resting state. The outcome is the formation of a spike event. Above the threshold, additional inputs are unable to increase the neuron's output for a specific time window known as the refractory period.
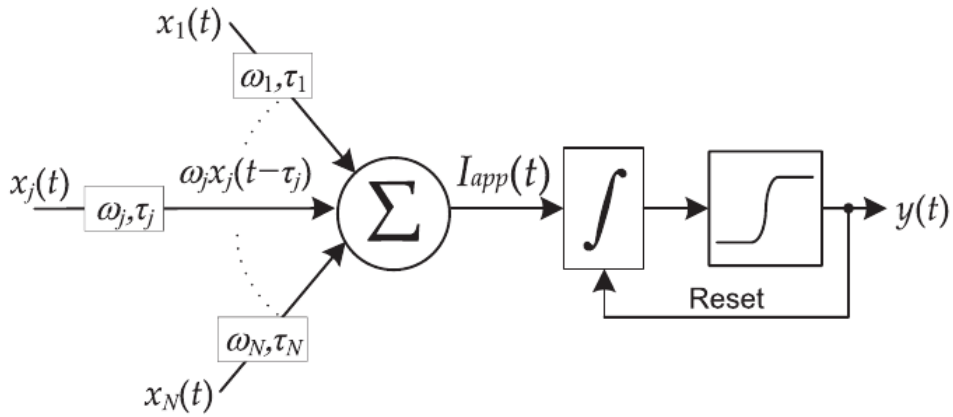
Figure 1-4: The operation of a leaky integrate and fire neuron [12].

A mechanistic view of this process is given in Figure 1-5 . The y axis in this case is inverted meaning that upwards it points to negative values, whereas downwards it points to positive ones.
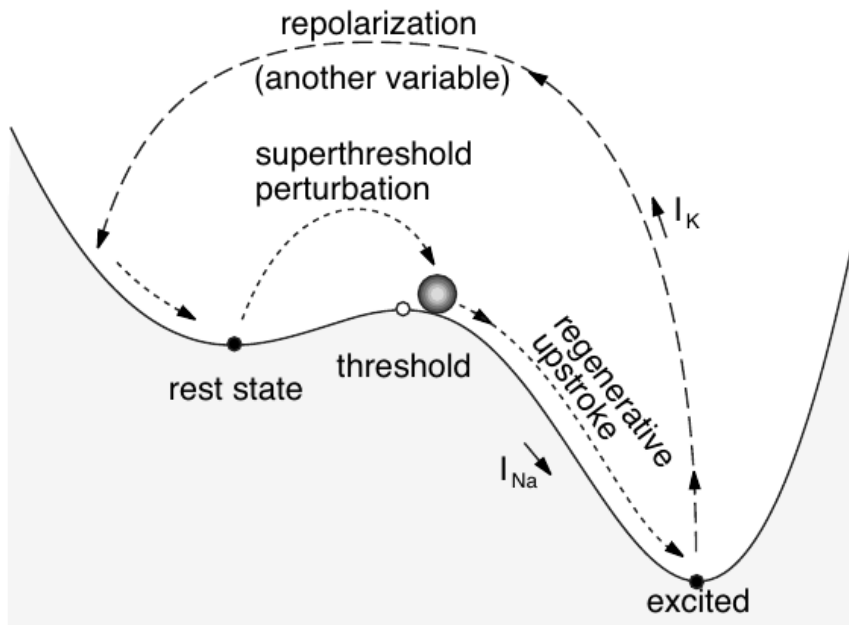
Figure 1-5 : A mechanistic view of the neuron's behavior [15].

1.3 The three generations of neuromorphic systems

Computer scientist have tried to extract from the picture of the biological neuron, the key characteristics that would allow them to exploit its potential. Although neuromorphic systems are currently under a remarkable development, their origin can be traced back to 1943, when Warren McCulloch and Walter Pitts proposed the first artificial neuron known as the perceptron or the threshold – logic unit [16]. The history of neuromorphic systems can be separated according to Maass [17] in three generations, with each generation adding more characteristics of the biological neuron.

The first and second generations use the model that is illustrated in Figure 1-6. The inputs are multiplied by weights and summed along with a bias value that is used so as to regulate the threshold value. The weights can take both positive and negative values indicating excitatory and inhibitory connections. The result is inserted in a non-linear function known as the activation function. The mathematical description is given by Eq. (1-1).

$$y = \phi\left(\sum_{k=1}^{N} w_k x_k\right)$$
(1-1)
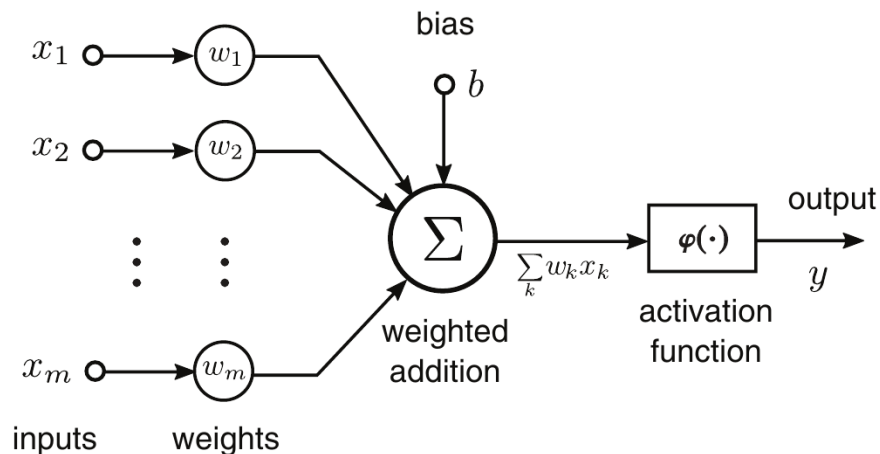
Figure 1-6 : Nonlinear model of an artificial neuron [12].

The distinction between the first and the second generations is made in terms of the activation function, which is usually bounded and monotonic. This distinction is shown in Figure 1-7. In the first generation, the activation function is a simple Heaviside function and the artificial neuron is known as perceptron. If the input is greater than zero then the neuron is said to be above threshold and takes the value 1, otherwise it is 0. Perceptrons can be used in order to implement any boolean circuit and thus they are universal for digital circuits. The second generation implements the activation function by introducing a continuous range of output values. In other words, the output is made analog. Neural networks that consist of artificial neurons with continuous non-linearity have the ability to perform any analog computation.

In order to introduce the third generation, it is important to notice a fundamental difference between the artificial neuron in Figure 1-6 and the biological neuron. Although the biological neuron transmits discrete spatio-temporal spike events, the artificial neurons broadcast continuous values. The reason is that neuroscientists

initially believed that information is encoded in the firing rate of neurons [18]. According to Hodgkin [19], as the power of the input applied at the neuron's synapses increases, its firing rate increases as well. This fact is illustrated in measurements for layer 5 pyramidal neurons from the rat primary virtual cortex [15] in Figure 1-8. By comparing Figure 1-8 and Figure 1-7 it can be seen that second-generation non-linear functions try to mimic the firing rate versus triggering strength relation.
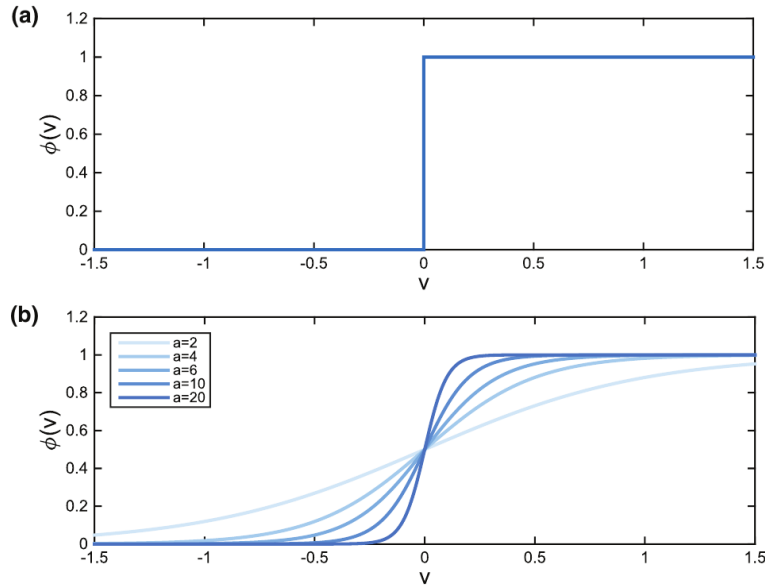
Figure 1-7 : (a) The step-like Heaviside non-linear function used by the neural networks of the first generation. (b) The sigmoid function, which is a conventional option as a continuous valued non-linearity. It is described by $\sigma(x) = [1 + exp(-ax)]^{-1}$. As the parameter a converges to infinity, the sigmoid function converges to the Heaviside [12].
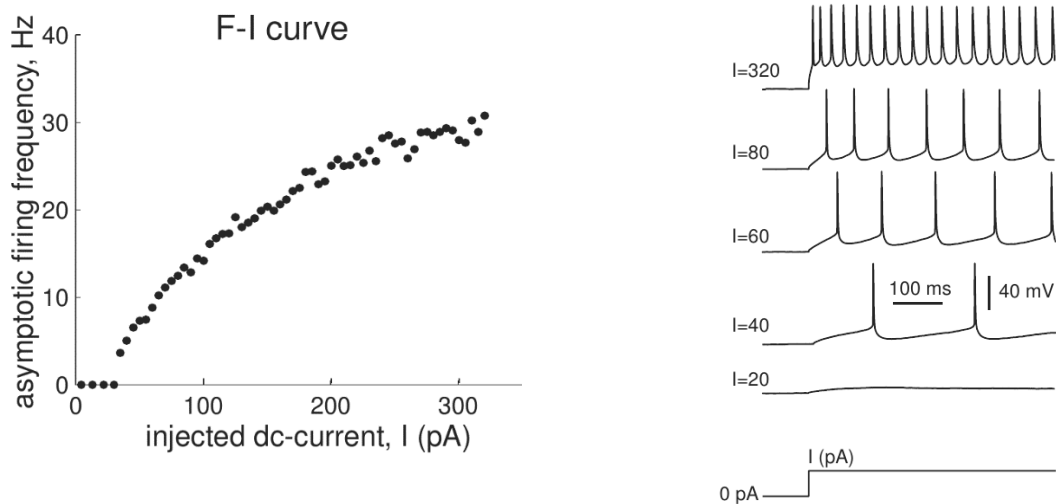
Figure 1-8: (Left) Experimental recording of the firing rate versus the applied DC current for layer 5 pyramidal neurons from the rat primary virtual cortex. (Right) Illustration of the increasing firing rate as a function of the applied DC current [15].

However, experimental results from the field of neuro-science reveal that this approach is rather simplistic and cannot provide a satisfactory explanation to fundamental biological functions such as vision. For example, the primitive brain recognizes 3D

objects such as faces, places, food, etc. in a time period as short as 150 ms. Since visual information must pass 10 neural layers in order to be decoded, this means that each neuron must fire at approximately 10 ms or less. Since neurons rarely fire at frequencies much above 100 Hz, this means that at 150 ms the neurons will have the time to fire at most one spike. It is unlikely that the firing rate of each neuron can be deduced by a single spike event and then used from the subsequent neural layers as it is done in artificial neural networks (ANN) [18]. It can be seen, that using the rate encoding scheme represents a computational bottleneck and different encoding mechanisms must be considered so as to effectively describe the neuro-computational power of biological systems.

The third generation of ANNs takes into account these considerations and utilizes hardware units that are capable of generating discrete spike events. These units are developed so as to mimic the functionality of the biological neurons and for this reason they are called neuromorphic, which gives rise to the field of neuromorphic engineering. These artificial neurons are known as spiking neurons and the ANNs that are composed by such neurons are known as spiking neural networks (SNN). SNNs in contrast to conventional ANNs can perform computational tasks by using different encoding schemes like rank order encoding, temporal encoding, synchronicity based encoding, etc [18]. Spiking neurons due to their complexity cannot be described by an equation similar to (1-1). In contrast, they are mathematically described by non-linear systems, which have the form seen in (1-2) [12], [15].

$$\frac{dX}{dt} = F(X; \Omega), \;\; X \in A_x \subset \mathcal{R}^m, \Omega \in A_\Omega \subset \mathcal{R}^l \qquad \text{(1-2)}$$

In this representation, X refers to the system's state variables, namely the physical terms that evolve with time, Ω refers to the terms that remain constant and are known as parameters. Although this mathematical formalism is more complex than the formalism used in conventional artificial neurons it allows the exploration of all neural attributes [15].

1.4   CMOS based Neuromorphic Architectures

Spiking primitives have been built in CMOS analog circuits, digital neurosynaptic cores, and non-CMOS devices. A notable example of CMOS based neuromorphic architecture is the TrueNorth architecture developed by IBM as a part of DARPA's SYNAPSE program [20]. TrueNorth is a 5.4 billion transistor chip which is organized in 4096 neurosynaptic cores. The cores are interconnected via an intra-chip network which integrates 1 million programmable spiking neurons and 256 million configurable synapses. In terms of efficiency TrueNorth's power density is 20mW per cm^2 whereas a typical CPU processor has a power density of 50 to 100W per cm^2. True North's architecture is presented in Figure 1-9. Other notable examples are Neurogrid as part of Stanford University's Brains in Silicon program [21], HICANN as part of University of Heidelberg's FACETS/BrainScaleS project [22] and University of Manchester's neuromorphic chip as part of the SpiNNaker project [23]. The latter two are under the flagship of the European Commission's Human Brain Project [24]. These technologies apply the principles of neuronal computation, including robust analog signaling, physics-based dynamics, distributed complexity and learning. In relation to von Neumann architectures for tasks involving speech processing and machine vision these platforms

show advantages in efficiency, fault tolerance and adaptability. In spite of these advantages, there are some drawbacks when processing of faster signal is concerned (e.g., radio waveforms). The main problem is that these systems rely on slow timescale operations due to the dense interconnection needed for the integration of a neuromorphic architecture.

A neuromorphic processor requires a large number of interconnects (i.e., ~100 of many-to-one fan-in per processor). This fact creates a great communication burden. Bandwidth limitations are introduced due to the numerous point-to-point connections. Additional limitations appear due to radiative physics in electronic links. While some systems incorporate a dense mesh of wires overlaying the semiconductor substrate, large-scale systems demand some form of time-division multiplexing (TDM) or packet switching, notably, address-event representation (AER). These methods introduce computational overhead in spike representation because they are based in digital codes. This overhead sacrifices bandwidth, which can be orders of magnitude. As a result, CMOS based systems are suitable for applications in the kHz and MHz regime but they cannot be used for applications in the GHz regime (such as sensing and manipulating the radio spectrum and for hypersonic aircraft control).
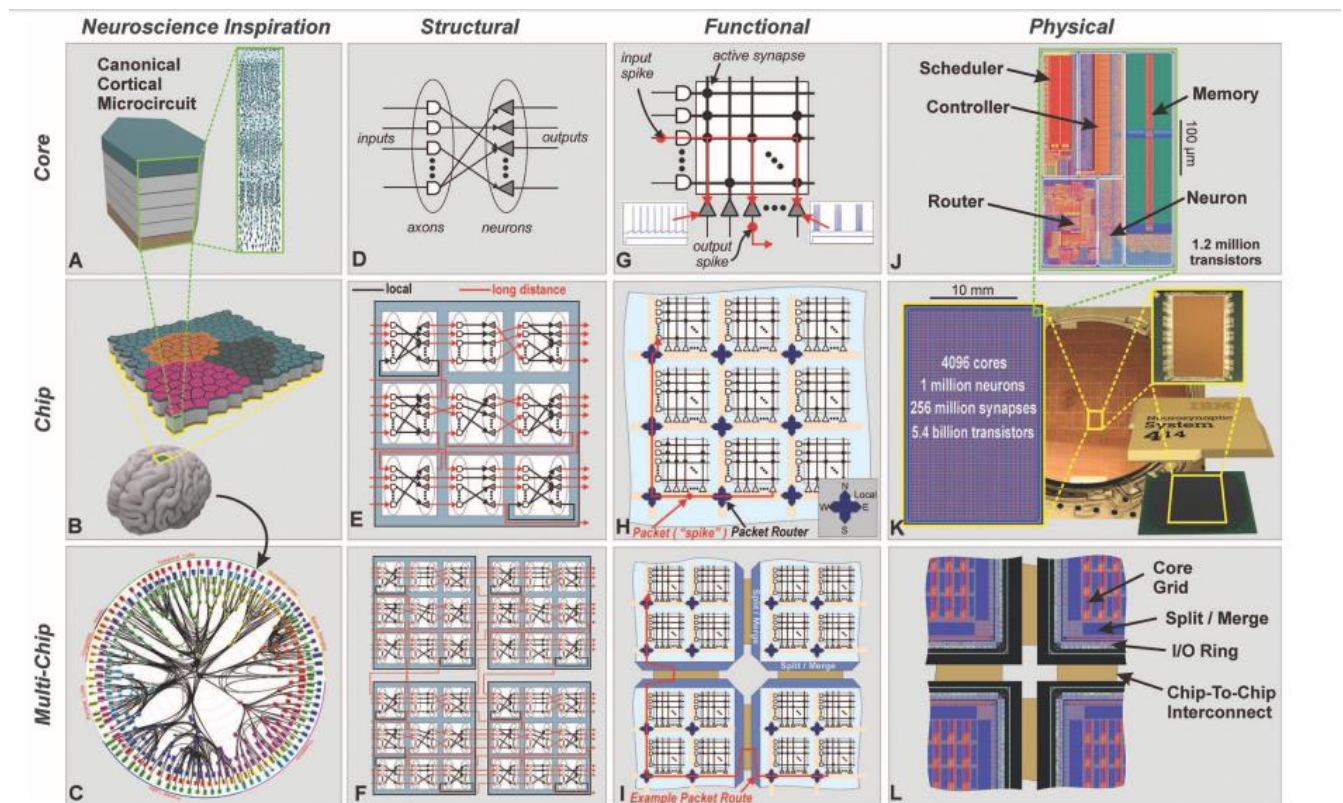
Figure 1-9 : IBM's TrueNorth architecture - a million spiking-neuron integrated circuit. Panels are organized into rows at three different views (neuroscience inspiration, structural, functional, and physical). (a) The neurosynaptic core is loosely inspired by the idea of a canonical cortical microcircuit. (b) A network of neurosynaptic cores is loosely inspired by the cortex's two-dimensional sheet. (c) The multichip network is inspired by the long-range connections between cortical regions shown from the macaque brain. (d) Structure of a neurosynaptic core with axons as inputs, neurons as outputs, and synapses as directed connections from axons to neurons. Multicore networks at (e) chip scale and (f) multichip scale both created by connecting a neuron on any core to an axon on any core with point-to-point connections. (g) Functional view of core as a crossbar where horizontal lines are axons, cross points are individually programmable synapses, vertical lines are neuron inputs, and triangles are neurons. Information flows from axons via active synapses to neurons. Neuron behaviors are individually programmable, with two

examples shown. (h) Functional chip architecture is a two-dimensional array of cores where long-range connections are implemented by sending spike events(packets) over a mesh routing network to activate a target axon. Axonal delay is implemented at the target. (i) Routing network extends across chip boundaries through peripheral merge and split blocks. (j) Physical layout of core in 28-nm CMOS fits in a $240\ \mu m$ -by- $390\ \mu m$ footprint. A memory (static random-access memory) stores all the data for each neuron, a time-multiplexed neuron circuit updates neuron membrane potential, a scheduler buffers incoming spike events to implement axonal delays, a router delays spike events, and an event-driven controller orchestrates the core's operation. (k) Chip layout of 64-by-64 core array, wafer, and chip package. (l) Chip periphery to support multichip networks. I/O. input/output [20].

1.5 Photonic Neuromorphic Platforms

The tremendous demand for interconnectivity in conventional computing systems gradually leads to the employment of photonic integrated circuits, allowing for faster and more efficient information transmission. With respect to information processing, although it is unlikely for optical platforms to achieve the efficiency of electronic systems when conventional architectures are considered (optical transistors), they are excellent candidates for unconventional types of computation like neuromorphic processing. Mapping a processing paradigm to its underlying dynamics, rather than abstracting the physics away entirely leads to significant improvements as far as efficiency and performance are concerned in relation to the CMOS based systems. The dynamics of photonic devices can show strong resemblances with the dynamics of the biological neurons. These systems can be described by an identical set of differential equations under appropriate conditions and approximations but exhibit vastly different parameter values. As a result, photonic platforms can produce spikes of 10 ps time magnitude and 1 ns period paving the way for neuro-inspired solutions for applications in the GHz regime (Figure 1-10). This formal mathematical analogy between different systems (biological and photonic systems) is called isomorphism. Large scale integrated photonic platforms offer the opportunity for ultrafast neuromorphic processing that complements neuromorphic microelectronics aimed at biological timescales.
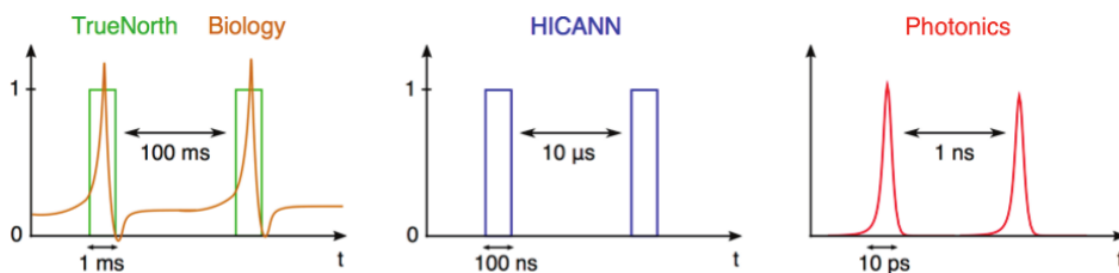
Figure 1-10 : Differences in time scales between biological neurons (left), current electronic neurons (middle) and photonic neurons (right) [12].

Photonic neuromorphic platforms are not developed so as to substitute electronic platforms entirely, but in order to address problems that are not reachable by electronics due to their inherent disadvantages in terms of interconnectivity. Some important areas where photonic neuromorphic processors will play an important role are:

- Enabling new breakthroughs in the field of fundamental physics: qubit readout classification [25], high-energy particle collision classification [26], [27], fusion reactor plasma control [28].

- Non - linear programming : solving nonlinear optimization problems (robotics, autonomous vehicles, predictive control) [29], and partial differential equations [30].

- Machine Learning accelerators, so as to boost the efficiency of machine learning schemes implemented by electronics: vector-matrix multiplications [31], deep learning inference [32], ultrafast or online learning [33].

- Intelligent signal processing : direct processing of the RF spectrum [34], fiber - optic communication [35].

With respect to photonic platforms and SNNs, the best demonstration to date is a platform consisting of micro-ring resonators (MRRs) acting as integrate and fire neurons by utilizing phase change materials (PCM) (Figure 1-11) [36]. A PCM is a material which at its crystallized form absorbs incoming optical power up to a threshold, where the material enters its amorphous state. At its amorphous state, the PCM permits light propagation. This threshold property is used in this work so as to emulate the neural threshold. PCM is also be placed upon the waveguides in order to emulate synapses, by using the non-abrupt contrast between the amorphous and the crystallized states. An important advantage of this platforms is its usage of WDM. Each input is encoded on a different wavelength and a sequence of MRRs is used to multiplex the various signals into a single waveguide. Signals can then be demultiplexed by a similar MRR sequence. This property is important since the connectivity between different neural nodes can be achieved in the optical domain by means of a single waveguide which eliminates the connectivity problems existing in electronic implementations. The all-optical SNN solved successfully simple machine learning tasks by using both supervised and unsupervised learning techniques.

Apart from the WDM, another important property of the photonic systems is the energy efficient implementation of synaptic connections by using typical waveguide meshes [31]. The mesh in Figure 1-12 consists of multiple re-configurable Mach Zehnder interferometer (MZI) modulators. A MZI is a two-port system that can be configured so as to modify the energy distribution between two input modes, thus effectively modifying their amplitude. It can be mathematically proved that a waveguide mesh that consists of multiple MZIs is able to implement a weight matrix transformation [31]. This photonic based topology has an efficiency in the order of $(m \times N)^{-1}$ fJ per operation, where m is the number of neural layers and N is the number of inputs, whereas a conventional GPU implementation consumes 100 pJ per operation. This dramatic decrease in terms of energy consumption stems from the fact that computation in the photonic domain with this topology consists of a simple passing of light through the passive pre-configured MZIs. Power is needed only for maintaining the MZI configuration in the experiment. However, in the future the employment of non-volatile materials to control the propagation of the light modes will reduce even this power consumption to zero [37].

1.6 Photonic Spiking Neuromorphic Nodes

Apart from the MRR based experiment [36] there is not for the time being another full scale implementation of a SNN. However, there are numerous photonic candidates for single neuromorphic nodes which can be used in future platforms. There are multiple such topologies based on a wide range of different methods and materials such as two-section semiconductor lasers, optically injected laser, photonic crystals, semiconductor micro-disk lasers, lasers with optical feedback, etc [12]. All these approaches are

isomorphic to biological neurons acting in nanosecond time scales. Some of these topologies are analyzed in terms of their neuro-computational properties in Chapter 3. Future SNN platforms will consist of numerous such elements which renders issues like scalability, fan out and fan in capabilities as well as thermal and noise resilience very important aspects.
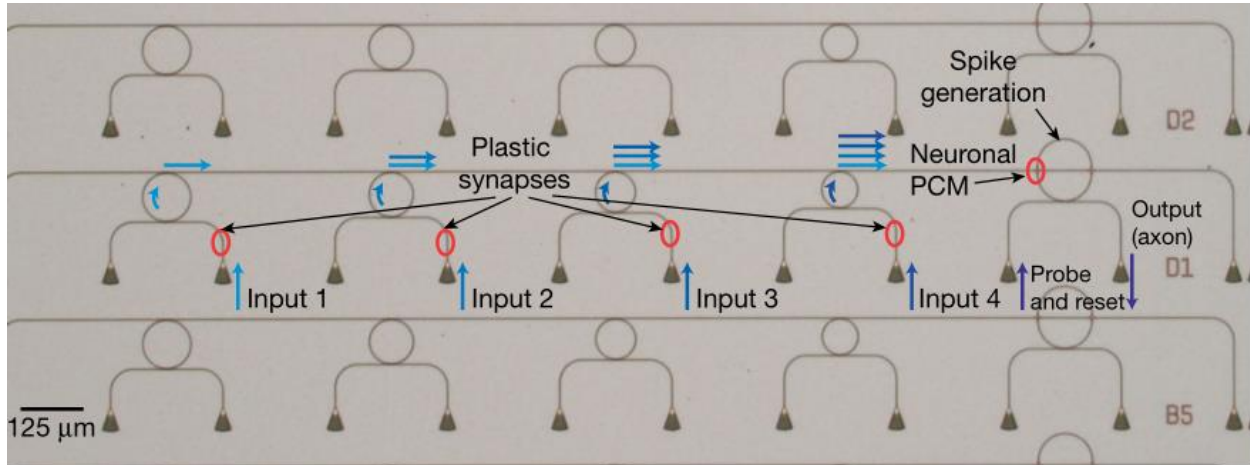
Figure 1-11 : The experimental implementation of an all optical SNN based on MRRs and PCMs [36].

A particularly important laser type that is the main focus of this work is the quantum dot laser (QD). QD lasers hold some very desirable properties compared to other platforms such as very low current threshold [38], robustness to thermal variations [39], [40] and high compatibility with silicon platforms [41]. Moreover, due to their atomic-like nature they can easily emit from multiple wavebands. The interaction between multiple wavebands can pave the way to new possibilities in the area of neuromorphic computing processing such as all - optical excitatory and inhibitory neurons [42], as well as improvements in the temporal resolution and processing speed [43].

1.7   Organization of this work

This work targets the theoretical analysis of QD lasers as potential neuromorphic nodes. In Chapter 2, the theory of non-linear systems is presented and through this framework, the property of excitability is mathematically examined. Since a pure mathematical formalism is introduced in this chapter, the conclusions that will be drawn are compatible with numerous systems such as biological systems, electronic systems, chemical systems and photonic systems. Thus, we can point to the similarities between biological and photonic neuromorphic nodes. From this point of view, the neuro-computational properties of key laser topologies will be discussed. In Chapter 3 an introduction to laser physics is provided. At the end of this chapter particular emphasis is given in the case of QD lasers. In Chapter 4, the neuro-computational properties of the QD laser are analyzed. In this case the QD laser is under an optical injection scheme. The interplay between multiple wavebands as well as their role in neural dynamics is examined for the first time from the viewpoint of non-linear theory. In Chapter 5 conclusions is provided along with some ideas for further researching the QD laser platforms as cognitive processors.

Figure 1-12 : (a) The 2-layered topology used in the experiment. This system is used 4 times so as to implement the desired neural network. An instance is a weight matrix implemented with MZIs, whereas the non-linear activation function is achieved by simulating a saturable absorber on a conventional computer. (b) The experimental feedback and control loop used in the experiment. (c) A MZI which is configured by modifying the phase delay. It can be seen that its re-configuration, which is achieved by changing the applied voltage, results in a change of the light transmission. (d) The photonic chip used in the experiment. The colors illustrate the propagation path of the 4 inputs (red) towards the 4 outputs (light blue) [31].

2. THE GEOMETRY OF EXCITABILITY

Arguably, the most significant characteristic of neurons is excitability. Excitability permits the generation of spike events which encode information in neural systems. It is however important to notice that excitability is not a biological notion, but a mathematical one. This means, that excitability is found not only in biological neurons but also in chemical reactions [44], electronic systems [45] and photonic systems [46] to name a few. This analogy between biological neurons and other systems allows for building neuromorphic systems similar to those described in Chapter 1. Thus, it is important to examine the notion of excitability from a geometrical point of view by means of non-linear systems theory so as to design new and highly efficient neuromorphic nodes.

2.1 Non – linear Systems

A non-linear system is a system that is described by a set of non-linear differential equations similar to (1-2), namely:

$$\frac{dX}{dt} = F(X; \Omega), \ \ X \in A_x \subset \mathcal{R}^m, \Omega \in A_\Omega \subset \mathcal{R}^l \quad \text{(2-1)}$$

In these equations, $X \in R^m$ is the state – space vector which describes the behavior of the system, whereas $\Omega \in \mathcal{R}^l$ are the parameters. The solution of this set can be calculated by using an initial condition vector $X(0) \in \mathcal{R}^m$ and it is known as flow. The flow can be visualized as the trajectory that is followed by the state – space vector in the $\mathcal{R}^m$ Euclidean space. An example can be seen in Figure 2-1. The arrows correspond to the vector field and provide an illustration of the trajectory that is to be followed when starting from different initial conditions.
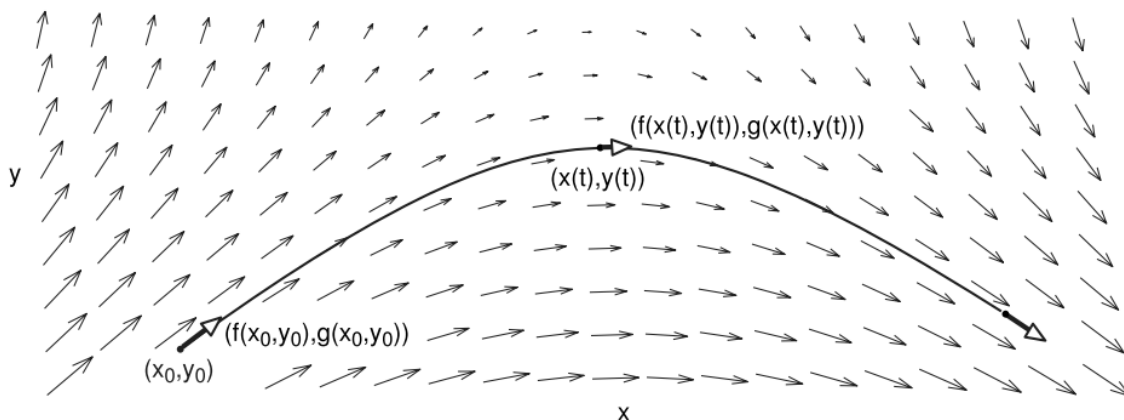
Figure 2-1 : The flow of a two-dimensional system starting from the initial condition $X = (x_0, y_0)$ [15].

2.1.1 Equilibrium Points and Stability

Equilibrium points are defined simply be setting the left-hand side of (2-1) equal to 0:

$$F(X_e; \Omega) = 0 \qquad\qquad (2\text{-}2)$$

A system may have none, one or multiple equilibrium points. When the initial condition $X(0)$ is equal to the equilibrium X_e, then the flow of the system remain un-changed and the system is known to be in equilibrium.

The equilibrium points can be either stable or unstable. In the first case, an initial condition $X(0)$ in the proximity of the equilibrium point will result in a flow towards the equilibrium point, whereas in the second case the flow will move away from the equilibrium. Since analytical solutions to (2-1) are very difficult, different tools are used so as to describe the notion of stability. The most important tools are arguably the second and first Lyapunov methods. The second Lyapunov method provides a strict definition of stability and allows for determining the system's properties without solving the system. The first Lyapunov method is a less strong tool for defining the stability of a system but it is easier to be used for simple problems and it is based on the linearization of the non-linear system.

2.1.1.1 The Second Lyapunov Method

Before describing the notion of stability by means of the second Lyapunov method it is important to provide some definitions.

Definition 1: A function $v(x, t)$ is said to be positive definitive inside a certain neighborhood $\mathcal{N} - \{0\}$ around 0, when $v(x, t) > 0$. It is known to be positive semi-definite when $v(x, t) \geq 0$.

Definition 2: A function $v(x, t)$ is said to be negative inside a certain neighborhood $\mathcal{N} - \{0\}$ around 0, when $v(x, t) < 0$. It is known to be negative semi-definite when $v(x, t) \leq 0$.

The distance between two points x, y in $\mathcal{R}^m$ is a function $d(x, y): \mathcal{R}^m \to \mathcal{R}$ of the form:

$$d(x, y) = \begin{cases} d(x, y) > 0, & x \neq y \\ 0, & x = y \end{cases}$$

A characteristic example of such a function is the Euclidean distance defined as $d(x, y) = \sqrt{\sum_{i=1}^{m}(x_i - y_i)^2}$. From this relation it is concluded that the distance between x and 0 is a positive function, namely $v(x(t)) = d(x(t), 0)$.The 0 point in this case is regarded as an equilibrium point of the system without loss of generality. In particular, any equilibrium point X_e can be substituted with the 0 point after the following change of variables $Z = X - X_e$.

With these definitions, the stability of the equilibrium point can be deduced. The derivative of a function $v(x(t), t)$ is given by the relation:

$$\dot{v}(x, t) = \frac{\partial v}{\partial t} + F(X; \Omega)\frac{\partial v}{\partial X} \qquad\qquad (2\text{-}3)$$

As a result, if there is a positive definite function $v(x, t)$ such that $\dot{v}(x, t)$ is a negative definite function, then the equilibrium 0 is asymptotically stable, which means that the flow of the system in the neighborhood of 0 converges with time at this point. If $\dot{v}(x, t)$ is a semi-negative definite function, then the equilibrium 0 is uniformly stable which means that the flow remains in the region of 0. In these cases, the function $v(x, t)$ is

known as a Lyapunov function. On the other hand, if $\dot{v}(x,t)$ is a positive definite then the equilibrium point is unstable, meaning that the flow moves away from the equilibrium.

The power of the aforementioned method stems from the fact, that the inequalities $\dot{v}(x,t) < 0$ and $\dot{v}(x,t) \leq 0$ can provide certain region boundaries $Bx \in \mathcal{R}^m$, known as regions of attraction, thus giving information with respect to the neighborhood where stability holds. If the above equations hold for the whole $\mathcal{R}^m$, then the equilibrium is said to be globally asymptotically stable and globally stable, respectively. However, it should be stressed that many times it is difficult to find a Lyapunov function and for this reason the first Lyapunov method is valuable, although weaker as a system's analysis tool.

2.1.1.2 The First Lyapunov Method

By using the Taylor's method so as to expand the relation (2-1), around its equilibrium point 0, the following linear system is acquired.

$$\dot{X} = AX + g(X,t), X \in \mathcal{R}^m, A \in \mathcal{R}^{m \times m} \qquad (2\text{-}4)$$

It is important in this case that $\| g(X,t) \| \to 0$ as $X \to X_e = 0$. By analyzing the simpler linear system, the stability of the equilibrium can be studied but as opposed to the second Lyapunov method no conclusions can be made with respect to the region of stability. For the purposes of this work however, this method is adequate.

The stability of the equilibrium is determined by the eigenvalues of the matrix A. The m eigenvalues can be determined by solving the characteristic equation:

$$|\lambda I - A| = 0 \qquad (2\text{-}5)$$

In this relation, $I \in \mathcal{R}^{m \times m}$ is the identity matrix. The determinant leads to a polynomial equation of m order with λ as the unknown value. The values of the solutions, known also as eigenvalues, $\lambda_i, i = 1, \dots, m$ determine the stability of the equilibrium.

Without loss of generality, we assume a two-dimensional system, namely m = 2. The linear system is described by the relation:

$$\dot{X} = AX$$

Here A is a 2 x 2 real matrix. The solution of this linear system for a given initial state X_0 is given by:

$$X(t) = M exp(J_r t) M^{-1} X_0$$

In this relation, J_r is the real Jordan form of A and M is a real nonsingular matrix such that $M^{-1}AM = J_r$. Depending on the two eigenvalues of A, the real Jordan form may take one of three forms:

$$\begin{bmatrix} \lambda_1 & 0 \\ 0 & \lambda_2 \end{bmatrix}, \begin{bmatrix} \lambda & k \\ 0 & \lambda \end{bmatrix}, and \begin{bmatrix} \alpha & -\beta \\ \beta & \alpha \end{bmatrix}$$

The term k is either 0 or 1. The first form corresponds to the case where both eigenvalues are real and distinct, the second form is when both eigenvalues are real and equal and the third form refers to the case where both eigenvalues are complex $\lambda_{1,2} = \alpha \pm j\beta$. There are four possible cases with respect to stability and the eigenvalues [47].

Case 1: Both eigenvalues are real $\lambda_1 \neq \lambda_2 \neq 0$.

In this case, $M = [v_1, v_2]$ where v_1 and v_2 are the real eigenvectors corresponding to the eigenvalues λ_1, λ_2. By taking the change of coordinates $z = M^{-1}X$, the equation is transformed in:

$$\dot{z} = \begin{bmatrix} \lambda_1 & 0 \\ 0 & \lambda_2 \end{bmatrix} z$$

Given that $z_0 = (z_{10}, z_{20})$ the two solutions are

$$z_1(t) = z_{10}e^{\lambda_1 t}, \quad z_2(t) = z_{20}e^{\lambda_2 t}$$

It can be seen that if $\lambda_1, \lambda_2 < 0$, then both solutions converge exponentially to the equilibrium $z_e = 0$. In this case, the equilibrium is known as a *stable node*. If, however, both eigenvalues are larger than 0 then the flow moves away from the equilibrium. In this case, the equilibrium is known as an *unstable node*.
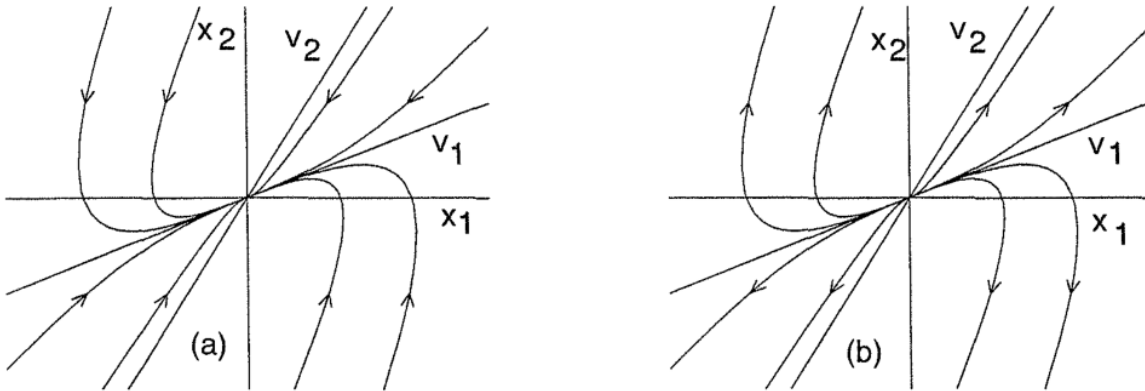
Figure 2-2 : State space diagrams for (a) a stable node, (b) an unstable node [47].

If the eigenvalues have opposite signs, namely $\lambda_2 < 0 < \lambda_1$, then the eigenvectors v_1, v_2 define the direction where the trajectory moves away from the equilibrium and toward the equilibrium respectively. In this case, the equilibrium is a saddle node and the system is again unstable.

In general, for an m-dimensional system when all eigenvalues are negative then the equilibrium is a stable node, whereas when all the eigenvalues are positive the equilibrium is an unstable node and finally when there are eigenvalues of opposite signs then the equilibrium is a saddle node.

Case 2: Complex eigenvalues $\lambda_{1,2} = \alpha \pm jb$.

The change of coordinates $z = M^{-1}X$, gives the form:

$$\dot{z} = \begin{bmatrix} \alpha & -\beta \\ \beta & \alpha \end{bmatrix} z$$

The change in polar coordinates $r = \sqrt{z_1^2 + z_2^2}$, $\theta = \tan^{-1}(z_1/z_2)$ leads to the equations:

$$\dot{r} = \alpha r, \qquad \dot{\theta} = \beta$$

Given the initial state (r_0, θ_0), the solutions are:

$$r(t) = r_0 \exp(\alpha t), \qquad \theta(t) = \theta_0 + \beta t$$
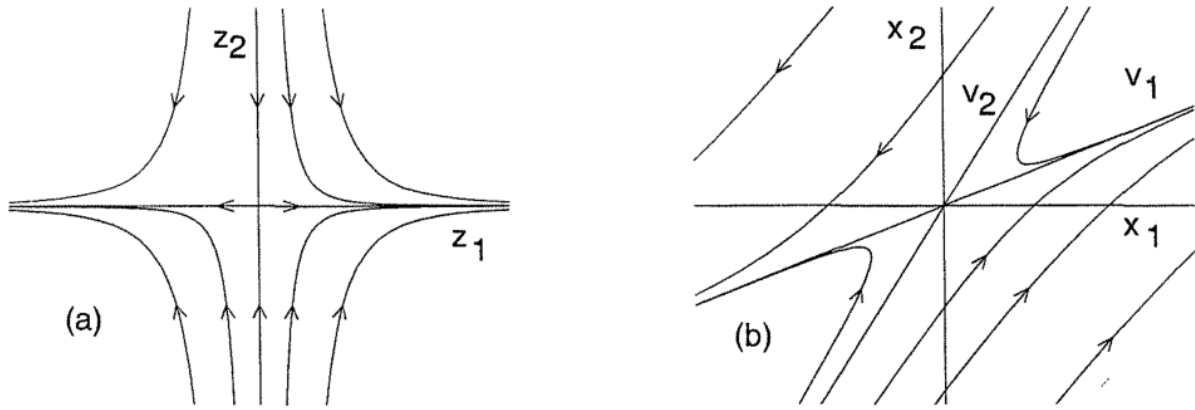
Figure 2-3: A saddle node equilibrium in (a) z- coordinates, (b) X – coordinates [47].

It can be seen that when $a < 0$ the radius r decreases and the solution converges towards the equilibrium. However, the trajectory follows a spiral due to θ which evolves with angular frequency β. The equilibrium in this case is a *stable focus*. When $a > 0$, the radius r increases and the solution moves away from the equilibrium. In this case the equilibrium is called an *unstable focus*. At last, when $a = 0$, the radius remains constant and equal to r_0 and the trajectory moves in a circle around the equilibrium. The radius in this case depends on the initial condition. The equilibrium is called a *center*. These results hold also in the case of m-th order systems.
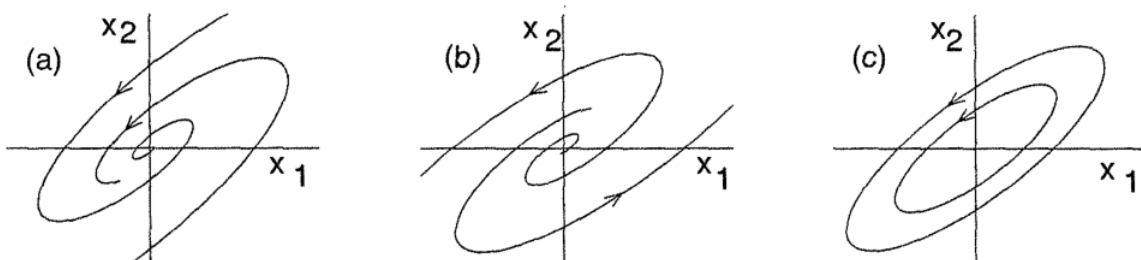
Figure 2-4: State space diagrams for (a) a stable focus, (b) an unstable focus, (c) a center [47].

Case 3: Nonzero multiple real eigenvalues $\lambda_1 = \lambda_2 = \lambda \neq 0$.

The change in z coordinates transforms the system in:

$$\dot{z} = \begin{bmatrix} \lambda & k \\ 0 & \lambda \end{bmatrix} z$$

The solution is given by:

$$z_1(t) = \exp(\lambda t)\,(z_{10} + kz_{20}t), \quad z_2(t) = \exp(\lambda t)\,z_{20}$$

When k = 0 the trajectories follow a different route than in the case of k=1. When $\lambda < 0$ the system is stable and the equilibrium is a stable node, otherwise the system is unstable and the equilibrium in an unstable node.

Case 4: One or more eigenvalues are equal to 0.

When one or both eigenvalues are 0, then the system around this equilibrium is in a sense degenerate. By changing in z coordinates when $\lambda_1 = 0$, $\lambda_2 \neq 0$ the system transforms to:

$$\dot{z}_1 = 0, \quad \dot{z}_2 = \lambda_2 z_2$$

The solution is:

$$z_1(t) = z_{10}, \quad z_2(t) = z_{20}\exp\left(\lambda_2 t\right)$$

The solution z_2 converges to the equilibrium subspace in the direction dictated by the v_2 eigenvector, when $\lambda_2 < 0$ and moves away when $\lambda_2 > 0$. The point where the solution moves towards or away from it, depends on the initial condition of z_{10}.

When both eigenvalues are 0 then the system becomes:

$$\dot{z}_1 = z_2, \quad \dot{z}_2 = 0$$

The solution is:

(a)   (b)
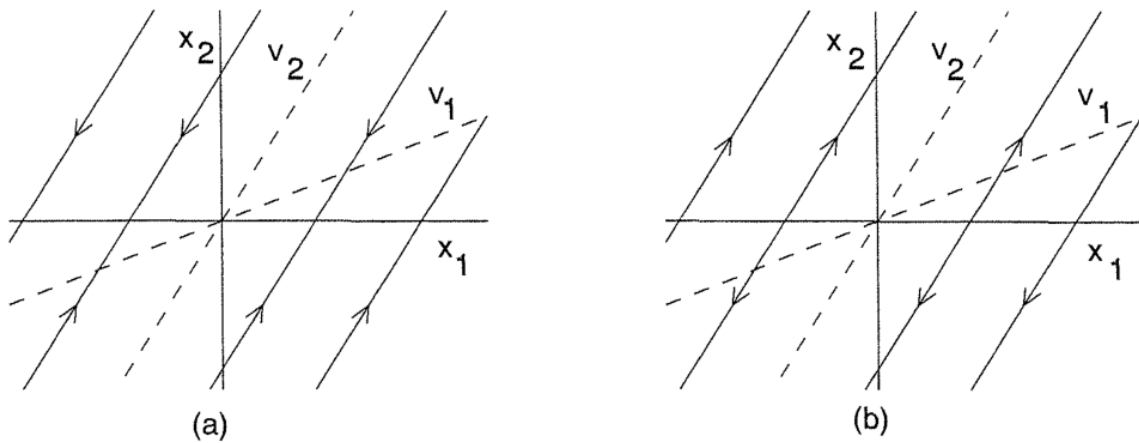
Figure 2-5: The state space diagram for (a) $\lambda_1 < 0$ and (b) $\lambda_2 > 0$ [47].

$$z_1(t) = z_{10} + z_{20}t, \quad z_2(t) = z_{20}$$

The term $z_{20}t$ will increase or decrease depending on the sign of the initial condition z_{20}. Trajectories starting off the equilibrium sub-space will move parallel to it.
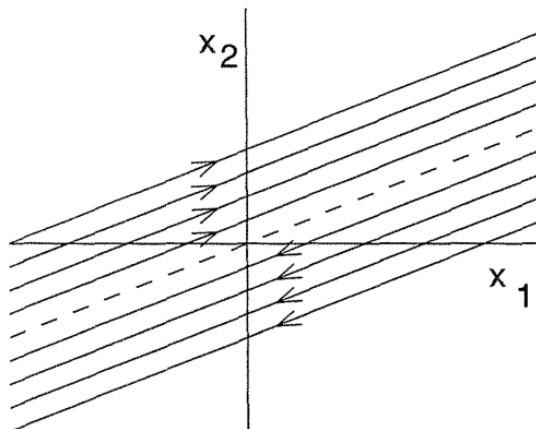
Figure 2-6: The state space diagram for $\lambda_1 = \lambda_2 = 0$ [47].

2.1.2 Limit Cycles

In the case of a non-linear system a limit cycle is defined as an isolated closed trajectory. This means that initial conditions close to the limit cycle will spiral either towards or away from the limit cycle. In the first case, the limit cycle is stable whereas in the second case it is unstable. In some exceptional cases the limit cycle can be stable or unstable depending on whether the initial conditions are inside or outside the limit cycle and then the limit cycle is half-stable.
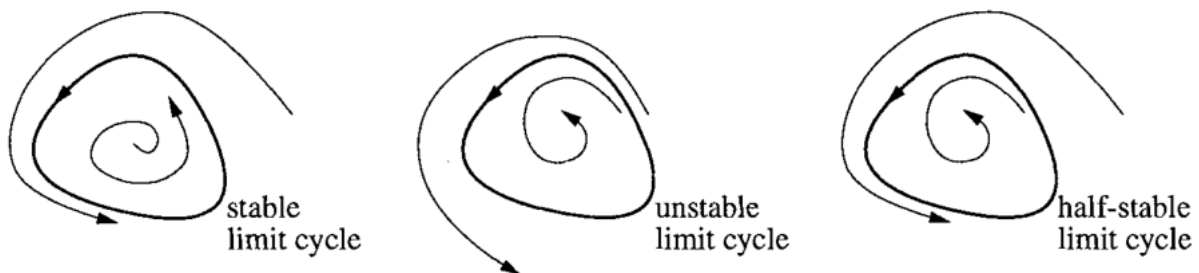
Figure 2-7: (Left) stable limit cycle, (Middle) unstable limit cycle, (Right) half-stable limit cycle [48].

It is important to notice, that although the limit cycle is a periodic trajectory as in the case of the center equilibrium, it differs from it since the trajectory is isolated and does not depend on the initial conditions. Limit cycles in nature are observed in systems exhibiting self-sustained oscillations like the spiking of a neuron, daily rhythms in human body temperature and even dangerous self-excited vibrations in bridges [48].

2.2 Bifurcations

We now turn our attention on the parameters of the system $\Omega \in \mathcal{R}^l$. Up to this point they were regarded constant. However, their values play a crucial role on the behavior of the system. Without loss of generality consider the two-dimensional non-linear system:

$$\dot{x}_1 = \mu - x_1^2$$
$$\dot{x}_2 = -x_2$$

In this system $X \in \mathcal{R}^2$ and $\Omega \in \mathcal{R}$, where μ is the parameter on which it depends. By solving the system so as to detect its equilibrium points using (2-2), two roots are found at $(\sqrt{\mu}, 0)$ and $(-\sqrt{\mu}, 0)$. By applying the first Lyapunov method so as to analyze the stability properties of the two equilibrium points it can be seen that $(-\sqrt{\mu}, 0)$ is as saddle node and $(\sqrt{\mu}, 0)$ is a stable node, when $\mu > 0$. As μ decreases, the saddle and the node approach each other at the state space, collide at $\mu = 0$ and disappear at $\mu < 0$ since in that case there is no solution to the characteristic equations determined by the first Lyapunov method. This process can be seen in Figure 2-8. Since a qualitative change appears at $\mu = 0$, marking the transition from two equilibrium points to none, this change is called a bifurcation. The parameter that is linked to this bifurcation is known as a bifurcation parameter and the point $\mu = 0$ is known as the bifurcation point. *In general, a bifurcation is a change in the equilibrium points or periodic orbits, or stability properties, as one or more parameters are varied* [47].

Since the bifurcation in Figure 2-8 involves a saddle node and a stable node, it is known as a saddle – node bifurcation. Since this bifurcation is caused by changing a single parameter, it is known as a co-dimension 1 bifurcation. In general, there are also bifurcations that are caused by changing simultaneously two parameters, which are called co-dimension 2 bifurcations but they only rarely are observed in experiments. For

this reason, only co-dimension 1 bifurcations will be introduced, which are the most important for most systems in general and neuromorphic systems in particular.
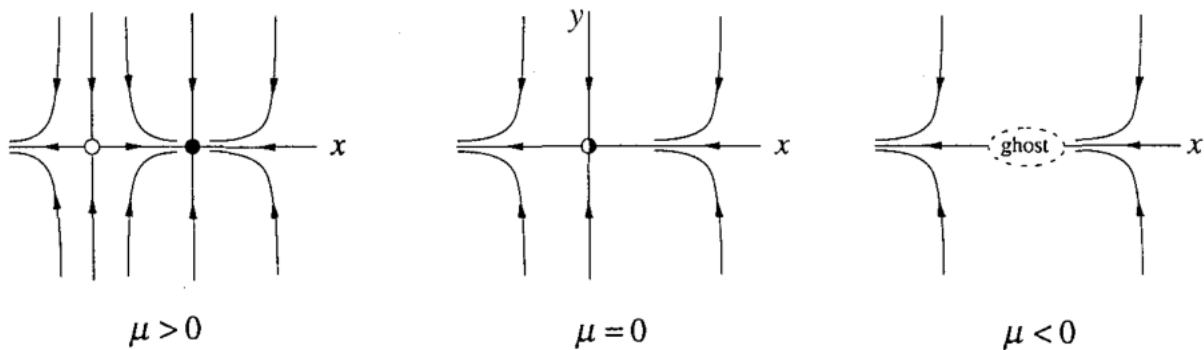
Figure 2-8: The saddle-node bifurcation for $\mu > 0$ (left), $\mu = 0$ (center) and $\mu < 0$ (right) [48].

In terms of the saddle-node bifurcation it can be seen that even when $\mu < 0$ there is a significant influence around the area where the saddle node and stable node collided known as a ghost [48]. A ghost is a region where the flow in delayed significantly. This delay introduces a bottleneck effect which in general increases as $(\mu - \mu_c)^{-\frac{1}{2}}$, where μ_c is the bifurcation point (in the example above $\mu_c = 0$).

Pitchfork Bifurcation

The pitchfork bifurcation is illustrated in Figure 2-9. Before the bifurcation occurs, only a single stable node equilibrium exists for the system, whereas beyond the bifurcation point this equilibrium becomes unstable (a saddle node) and two stable points appear. This bifurcation is important in the case of lasers as it is linked to the appearance of stimulated emission when the pumping is higher than the threshold value. In this case the pumping is the bifurcation parameter and the threshold the pitchfork bifurcation point (See Chapter 3).

Andronov - Hopf Bifurcation

With respect to Andronov-Hopf bifurcation there are two possible cases; (a) the subcritical Hopf bifurcation and (b) the supercritical Hopf bifurcation. The subcritical Hopf bifurcation is shown in Figure 2-10. Before the bifurcation point, the system has one stable focus, one stable limit cycle and one unstable limit cycle between them. In this case, the system is bistable, meaning that by introducing a suitable perturbation one can move the initial conditions at the outer side of the unstable circle, thus noticing self-pulsations or at the inner part of the circle thus observing a constant response. As the bifurcation parameter is varied, the stable focus and the unstable limit cycle approach each other and at the bifurcation point the unstable limit cycle disappears and the stable focus becomes an unstable focus, meaning that its complex eigenvalues acquire a positive real part.

In the supercritical Hopf bifurcation only a single stable focus exists before the bifurcation point. Beyond that point, the stable focus becomes unstable and a stable limit cycle appear. In terms of the system's response, this is connected to a transition from a constant response to self-pulsations. It must be noted, that close to the bifurcation point the period of the stable limit cycle is dictated by the imaginary part of the corresponding complex eigenvalues of the equilibrium point. Also, in this case no bistability is observed as opposed to the subcritical Hopf case.
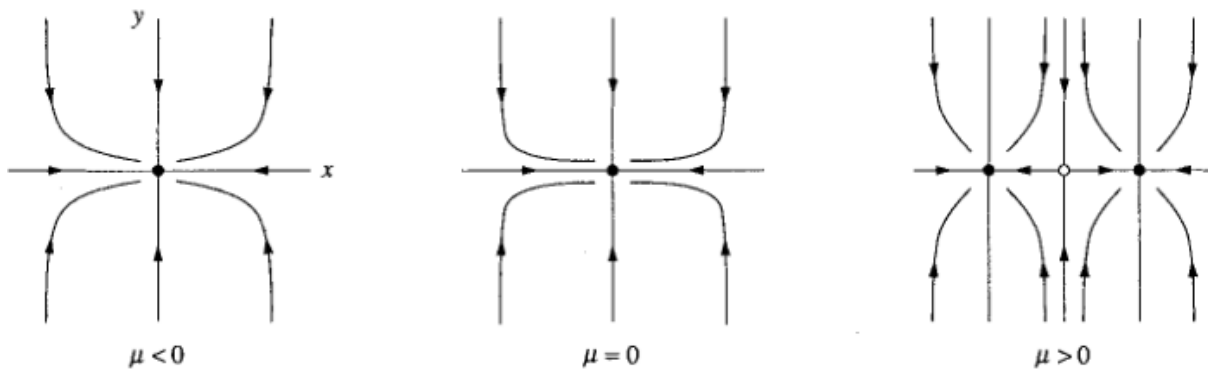
Figure 2-9: The pitchfork bifurcation. For negative values of the bifurcation parameter μ only a stable point appears. At $\mu > 0$, the stable point becomes unstable and two new and symmetrical stable points appear [48].
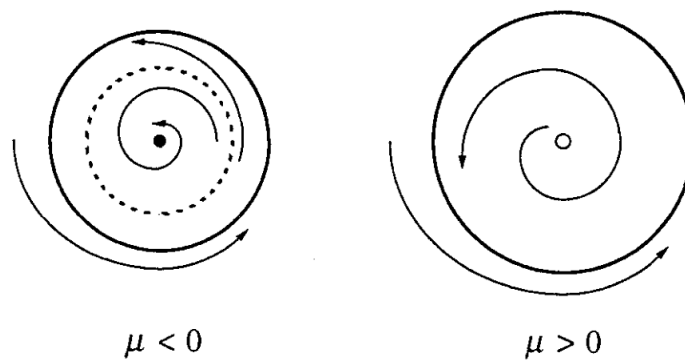
Figure 2-10 : The subcritical Hopf bifurcation. For negative μ, a stable limit cycle and a stable focus co-exist and they get separated by an unstable limit cycle. For positive μ, the unstable limit cycle disappears and the stable focus becomes unstable thus leaving the limit cycle as the only stable trajectory [48].

Saddle – Node on Limit Cycle bifurcation

The Saddle-Node on Limit Cycle bifurcation (SNLC) appears in Figure 2-12. Before the bifurcation point, there is an unstable focus and a stable limit cycle. As the bifurcation parameter approaches the bifurcation point, the flow starts to experience a significant delay on a certain region of the limit cycle, which is linked to a ghost. Beyond the bifurcation point, a stable node and a saddle node appear on this region via a saddle node bifurcation. Since this bifurcation takes place on a limit cycle it is known as a SNLC bifurcation. In Figure 2-12, when $\mu < 1$ some special trajectories are illustrated upon the limit cycle and upon the straight lines. These trajectories are known as manifolds and they can be stable or unstable with respect on an equilibrium point, when they move towards or away from the equilibrium point the flow, respectively. For example, initial conditions upon the stable manifold of the saddle node will lead the flow towards it. These manifolds are connected to the stable and unstable eigenvalues presented during the first Lyapunov method. However, in the first Lyapunov method only a linear approximation of the manifolds can be made by means of the eigenvectors that are linked to the corresponding eigenvalues.

$$\mu < 0 \qquad\qquad \mu > 0$$
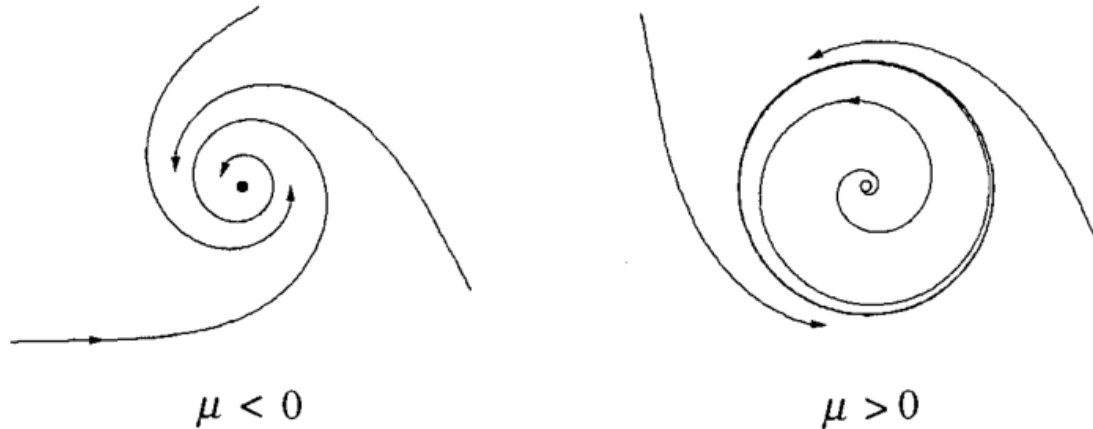
Figure 2-11: The supercritical Hopf bifurcation. For $\mu < 0$ only a stable focus exists. For $\mu > 0$ the stable focus becomes unstable and a stable limit cycle appears thus marking the onset of self-pulsations [48].

$$\mu > 1 \qquad\qquad \mu < 1$$
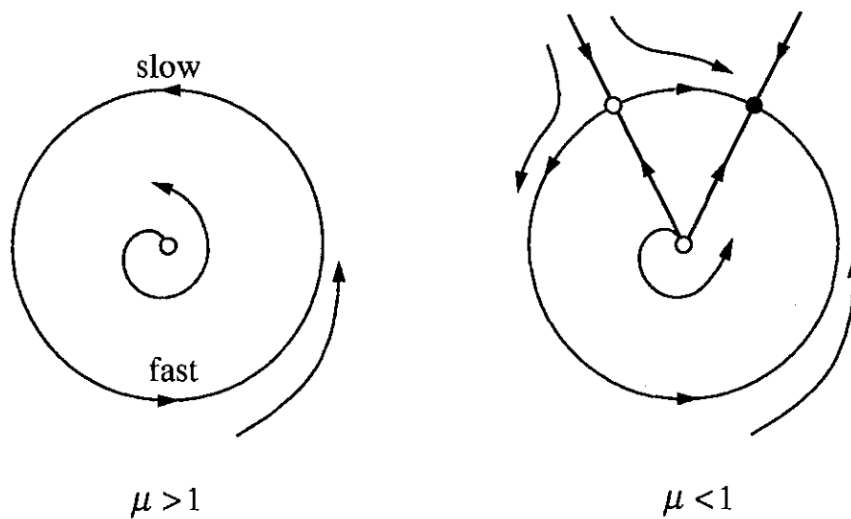
Figure 2-12 : The saddle node on limit cycle (SNLC) bifurcation. When $\mu > 1$ an unstable focus is surrounded by a stable limit cycle. The flow on the limit cycle is characterized by a small region on top where the orbit propagates in a slow manner. As μ decreases, this bottleneck region becomes even slower and at $\mu = 1$ a saddle node and a stable node appear. For $\mu > 1$ the coexist on the limit cycle [48].

Homoclinic Bifurcation

The last important bifurcation mechanism for our purposes is the homoclinic bifurcation illustrated in Figure 2-13. The transition from (a) to (d), shows that at point (a) there are an unstable point, saddle point and a stable limit cycle. At (b) a stable and an unstable manifold of the saddle point approach the stable limit cycle and at point (c) they collide forming a closed loop. At (d) as the bifurcation parameter further changes, manifolds of the saddle point are separated again and the limit cycle disappears. The point (c) corresponds to the bifurcation point which marks the disappearance of the stable limit cycle. This bifurcation is known as the saddle-homoclinic bifurcation or simply the homoclinic bifurcation.
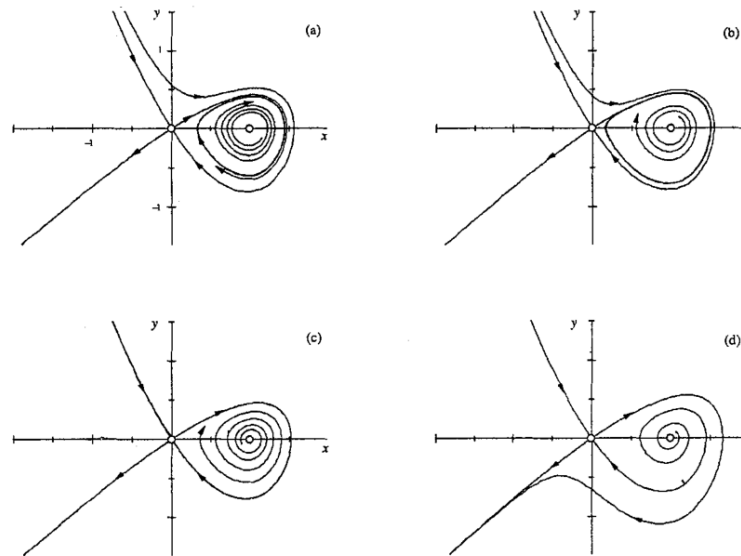
Figure 2-13: The Homoclinic bifurcation [48] .

2.3 Neuronal Excitability

Excitability in neural systems can be studied geometrically by examining the neuron as a non-linear system. From this point of view a dynamical system with a stable equilibrium point is excitable if there is a large – amplitude trajectory that starts in a small neighborhood of the equilibrium, leaves the neighborhood and then returns back [15]. This stable equilibrium corresponds to the resting state of the neuron and the large amplitude trajectory to a spike event. The movement of the flow from the stable equilibrium to the neighborhood where the large amplitude trajectory takes place is enforced externally and it is known as triggering.
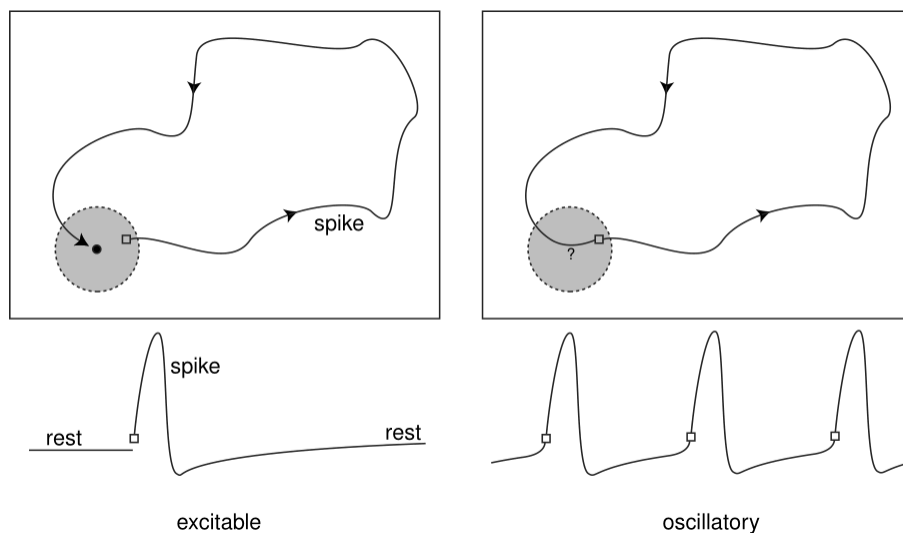
Figure 2-14: The geometric interpretation of excitability. In the left, the system has a stable equilibrium. Perturbations that move the orbit outside a specific region induce a spike even (long trajectory). In the right, a bifurcation has taken place and the only attractor is a LC. As the orbit follows the LC, the output performs oscillatory dynamics [15].

From the point of view of bifurcations, a system is excitable when it is biased by appropriately configuring a single parameter so as for the system to be close to a bifurcation that involves a limit cycle. For example, in Figure 2-14 it is shown that a

small change of a bifurcation parameter substitutes the stable equilibrium with a stable limit cycle.

A summary of the 4 major bifurcations connected with basic spiking activity (excluding bursting and other more complex neural behaviors) are shown in Figure 2-15.

Bifurcation of an equilibrium	Fast subthreshold oscillations	Amplitude of spikes	Frequency of spikes
saddle-node	no	nonzero	nonzero
saddle-node on invariant circle	no	nonzero	$A\sqrt{I-I_{\mathrm{b}}} \to 0$
supercritical Andronov-Hopf	yes	$A\sqrt{I-I_{\mathrm{b}}} \to 0$	nonzero
subcritical Andronov-Hopf	yes	nonzero	nonzero

Figure 2-15 : The transition from stable to oscillatory dynamics and the evolution of the latter under the variation of the bifurcation parameter I, whose bifurcation point is I_b [15].

2.3.1 The difference between triggering and the bifurcation parameter.

Before studying the spiking dynamics in the context of bifurcation theory it is important to make a distinction between triggering and the bifurcation parameter. When the input has a pulsed-like form (e.g., spikes from pre-synaptic neurons), then the excitation process is referred to as triggering. The triggering can be directly applied on a state-space variable thus changing the initial conditions of the flow, whereas it can be applied also on the bifurcation parameter. In the second case, the position of the equilibriums will change thus forcing the orbit out of equilibrium. As soon as the equilibrium returns to its previous position after the trigger - a single pulse - the flow will have acquired a new initial condition and the outcome will be similar to one achieved by directly modifying the orbit of the system.

2.3.2 Hodgkin's Classification

Hodgkin studied the mechanism of excitability in biological neurons, years before mathematicians discovered the underlying bifurcation mechanisms [15], [19]. He injected DC current on the membrane of the neurons and recorded their spiking behavior as function of step-like increases of the injected current. He observed two main categories in terms of the frequency response of the biological neuron, now known as class of excitability:

- Class 1 excitability: The firing rate of spike events can take arbitrarily low values close to the threshold and increases as the current stimulus increases. A typical range is (2-100 Hz) [15].

- Class 2 excitability: The firing rate of spike events is limited in a certain small frequency band and it is only weakly affected by increasing the current stimulus. A typical range is (150 – 200 Hz) [15].

These two cases, have different neurocomputational properties. Class I excitability can be linked with rate encoding since the strength of the applied stimulus is encoded at the

repetition frequency of spike events. Class II neurons on the other hand, act as thresholders which detect whether a certain signal is present or not. Both properties are important from the scope of neural processing.

These properties can be described effectively by means of the introduced bifurcation mechanisms in the following manner:

- Class I neural excitability: A system is Class I excitable when variation of a single parameter (e.g., DC current stimulus) leads to a SNLC bifurcation, where the resting state is substituted by a stable limit cycle linked to the spiking activity. As the parameter increases, the bottleneck effect caused by the ghost becomes weaker which is linked to the rate encoding attribute.

- Class II neural excitability: A system is Class II excitable when variation of a single parameter (e.g. DC current stimulus) leads to either a supercritical or a subcritical Hopf bifurcation. The frequency range on which spiking rate is limited is linked to the imaginary part of the complex eigenvalues involved. The frequency dictated from the imaginary part is known as the relaxation oscillation (RO) frequency.

Additionally, Class I excitability can be associated also with the homoclinic bifurcation. However, the bottleneck in this case is much weaker, leading to a rapid frequency increase which means that experimentally this case is more difficult to be observed than in the case of the SNLC bifurcation [48]. From this discussion it is obvious, that any system biological, electrical, photonic, chemical, etc. whose dynamical description involves these codimension 1 bifurcations can be used as a neuromorphic node, albeit with different time scales due to the different underlying physical mechanism.

2.3.3 Integrators and Resonators

Another important distinction in neural behavior is in terms of the neuron's response on the frequency of the applied stimulus. In this context, the neurons are separated in two categories; integrators and resonators. This separation is based on a single attribute, namely the absence or presence of sub-threshold oscillations. Integrators present no sub-threshold oscillations, while resonators do. This distinction is so important that multiple other neurocomputational properties are mere consequences of it as it is shown in Figure 2-16.

Integrators

In the context of bifurcations, a neuron is an integrator when it is biased close to a SNLC or a homoclinic bifurcation (shown as saddle-node on invariant circle and saddle-node in Figure 2-16, respectively). In both cases the stable equilibrium that is associated with the resting state is a stable node. This means that the sub-threshold triggering of a system will result in a non-oscillatory (highly dumped) return at the resting state.

The operation of an integrator is presented in Figure 2-17 (right), where the system is biased closed to a SNLC bifurcation. The stable node is related to the equilibrium, whereas the stable manifold of the saddle node defines the threshold. If perturbations place the initial conditions beyond the threshold related manifold, then the trajectory follows the limit cycle and returns back at the equilibrium. This trajectory is known as the spiking trajectory or simply a spike event. When the perturbation is not able to push the orbit beyond the threshold then no spike is observed. Since the resting state is a node, the convergence back to it is exponential. When a spike is triggered, it is impossible at the beginning of its trajectory for other perturbations to generate another one, while it gets easier as trajectory moves gets closer to the resting state. This property is known

as the refractory period. Finally, perturbations can be excitatory or inhibitory when they push the orbit to the manifold or away from it, respectively. Excitatory signals consequently tend to help the neuron reach its threshold condition and generate a spike event, while inhibitory signals do the opposite. To summarize, it can be seen that a simple dynamical description of a SNLC bifurcation, provides all the major functionalities of a biological neuron.

properties	integrators		resonators	
bifurcation	saddle-node on invariant circle	saddle-node	subcritical Andronov-Hopf	supercritical Andronov-Hopf
excitability	class 1	class 2	class 2	class 2
oscillatory potentials	no		yes	
frequency preference	no		yes	
I-V relation at rest	non-monotone		monotone	
spike latency	large		small	
threshold and rheobase	well-defined		may not be defined	
all-or-none action potentials	yes		no	
co-existence of resting and spiking	no	yes	yes	no
post-inhibitory spike or facilitation (brief stimuli)	no		yes	
inhibition-induced spiking	no		possible	

Figure 2-16 : The neural properties of integrators and resonators [15].
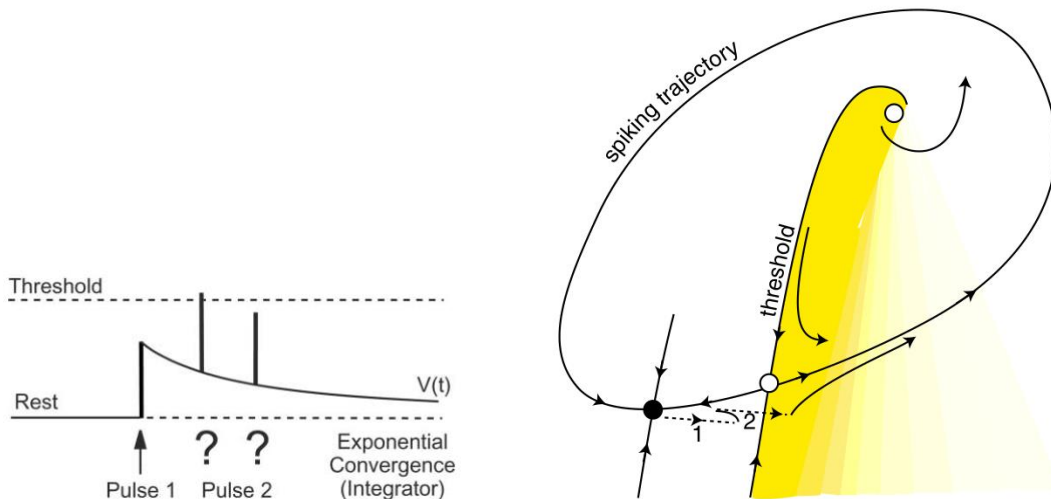
Figure 2-17 : The response of an integrator to pulsed stimulus [12], [49].

Resonators

Resonators are neurons who from a dynamical point of view are biased close to an Andronov-Hopf bifurcation. In this case, the resting state is not a stable node but a stable focus, which means that convergence of the system back to it is accompanied by relaxation oscillations. The frequency of these oscillations f_{res} is associated with the imaginary part of the complex eigenvalues whose real part changes its sign when the bifurcation occurs. In real systems, the presence of noise which constantly adds weak random perturbations of the system's orbit unmasks the oscillation frequency of the

stable focus. This is shown in the experimental results from biological neurons in Figure 2-18 (left).

In the same picture, the case of biasing the system close to a supercritical Hopf bifurcation is illustrated. First of all, it is observed that a perturbation results in a spiral-like decay of the system to its equilibrium. This means that discrete perturbations must be synchronized in order to evoke a spike event. For example in Figure 2-18, after perturbation 1 takes place, a perturbation at 2 will move the system toward the resting point, whereas a perturbation 3 will move the system toward the evolution of a spike event. The temporal difference between perturbations 1 and 2 is close to $\frac{1}{2f_{res}} = \frac{T_{res}}{2}$, whereas the difference between 1 and 3 is close to the $\frac{1}{f_{res}} = T_{res}$. This means that the neuron is sensitive to inputs whose temporal distance is $\Delta t = m T_{res}, \ m = 1,2,\dots$. For this reason, f_{res} is known as the resonance frequency of the neuron and the neuron itself is called a resonator.

Also, since in the case of the supercritical Hopf bifurcation the amplitude of the stable limit cycle increases as the bifurcation parameter increases, there is not a definite limit cycle trajectory. This means that excitations can produce spikes of different amplitudes, but their timing is always dictated by the resonance frequency. This explains the statement in Figure 2-16, according to which resonators do not have an all-or-none action potential. Also, there is not a manifold that clearly separates the region in spiking and non-spiking behavior as in the case of the SNLC, which means that these neurons do not reveal a definite neural threshold, but a threshold region. Inside this region even half-amplitude spikes can be produced as it is shown in Figure 2-18 (right). Finally, inhibitory signals if properly synchronized can also produce spike events, thus making possible the inhibition-induced spiking property.
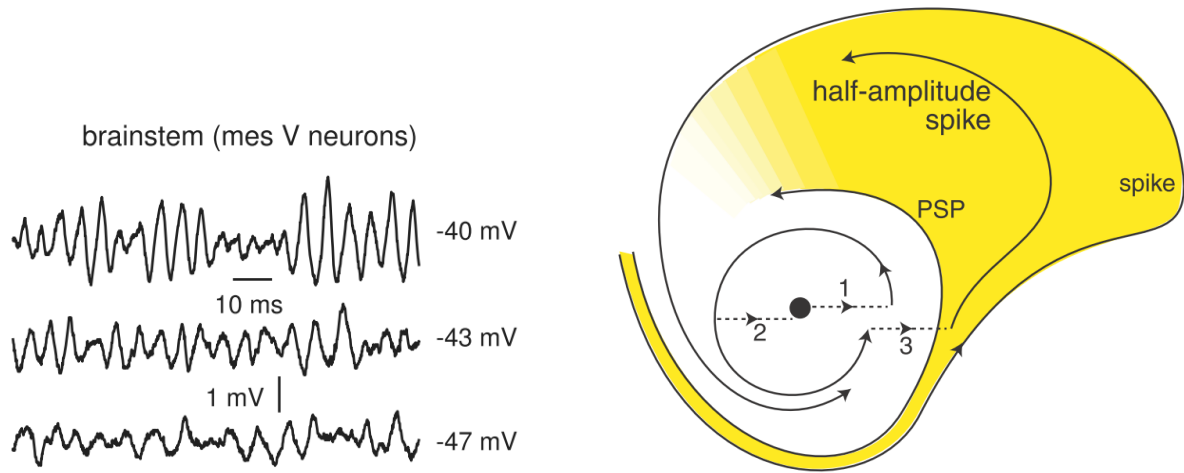
Figure 2-18 : (Left) Experimental results from a biological resonate and fire neuron [12], [15].

Although not as popular as integrators, the resonators can be used for some types of applications such as observing signals of a certain frequency content, by employing their resonant frequency. Moreover, they can be used as a gate for selective communication between different neural groups when combined with burst neurons as it is shown in Figure 2-19.
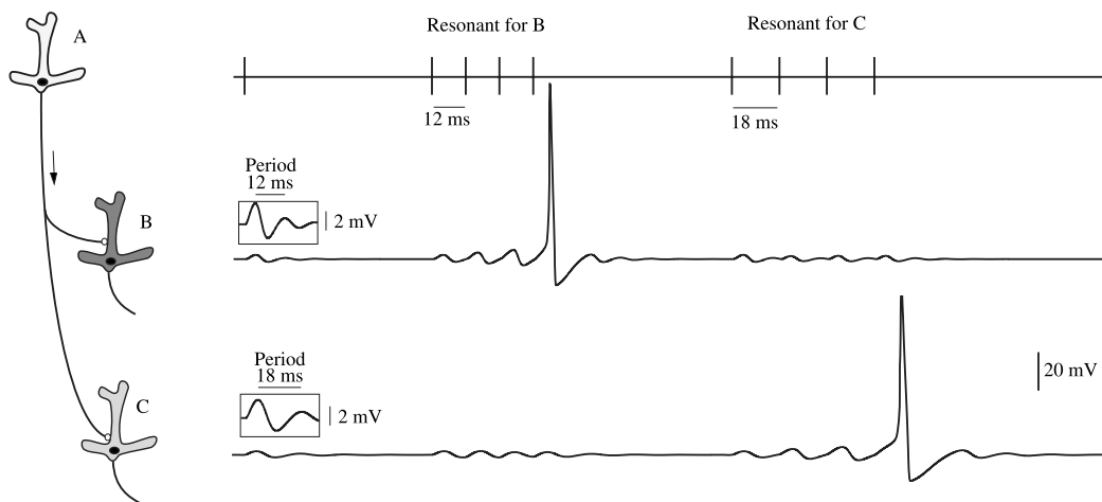
Figure 2-19 : Selective communication between resonators. The neuron A generates spike events whose repetition frequency can be either resonant to the neuron B or the neuron C. In this way neuron A can selectively trigger the neuron B or the neuron C by exploiting their resonate and fire dynamics [15].

2.4   Conclusion

In this chapter, the neuron is presented as a system of non-linear equations. In this way, it is evident that the bifurcation theory is a key tool when the behavior of neurons of the third generation is considered. By biasing the system close to a point where its output changes from a steady one (equilibrium) to a self-pulsating one (limit cycle), it can become excitable and thus act as a neuron. This theory will be used in the following chapters when the laser will be studied as a neuromorphic node. It will be shown that its dynamical description presents the same bifurcation mechanisms, but its different time scales allow for processing speeds that are up to 6 orders of magnitudes faster compared to biological and electronic neurons.

3. SEMICONDUCTOR LASERS

The word laser stands for a particularly important phenomenon in physics; light amplification by stimulated emission of radiation. This key property has left a significant mark on almost any area of modern technology and physics. It would be no exaggeration to state that the advent of laser technology has literally transformed our lives and they will continue doing so for the foreseeable future. There are multiple types of lasers but they all share a common characteristic, namely the amplification of radiation when passing from a suitable material, known as the gain material, inside a reflecting cavity. The gain amplification property also known as stimulated emission was shown first by Einstein in 1916. The first laser was constructed in 1960 by T.H. Maiman, whereas in 1964 the physicists C.H. Townes, N. G. Basov and A. M. Prokhorov shared the Nobel Prize "for fundamental work in the field of quantum electronics, which has led to the construction of oscillators and amplifiers based on the maser-laser principle". Since then, these oscillators and amplifiers have become an integral part of our everyday lives.

In particular, the semiconductor laser, due to its small size, ease of integration and the possibility of electrical pumping with low power consumption, is the building block of many digital systems and telecommunication networks. Moreover, semiconductor based photonic devices can be used except from lasing also for other important operations such as light modulation, light amplification and light emitting diodes.
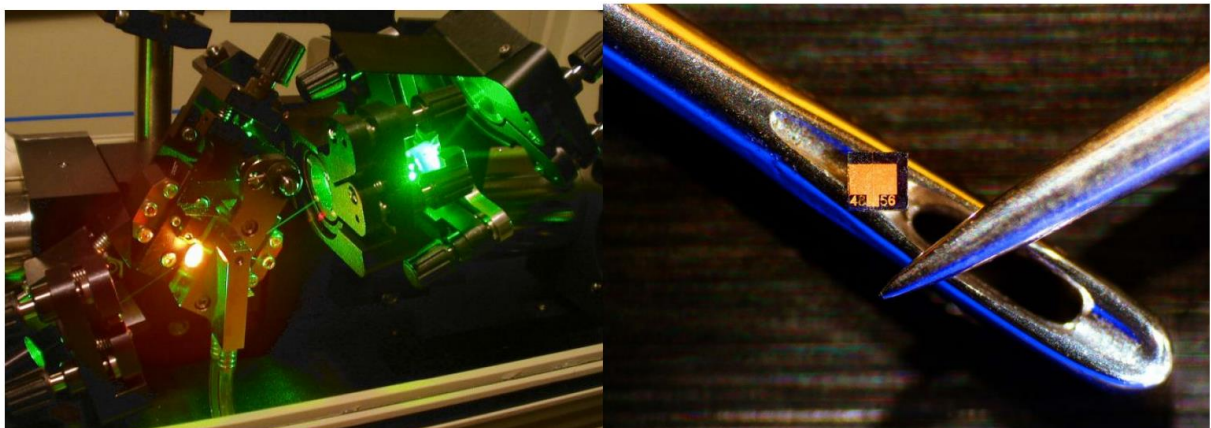
Figure 3-1 : Comparison between a titanium sapphire laser (left) and a semiconductor laser (right) in terms of physical footprint.

Among various semiconductor laser types, quantum dot lasers are excellent candidates for photonic integration due to their low current threshold [50], their high temperature stability [39], [40], the ability for multi-waveband emission [51], [52] and their integrability with silicon platforms [41]. In the following, a short introduction of semiconductor lasers will be provided along with their dynamical description, as well as an overview of quantum dot lasers.

3.1 Light – Matter Interaction

In nature a material in terms of its electrical properties can be classified either as a conductor, an insulator or a semiconductor. The evolution of quantum physics during the 20th century allowed for an energy-based description of these properties. Quantum physics dictate that the energy of each electron can have only discrete (quantum) values. As a result, electrons bounded by the potential field of an atom can take discrete

energy values. However, according to the Pauli principle each energy state can accommodate up to two electrons. Thus, the electrons that are bounded by an atom occupy multiple discrete energy states. Placing multiple atoms close together, leads to their interaction which yields new discrete energy levels due to the Pauli principle. When atoms are tightly closed together as it happens to a crystal structure, the new energy levels are so many that they can be interpreted as quasi-continuous energy bands. This is shown in Figure 3-2.

The electrical properties of a material are determined by the electrons at the valence band. The valence band is the highest energy band that is occupied by electrons at T = 0 Kelvin. When this band is not completely occupied, then the material is a conductor meaning that electrons can easily transition to higher energy states when an electric field is imposed. When the valence band is fully occupied and its energy distance from the next unoccupied band which is known as the conduction band is relatively high, then the material is an insulator. Even for higher temperature, electrons in the valence band cannot transition to the conduction band. When the distance between the conduction and the valence band is short enough ($\lesssim$ 3 eV) for thermal energy alone to cause the transition of electrons from the valence band to the conduction band when T > 0 K, then the material is a semiconductor.

Semiconductors can be classified as direct or indirect. In direct semiconductors the minimum energy state of the conduction band and the maximum energy state of the valence band correspond to the same crystal momentum (k-vector), while in indirect semiconductors this condition does not hold. Only direct semiconductors are efficient for optical transitions since they do not require the change of the crystal momentum for transitions between the conduction and the valence band. The energy diagram of a direct semiconductor is shown in Figure 3-3. In this diagram, the transition of an electron from the conduction band with energy E_2 to the valence band with energy E_1 causes the emission of a photon with frequency v, since $E_2 - E_1 = hv$.
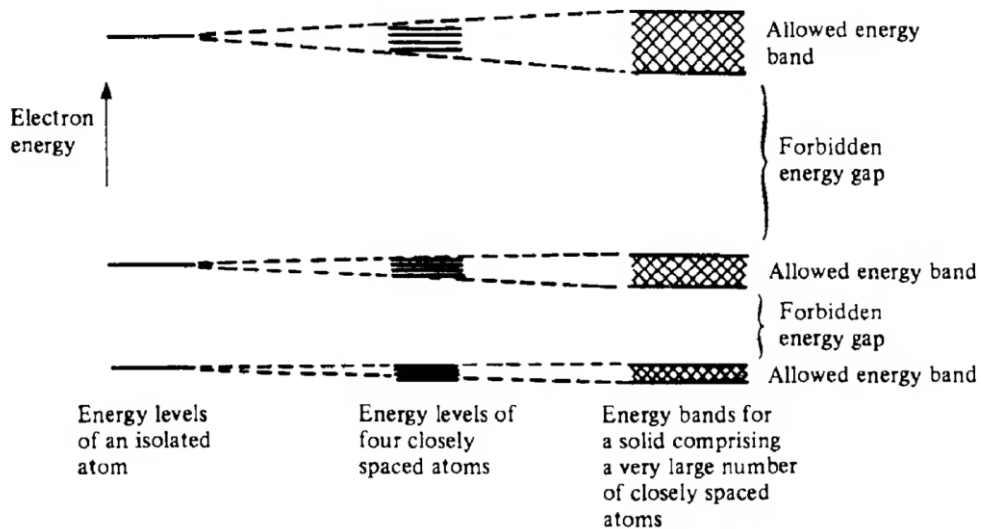
Figure 3-2: The energy levels of an isolated atom (left), four closely spaced atoms (middle) and a very large number of atoms (right). It can be seen that when the number of atoms that are closely spaces is large then the discrete energy levels can be interpreted as energy bands [53].

When an electron transitions from the valence to the conduction band, then it leaves an empty state behind in the form of a positive charge known as a hole. The number of holes in the valence band or electrons in the conduction band can be modified also by adding excess holes or electrons by a process known as doping. In the first case, the

semiconductor is called p – doped (additional holes) and in the second case it is called n-doped (additional electrons) [54].

In thermal equilibrium the electrons in the semiconductor are distributed according to the Fermi distribution [54]. The occupation probability of a given state E_k with wave-vector $\boldsymbol{k}$ is given by the relation:

$$\rho_b(E_k) = \left[1 + \exp\left(\frac{E_{k,b} - E_F}{k_B T}\right)\right]^{-1} \qquad (3\text{-}1)$$

In this relation $b = (c, v)$ where c stands for the conduction band and v for the valence band, k_B is the Boltzmann's constant, T is the temperature and E_F is the Fermi energy which lies inside the energy gap for a semiconductor.
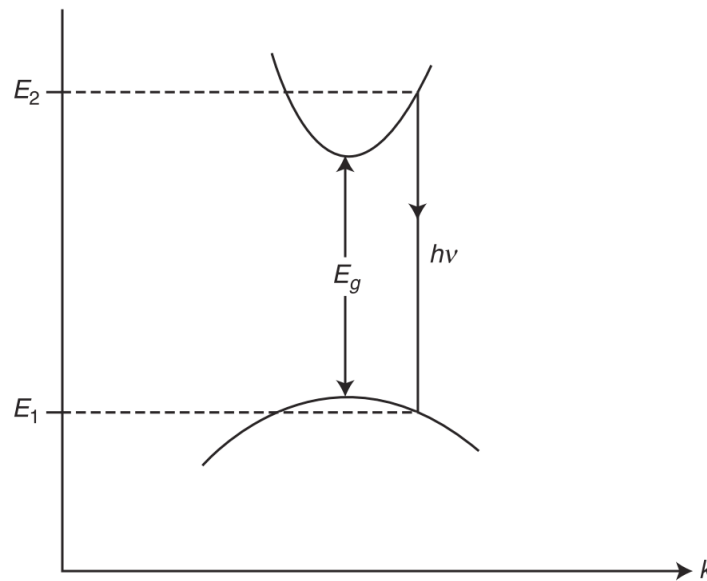
Figure 3-3 : E-k curves for the conduction and valence bands of a direct semiconductor. E_g is the energy gap and $h\nu$ is the energy released from the transition of an electron from the E_2 to E_1 .

Photons interact with the electrons in the semiconductor by aiding them in transitioning from the valence to the conduction band. This process is known as absorption and the probability for such a transition to take place is given by the relation:

$$W_k^{v \to c} = B_k^{v \to c} \, \rho_v(E_k)[1 - \rho_c(E_k)]u(\hbar\omega) \qquad (3\text{-}2)$$

In this relation $B_k^{v \to c}$ gives the transition rate and it is known as the Einstein coefficient. The spectral density of light is given by $u(\hbar\omega)$ at the transition energy. It is obvious from this relation that the transition probability is proportional to the probability of finding an empty state at the conduction band and an occupied state at the valence band.

The inverse process is known as radiative recombination, when an electron at the conduction band transitions to a vacant state at the valence band thus causing the disappearance of a hole. During radiative recombination a photon with energy equal to the energy transition is emitted. Such a transition can occur spontaneously and this mechanism is known as spontaneous emission.

However, there is also the case when an existing photon causes the recombination between an electron and a hole. In this case an identical photon is created after the

recombination and essentially the total optical field is amplified. This second process is known as stimulated emission. The rate of stimulated emission is given by:

$$W_k^{c \to v} = B_k^{c \to v} \rho_c(E_k)[1 - \rho_v(E_k)]u(\hbar\omega) \qquad (3\text{-}3)$$

In this case the Einstein coefficient $B_k^{c \to v}$ is equal to the absorption coefficient $B_k^{v \to c}$. Absorption, spontaneous emission and stimulated emission are shown in Figure 3-4.

(a)   **(b)**   **(c)**

conduction band

$\hbar\omega$ $\hbar\omega$ $\hbar\omega$ $\hbar\omega$

$\hbar\omega$ $\hbar\omega$
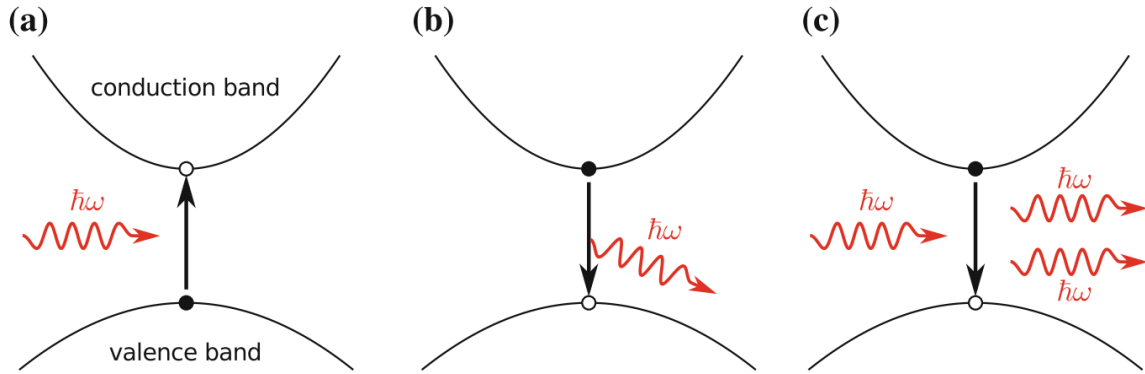
valence band

Figure 3-4 : Illustration of the absorption, spontaneous emission and stimulated emission properties. (a) Absorption of a photon with energy $\hbar\omega$ which results in the transition of an electron from the valence to the conduction band. (b) Spontaneous emission, where an electron in the conduction band relaxes in the valence band thus generating a photon with random phase and direction. (c) Stimulated emission of an identical photon by a passing photon [55].

3.2   Laser as a dynamical system

Lasing is achieved when a material capable of light amplification via the process of stimulated emission is placed between two mirrors (Figure 3-5). When light of frequency v propagates through the material towards the z direction with intensity $I_v^+(z,t)$, its intensity will be modified according to the wave equation:

$$\frac{\partial I_v^+}{\partial z} + \frac{n}{c}\frac{\partial I^+}{\partial t} = g(v)I^+(v)$$

Light traveling to the opposite direction will experience a similar modification to its intensity:

$$-\frac{\partial I_v^+}{\partial z} + \frac{n}{c}\frac{\partial I^+}{\partial t} = g(v)I^-(v)$$

Addition of these equations and the fact that in most lasers there is a very low variation of $I_v^+ - I_v^-$ with z allows for the relation:

$$\frac{dI_v}{dt} = \frac{c}{n}g(v)I_v, \qquad I_v = I_v^+ + I_v^- \qquad (3\text{-}4)$$

In this relation the term $g(v)$ expresses the absorption and stimulated emission properties illustrated in Figure 3-4. When $g(v) > 0$ stimulated emission is the dominant light – matter interaction mechanism and light is amplified, whereas when $g(v) < 0$ the

dominant light – matter interaction mechanism is absorption and light intensity decreases. In order for the material to be amplifying, the number of electrons in the conduction band must be larger than the number of electrons in the valence band since in this case the probability for a photon to generate an additional identical photon via stimulated emission, will be greater than the probability to be absorbed. This condition is known as population inversion and it is simply formulated in the definition of the gain:

$$g(v) = \sigma(N_c^e - N_v^e)L(v)$$

In this relation, σ is defined as the cross-gain coefficient, N_c^e is the number of electrons in the conduction band and N_v^e is the number of electrons in the valence band. The number of holes in the valence band is equal to $N_v^h = N_0 - N_v^e$, where N_0 is the total number of carriers in the valence band. The carriers that react at the application of electric field by freely moving in the crystal are the electrons in the conduction band and the holes in the valence band. By defining the total number of carriers as $N = N_c^e + N_v^h$ the gain becomes:

$$g(v) = \sigma(N - N_0)L(v) \qquad\qquad (3\text{-}5)$$

The term $L(v)$ is the lineshape function which expresses how much the gain of the material is affected by different photon wavelengths. The line-shape function is described by a Lorentzian:

$$L(v) = \frac{\delta v_0}{\pi} \frac{1}{(v - v_0)^2 + \delta v_0^2}$$

The frequency v_0 is equal to E_{gap}/h , where h is the Planck constant and E_{gap} the energy gap of the material defined as the distance between the conduction and the valence band. As a result, when $N > N_0$ the stimulated emission process is dominant and the material acts as an amplifier, otherwise when $N < N_0$ the absorption process is dominant and the material acts as an absorber.
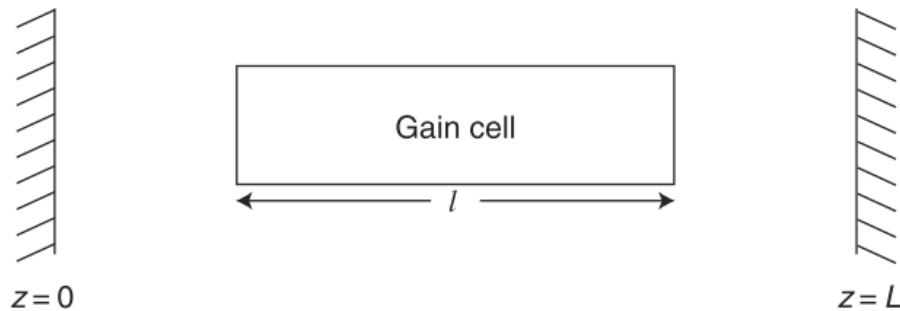
Figure 3-5 : A laser cavity; a stimulated emission-based amplifier placed in a cavity between two mirrors located at $z = 0$ and $z = L$ [54].

However, in order for light amplification to occur, the condition that the material must be amplifying is a necessary but not sufficient condition, since there exist additional propagation losses and the losses at the mirrors. These losses are expressed as

$$g_{losses} = -\frac{1}{2L}\ln(r_1 r_2) + a$$

In this relation r_1, r_2 are the two reflectivities, L the cavity length and a the propagation losses. Usually, one reflectivity acquires a high value (0.99) and the other one a lower value (i.e., 0.3) from where the light is able to escape. For amplification to occur the

population inversion $(N > N_0)$ must be strong enough so as to overcome the cavity losses $g(v) > g_{losses}$. This condition is known as the threshold condition. The intensity I_v is thus expressed by the relation

$$\frac{dI_v}{dt} = \left(\frac{c}{n}g(v) - \frac{1}{\tau_{ph}}\right)I_v \qquad (3\text{-}6)$$

The time constant τ_{ph} is the photon lifetime and it expresses the mean temporal window when a photon is lost due to cavity losses. It is computed as:

$$\tau_{ph} = \left(\frac{c}{n}\,g_{losses}\right)^{-1} \qquad (3\text{-}7)$$

With respect to the carriers, they are described by the relation

$$\frac{dN}{dt} = K - \frac{c}{n}g(v)I_v - \frac{N}{t_{sp}} \qquad (3\text{-}8)$$

The term K is known as the pumping process. This term accounts for the external mechanism that is responsible for generating the desired population inversion $(N > N_0)$. When the system is in thermal equilibrium (K = 0) then the absorption mechanism is dominant. The second term accounts for the light – matter interaction and the third term accounts for carrier recombination due to spontaneous emission.

Equations (3-6), (3-8) describe the laser operation in the form of a 2D nonlinear dynamical system. Solving the system for its equilibrium points yields two solutions. The first solution is associated with zero light intensity:

$$\overline{I_{1,v}} = 0, \qquad \overline{N_1} = K\tau_{sp}$$

The second solution is associated with non-zero light intensity:

$$\overline{I_{2,v}} = \tau_{ph}\left(K - \frac{1}{\tau_{sp}}\left(N_0 + \frac{n}{\tau_{ph}\sigma L(v)c}\right)\right), \qquad \overline{N_2} = N_0 + \left(\frac{n}{\tau_{ph}\sigma L(v)c}\right)$$

By taking the linear approximation of the system (first Lyapunov method) the linear matrix is:

$$A = \begin{bmatrix} \dfrac{cg(N)}{n} - \dfrac{1}{\tau_{ph}} & \dfrac{c}{n}\sigma L(v)I_v \\[3mm] -\dfrac{c}{n}g_v(N) & -\dfrac{c}{n}\sigma L(v)I_v - \dfrac{1}{\tau_{sp}} \end{bmatrix}$$

The eigenvalues of around an equilibrium are given by the characteristic equation:

$$|\lambda I - A| = 0$$

The matrix A around the first equilibrium is calculated by substituting $I_v = \overline{I_{1,v}}$ and $N = \overline{N_1}$. The result is:

$$A_1 = \begin{bmatrix} \frac{c}{n}\sigma L(v)\left(\tau_{sp}K - N_0\right) - \frac{1}{\tau_{ph}} & 0 \\ -\frac{c}{n}\sigma L(v)\left(\tau_{sp}K - N_0\right) & -\frac{1}{\tau_{sp}} \end{bmatrix}$$

There are two solutions to the eigenvalue problem: $\lambda_1 = -1/\tau_{sp}$ and $\lambda_2 = \frac{c}{n}\sigma L(v)\left(\tau_{sp}K - N_0\right) - \frac{1}{\tau_{ph}}$. The first eigenvalue is negative. The second eigenvalue is negative only when $K < \frac{1}{\tau_{sp}}\left(N_0 + \left(\frac{n}{\tau_{ph}\sigma L(v)c}\right)\right) = \frac{\overline{N_2}}{\tau_{sp}} = K_b$. As a result, the pumping process K acts as a bifurcation parameter and the bifurcation point is at K_b.

In terms of the second equilibrium point of the matrix A, the values $I_v = \overline{I_{2,v}}$ and $N = \overline{N_2}$ are used. The result is:

$$A_2 = \begin{bmatrix} 0 & \frac{c}{n}\sigma L(v)\tau_{ph}\left(K - \frac{\overline{N_2}}{\tau_{sp}}\right) \\ -\frac{1}{\tau_{ph}} & -\frac{c}{n}\sigma L(v)\tau_{ph}\left(K - \frac{N_0}{\tau_{sp}}\right) \end{bmatrix}$$

The characteristic equation is:

$$\lambda^2 + \lambda\frac{c}{n}\sigma L(v)\tau_{ph}\left(K - \frac{N_0}{\tau_{sp}}\right) + \frac{c}{n}\sigma L(v)\left(K - \frac{\overline{N_2}}{\tau_{sp}}\right)$$

Setting $\gamma = \frac{c}{n}\sigma L(v)\tau_{ph}\left(K - \frac{N_0}{\tau_{sp}}\right)$ and $\omega_0^2 = \frac{c}{n}\sigma L(v)\left(K - \frac{\overline{N_2}}{\tau_{sp}}\right)$, the solution to this equation is:

$$\lambda_{1,2} = -\frac{\gamma}{2} \pm j\sqrt{\omega_0^2 - \frac{\gamma^2}{4}}$$

For definitiveness it is assumed that $\omega_0 > \gamma/2$. Physically meaningful solutions of the intensity correspond to $K > K_b$, since $\overline{I_{2v}} = \tau_{phi}(K - K_b)$. As a result, it can be seen that $\mathcal{R}(\lambda_{1,2}) < 0$ always holds for $K > K_b$. The equilibrium is a stable focus since it is described by two complex eigenvalues. When perturbed, the system will return to its steady state via relaxation oscillations (RO) with decay rate dependent on the dumping factor γ and their frequency being equal to

$$f_{RO} = \frac{\omega_{RO}}{2\pi} = \frac{1}{2\pi}\sqrt{\omega_0^2 - \frac{\gamma^2}{4}} \qquad (3\text{-}9)$$

These results reveal the most important characteristics of lasers. First of all, when the pumping strength, whose role is to cause the population inversion, is lower than a critical value K_b then the population inversion is not strong enough so as to overcome the cavity losses and light experiences attenuation which means that its intensity converges to 0. In reality the intensity is never equal to 0, since there are always some photons generated via the process of spontaneous emission. Increasing the pumping strength causes an increase at the number of electron – hole pairs N.

For pumping higher than the critical value K_b, the population inversion is sufficiently strong to overcome cavity losses and photons are amplified by the stimulated emission

process. Spontaneous emission is the mechanism responsible for these photons. The optical frequencies to be amplified are determined by the standing wave condition:

$$v_m = \frac{mc}{2nL} \tag{3-10}$$

In this case, L is the cavity length and n is the refractive index of the gain material. These optical frequencies are known as longitudinal modes. The frequency spacing between these modes is known as the free spectral range (FSR) and is defined as:

$$FSR = v_{m+1} - v_m = \frac{c}{2nL} \tag{3-11}$$

Since K_b is a function of the optical frequency via the Lorentzian $L(v)$, different modes will present different lasing thresholds. The central mode is the mode that experiences the higher gain. Once the condition $K > K_b(v)$ is satisfied for a mode, then additional pumping will result in an increase to the value of its intensity. With respect to the carriers, their number remains constant and equal to N_0 a condition known as gain clamping, since in this case the total gain cannot be further increased.

3.3 Diode Lasers

In a diode laser, the gain material arises from the interaction between a p – doped and an n – doped semiconductor of direct bandgap (III- VI materials). A typical sketch of a diode laser is shown in Figure 3-6.
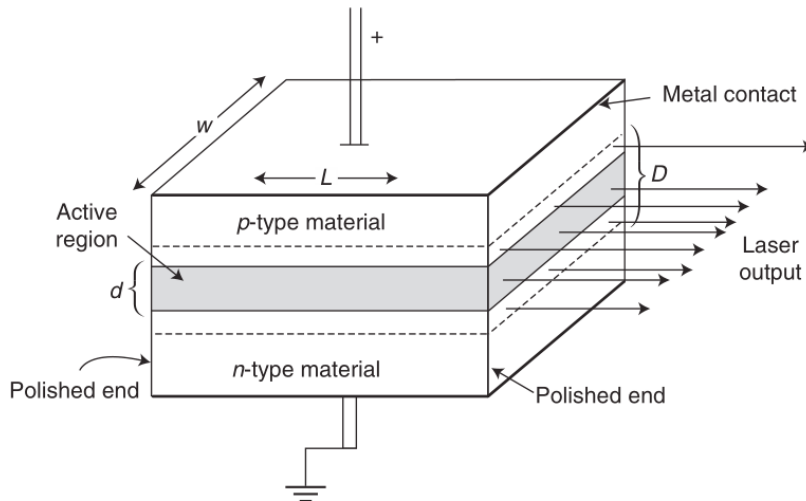
Figure 3-6: A diode laser (homojunction design) [54].

The interaction between the p-doped and n-doped material result in the formation of a region between the p-doped and the n-doped material known as the depletion region. In this region, electrons recombine with holes due to the diffusion process thus causing a region depleted of carriers. This process results in the formation of positive ions at the side of the p-type material and negative ions at the side of the n-type material and thus the occurrence of an internal electric field. This field acts as a barrier for further recombination of carriers and the system reaches an equilibrium state maintained by these two opposing forces; the diffusion process and the internal field. Applying a

current injection by forward biasing the device leads to weakening of the barrier field along with a flow of carriers (electron-hole pairs). The flowing carriers can recombine radiatively inside the depletion region which effectively acts as the gain region. The injected current acts in this case as the pumping mechanism.

In this scheme, mirrors are not needed since the refractive index difference between cleaved semiconductor facets and the air allows for sufficiently high reflectivity. The first diode laser devices were homojunctions such as the one shown in Figure 3-6. The problem with this device is the low confinement of carriers caused due to the strengthened diffusion process. Thus, the first diode lasers required extremely high injection current. The solution came with the advent of heterostructure materials. The lasing material (i.e., GaAs) in this case is confined between a different material with higher bandgap (i.e., AlGaAs), thus leading to a strong restriction of carriers in the active region and subsequently the first demonstration of a diode laser operating at room-temperature (Alferov).

Further improvements have been achieved by adding a separate confinement heterostructure (SCH). In this case, additional layers are deposited on either side of the active region so as to strongly confine the electrons in this region by means of the increased refractive index difference. Moreover, decreasing the width of the active material below the de-Broglie wavelength of electrons (a few nm) results in the formation of a quantum well (QW). This localization strongly increases the efficiency of laser-diodes by confining the electrons in two dimensions, thus greatly reducing the current threshold and the power efficiency. Almost all modern diode lasers are QW structures. Confinement in one additional dimension leads to the formation of quantum wires, whereas confinement in all three dimensions leads to a quantum dot (QD). These different charge-carrier confinement approaches are illustrated in Figure 3-7.

3.4 Quantum Dot Lasers

QD lasers are the final step in the succession of methods for more efficient confinement of charge-carriers. In particular, the higher efficiency of QD active materials along with their key properties such as multi-waveband emission is due to their similarity to atoms.
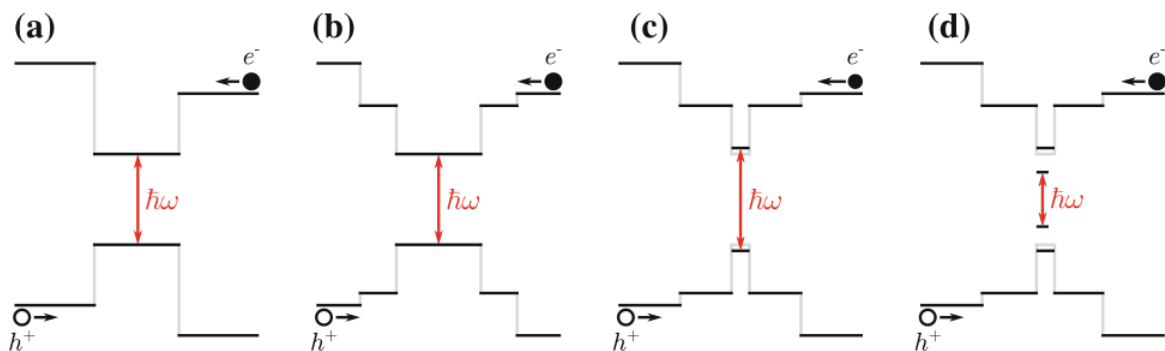
Figure 3-7 : Progression of carrier-confinement methods: (a) heterostructure, (b) separate confinement heterostructure, (c) quantum well, (b) quantum dot [55].

The gain in a general laser is given by (3-5). The number of electrons and holes in the conduction and valence bands is directly proportional to the density of states (DOS). The higher the value of the DOS that is associated with the recombination of carriers due to stimulated emission, the higher the efficiency of the device since in this case the population inversion will be easier to be achieved. It can be seen in Figure 3-8, that a

change in dimensionality leads to different type of the DOS function. In the case of QDs, the DOS is defined at specific energy values and it is particularly high compared to the other cases. This effect has some important consequences compared to QW and 3d-bulk materials ; (a) population inversion can be achieved for lower current injection resulting in improved power efficiency, (b) filling of the next energy level known as the first excited state is achievable for reasonable pumping strength which leads to dual – waveband emission and (c) the separation between the energy states makes the thermally induced transitions between different energy values harder thus leading to improved thermal stability [56].
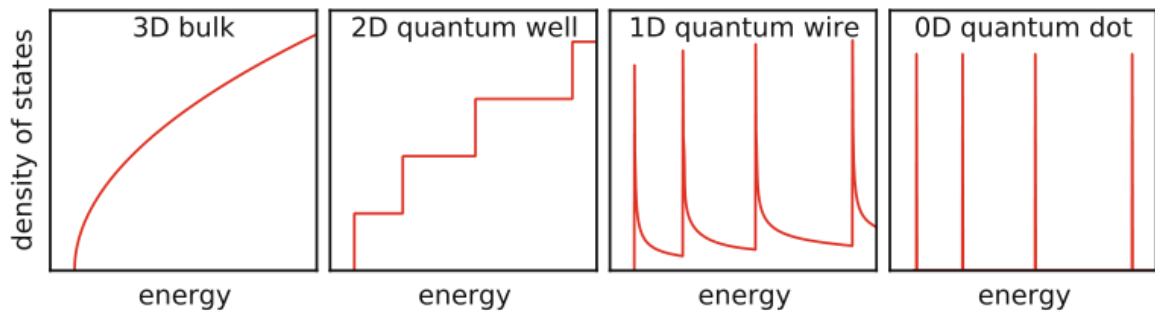
Figure 3-8 : Density of states for 3D bulk, quantum well, quantum wire and quantum dot structures [55].

QD lasers are fabricated by using the Stranski-Krastanov technique [57], [58]. In detail, in the case of an InGaAs QD laser, the SCH structure is a GaAs substrate upon which a thin InAs layer is deposited which forms a QW. The lattice mismatch between the lattice constant of the two materials leads to the emergence of small pyramidal structures. An additional growth of InGaAs at this point leads to an InGaAs QW with embedded InAs QDs. The whole process is illustrated in Figure 3-9.

The result is known as a dot-in-a-well (DWELL) structure. The surface density of QDs in the InGaAs ranges between $10^9 \ cm^{-2}$ and $10^{11} cm^{-2}$ [59]. However, even in the case of a large surface density, the optical gain is quite low which means that the emitted power is weak. The most efficient way to solve this issue is the fabrication by means of epitaxy of additional QD layers upon the previous one. Thus, the total surface density is increased thus leading to higher gain and thus higher output power.

Figure 3-9 : The Stranski – Krastanov method. Growth of a InAs thin layer upon a GaAs substrate by means of epitaxy. The height of the InAs at this point is equal only to a few atoms (left). Further growth leads to the spontaneous emergence of isolated pyramidal islands known as QDs (middle). Overgrowth of these islands with a InGaAs layer flattens then QDs and results in a DWELL structure [55].

The energy diagram of a QD laser is illustrated in Figure 3-10. The atomic – like energy diagram of QDs leads to two discrete energy states with lower energy values compared

to the energy states in the QW layer. The lowest one is known as the ground state (GS), whereas the higher one is known as the first excited state (ES). The GS has a degeneracy of 1, whereas the ES has a degeneracy of 2 or 3, thus allowing for the accumulation of twice or thrice as many carriers compared to the GS. The pump current creates electron hole pairs in the WL, which relax towards the GS and the ES. In contrast to the QW layer, where the energy states are very closely spaced and thus the inter-band dynamics can be neglected, in the case of the GS and the ES the large energy separation leads to noticeable transition dynamics between the GS and the ES. These transition rates are known as the scattering rates and depend both at the occupation probabilities of the energy states and their spacing. Since these transition times range between 0.1 – 10 ps they cannot be neglected. The inter-band dynamics in this case play a crucial role in the behavior or the QD laser structure. Finally, since electrons and holes have different effective masses, the energy spacing between the electrons in the conduction band is smaller than the energy spacing between the holes in the valence band, which leads to an asymmetry in carrier dynamics. However, it is a common strategy to treat in simulations electrons and holes as a pair called exciton by neglecting the hole dynamics due to the fast thermalization in the valence band. In this case the assumption is made that the occupation probability of holes follows the occupation probability of electrons and thus $\rho_e^m = \rho_h^m$, m = GS, ES. This is known as the excitonic approach and has been successfully employed to model QD lasers [60].
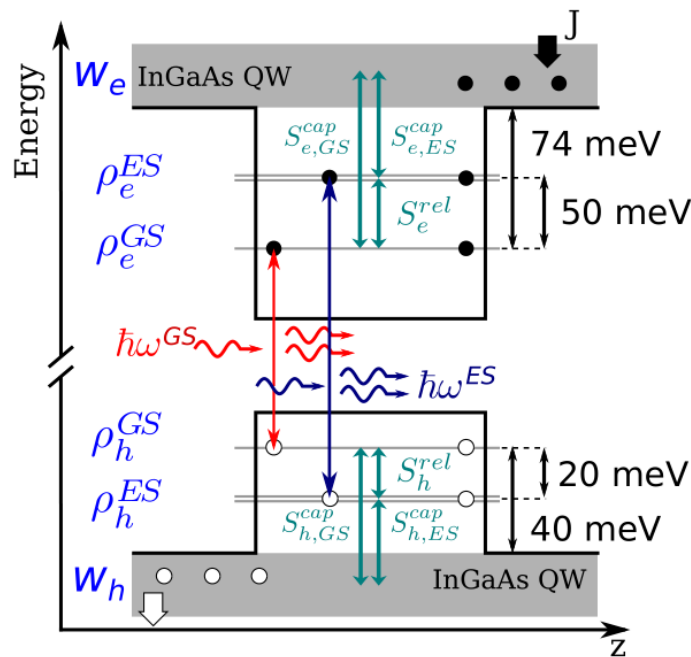
Figure 3-10 : Energy diagram of the scattering processes and light – matter interaction of the QD model. J **is the current injection,** ρ_b^m **the occupation probabilities where** $b = e, h$ **for electrons and holes and** $m = ES, GS$. w_b **is the occupation probability at the QW. There is an asymmetry in energy spacing between electrons and holes due to their different effective mass. The ES shows a degeneracy of two [61].**

With respect to light – matter interaction, the QD laser can emit from both GS and ES. The lasing threshold for each level is a function of multiple parameters, like the photon lifetime, the number of QD layers and the scattering rates. The dependence of two-state lasing on photon lifetime is shown in Figure 3-11 [62], which examines the two-state lasing inside a current injection range from 220 to 710 A/cm^2 as a function of the cavity length. The photon lifetime is directly proportional to the cavity length. For a low cavity length, lasing cannot occur since the maximum gain cannot overcome the cavity losses. As the cavity length increases, which translates in increased number of QDs and higher

photon lifetime, only ES lasing is possible. This happens since the maximum gain of the ES level is two times higher than the maximum gain of the GS due to its higher degeneracy. As a result, there is a range of photon lifetimes where GS lasing is not possible since it cannot overcome the cavity losses, whereas the threshold condition is satisfied for the ES. Further increase of the photon lifetime and QD number by increasing the cavity length leads to two state lasing ($l = 1.5\ mm$) since the GS lasing condition can be satisfied. As the cavity length further increases, the increased number of QDs leads to the termination of the ES lasing. This effect can be attributed to the decreased occupation probability at the GS level when its lasing condition is satisfied. This decrease leads to a higher flow of carriers from the ES to the GS. These extra carriers are radiatively recombined at the GS thus yielding increased GS emission. The ES due to this loss of carriers at some point is unable to satisfy the lasing condition and switches off. Of course, the application of higher current injection can populate substantially the ES level and thus two state lasing can be observed.
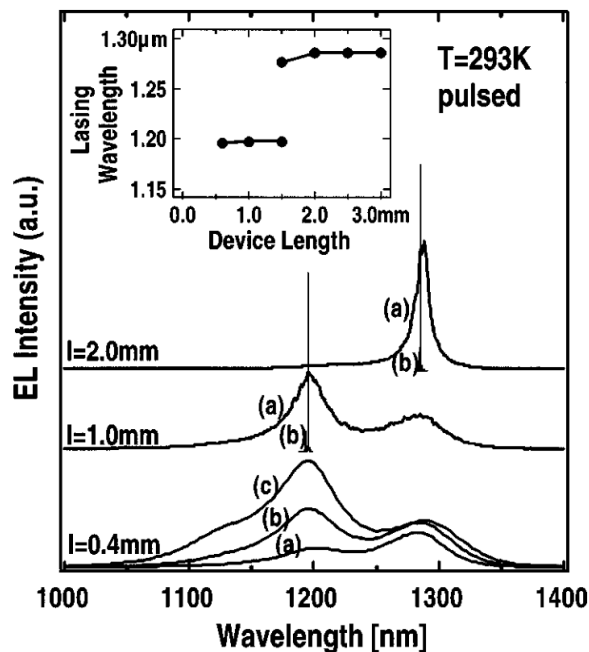
Figure 3-11 : Dependence of GS and ES lasing on the cavity length in room temperature. The lines on the bottom show spontaneous emission spectra for $l = 0.4\ mm$ and current densities equal to (a) $220\ A/cm^2$, (b) $390\ A/cm^2$, (c) $710\ A/cm^2$. The upper lines show GS and ES lasing for (a) slightly below and (b) slightly above the threshold for $l = 1\ mm, l = 2mm$ respectively. The inset shows the dependence of lasing wavelength on the cavity length [62].

A typical power – current characteristic is shown in Figure 3-12 [62]. A peculiar effect is observed at the onset of ES emission, namely the GS emission is decreased. This phenomenon is known as the GS quenching effect and it is attributed mainly to the asymmetrical electron – hole dynamics [52], [61] as well to the increase of the Lorentzian linewidth (homogeneous broadening) with current injection [60].

Finally, with respect to the scattering rates, the lower the relaxation time from the ES to the GS, the higher the ratio between the ES and the GS threshold as it is shown in Figure 3-13 [63]. In the same figure it can be seen that the overall ratio becomes lower as the cavity length decreases, due to the decreased photon lifetime.

An additional notable characteristic of QD lasers that should be considered is the inhomogeneous broadening [64]. During the Stranski – Krastanov process the QD islands which are formed upon the InAs QW vary in size. Since these islands act as

artificial atoms, different sizes dictate different energy bandgaps and consequently different emission wavelengths. This variation with respect to the emission wavelength is known as the inhomogeneous broadening (see Figure 3-14) and it is described by a normal distribution which is given by:
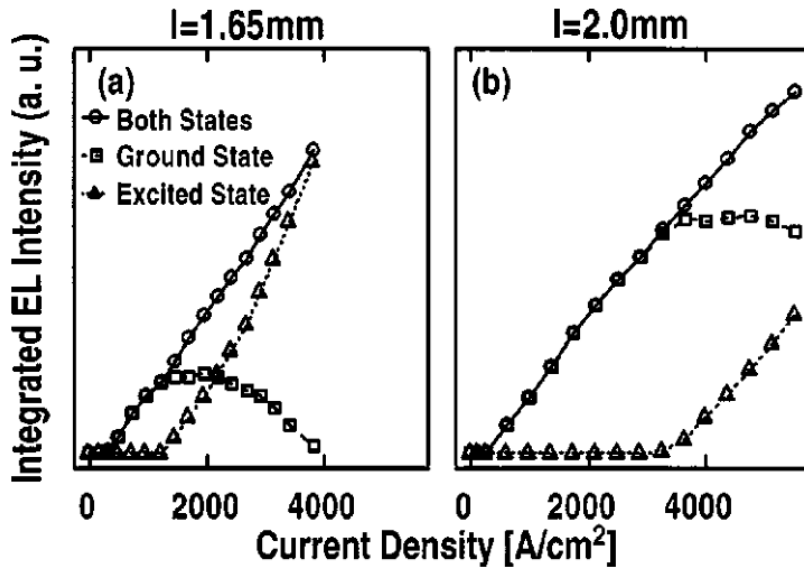
Figure 3-12: Power – Current characteristic for (a) $l = 1.65\ mm$**, (b)** $l = 2\ mm$**. In both cases GS lasing occurs first whereas ES lasing presents a higher threshold current. When ES lasing takes place, further current injection leads to a decrease of the GS emission due to the GS quenching effect [62].**

$$G(\omega^m) = \frac{1}{Z}\exp\left(-\frac{(\omega^m - \omega_{ctr}^m)^2}{2\sigma_0^2}\right)$$

$$\sigma_0 = \frac{\Gamma_{inhomo}}{2.35}$$

(3-12)
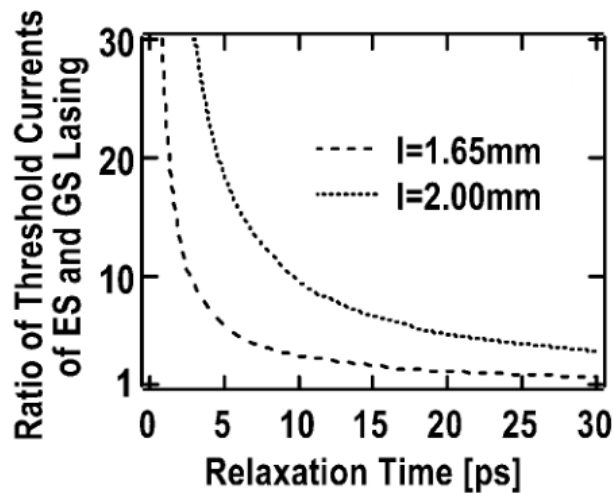
Figure 3-13: The ratio of threshold current of ES and GS lasing as a function of the relaxation time from the ES to the GS [63].

In this relation ω^m is the angular frequency of emitted photons which varies with QD size for m = GS, ES, ω_{ctr}^m is the mean angular frequency which corresponds to mean QD size and σ_0 is the standard deviation which is directly proportional to the inhomogeneous broadening Γ_{inhomo}. The inhomogeneous broadening is defined as the full width at half maximum (FWHM) of the Gaussian. The factor Z is a normalization factor in order to achieve the relation $\int_0^\infty G(\omega^m)d\omega^m = 1$.
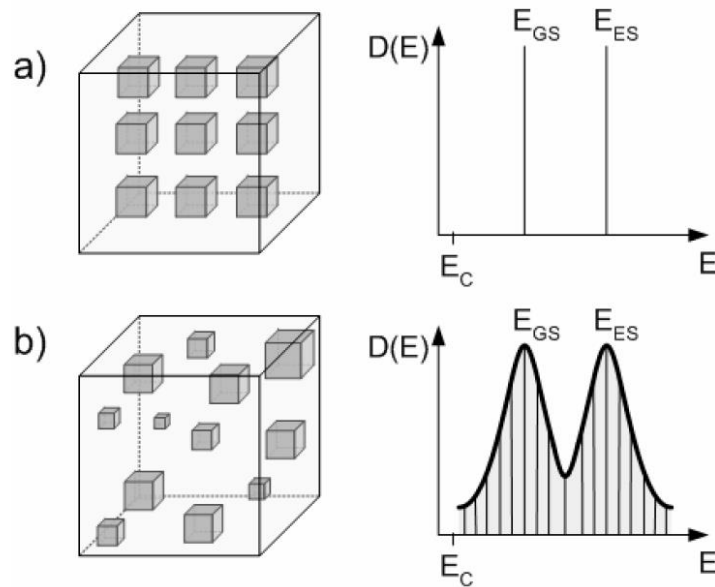
Figure 3-14 : The effect of the inhomogeneous broadening on the DOS function. (a) The case of an ideal QD laser where all dots have identical size, (b) the case of a real QD laser where a variation is observed with respect to the dot size [64].

3.5 Quantum Dot Lasers as Neuromorphic Nodes

In literature, it has been successfully demonstrated that QD Lasers can operate as neuromorphic nodes. In [65], a single mode QD laser operating under external optical injection has revealed integrate and fire dynamics. In particular, light emitted from an external QD laser (master laser; ML) was injected in another QD laser (slave laser; SL), while controlling the injection strength and the frequency detuning between the two lasers. In this experimental setup, the injection strength and the frequency detuning act as bifurcation parameters. When the injection strength is strong enough, the SL is frequency locked to the ML, which means that the difference between the phase of the ML and the SL is constant. At this point, the output of the SL is constant (CW) – the system is under equilibrium. By decreasing the injection strength, there is a bifurcation point that marks the unlocking of the SL from the ML and a transition from CW operation to complex oscillatory dynamics. When the detuning between two lasers is negative ($\omega_{ML} < \omega_{SL}$), this dynamical transition is associated with a SNLC bifurcation, which is linked to the integrate and fire dynamics. The QD lasers in this experiment emit only from a single waveband (GS). In Figure 3-15, the recordings on the oscilloscope are presented for two different bias conditions. From this recording it can be seen that both single and double spikes have been recorded.

In another work [42], the study of a QD laser diode revealed a new important neural attribute that can be achieved all-optically in QD laser by employing the dual waveband dynamics. This attribute refers to excitatory and inhibitory dynamics, which in this context can be linked to emission from the GS or the ES level. The experimental setup

consists of two multimode two-section lasers, with a small portion (15 %) of the active material being reverse biased so as to act as a saturable absorber and the rest (85 %) being forward biased so as to act as a gain material. The whole setup is presented in Figure 3-16.

(a) Single pulse
(b) Train of double pulses
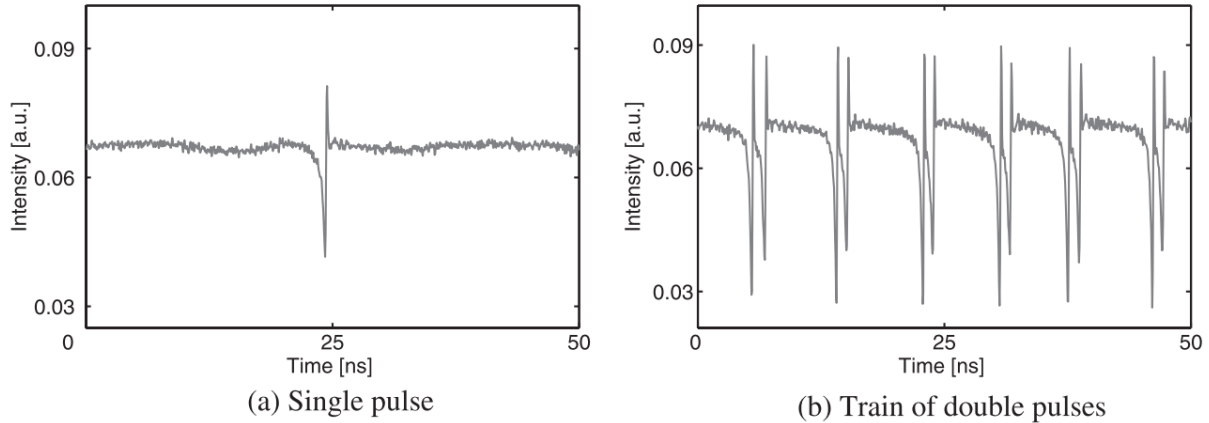
Figure 3-15 : Spiking events recorded from a QD laser under external optical injection: (a) a single spike event, (b) double spike events [65].

The ML is in mode-locked operation thus emitting picosecond pulsations in a fixed firing rate which is dictated by the FSR of the cavity [54]. The SL is biased by controlling the reverse bias voltage and the current injection. These two parameters act as bifurcation parameters. The excitatory neuron is realized when the laser is biased so as to emit only from the ES while the GS is suppressed (Figure 3-17). However, no ES emission can be recorded at the output, since an external waveband filter (WF) is used that blocks the ES emission and permits the only transmission of the GS emission associated with excitatory signals. On the other hand, the inhibitory neuron is realized when the laser is biased so as to emit only from the GS while the ES emission is still below its threshold. Analogously to the previous case, a WF filter is used that blocks GS emission and allows only the transmission of the ES emission associated with inhibitory signals.
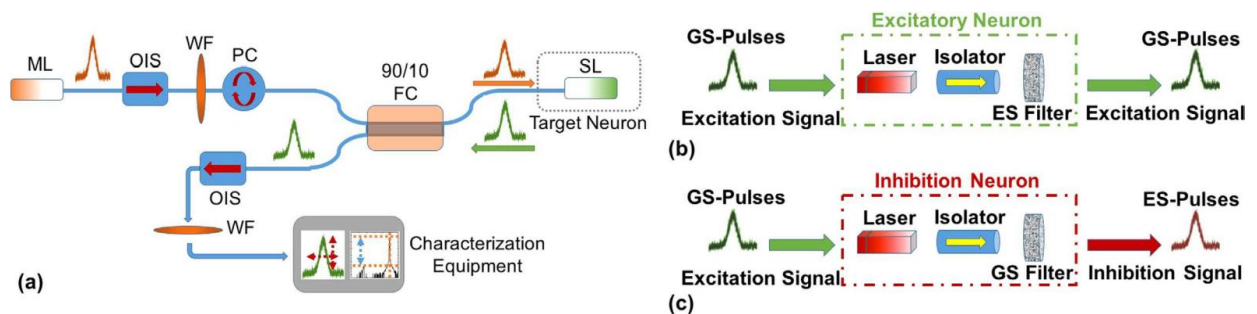
Figure 3-16 : (a) The experimental setup: ML/SL correspond to the master and the slave laser, OIS to the optical isolator, PC is the polarization controller, FC the fiber coupler and WF are waveband filters. (b) An excitatory neuron, triggered by GS spike events and generating GS spikes. An ES filter is used to block ES emission. (c) An inhibitory neuron, triggered by GS spike events and emitting ES spikes. A GS filter is used to block GS emission [42].

In the case of the excitatory neuron, external GS optical injection suppresses the ES emission and evokes GS emission. Thus, GS emission is recorded at the output. On the other hand, when ES optical injection is applied the ES emission is enhanced and the GS spontaneous emission is further suppressed. Thus, the SL is moved further away

from the onset of GS lasing. External GS injection can be associated with an excitatory signal as it enhances GS emission from the SL, whereas external ES injection can be associated with an inhibitory signal since it inhibits GS emission from the SL. The excitatory neuron can emit only from the GS due to the WF which means that it can emit only excitatory signals.

In the case of the inhibitory neuron, external injection from the GS leads to suppression of the GS and emission from the ES. External injection from the ES leads to a similar result. Thus, in this case, both excitatory and inhibitory inputs achieve an inhibitory output. However, in most SNNs, inhibitory neurons receive only excitatory inputs which means that the presented setup is sufficient to be used in more complex neural networks.
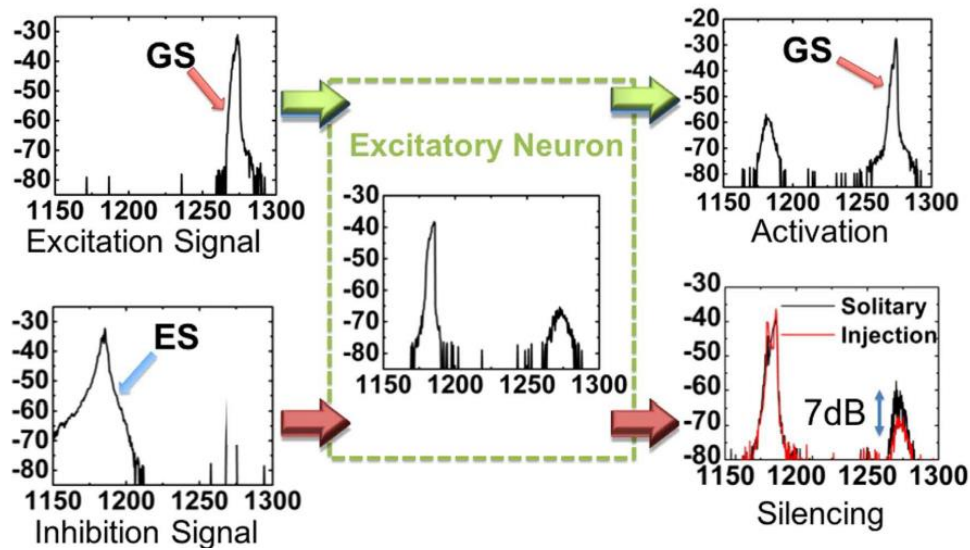
Figure 3-17: The excitatory neuron. Under no triggering only ES lasing is possible. When GS triggering occurs, the ES lasing is suppressed and GS emission is possible, whereas when ES triggering occurs a silencing of the GS occurs (7 dB reduction) [42].
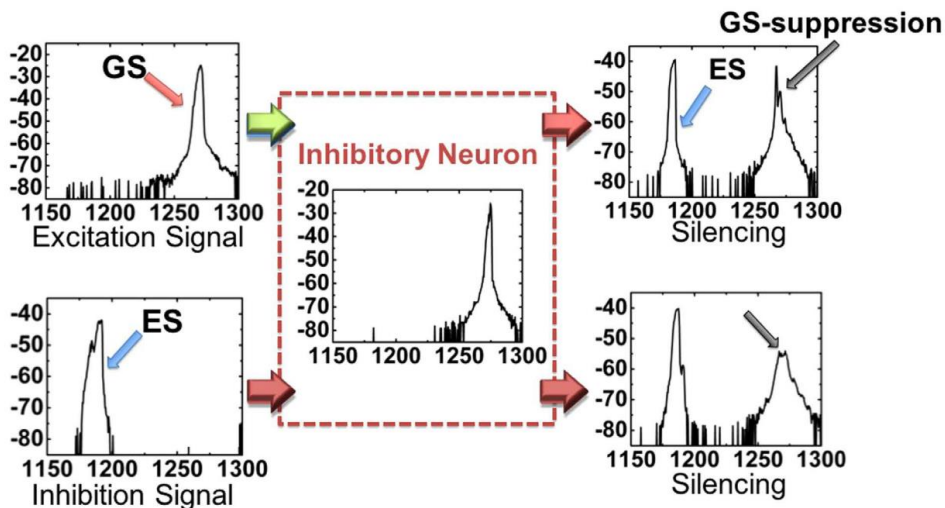
Figure 3-18 : The inhibitory neuron. Under no triggering only GS lasing takes place. When GS triggering is applied, GS lasing is suppressed and ES lasing takes place. On the other hand, when ES triggering is applied a suppression of the GS lasing is observed along with ES emission [42].

In terms of the laser dynamics, the saturable absorber results in a region of self-pulsations between the sub-threshold lasing operation and the stable lasing operation. The transition from non-lasing to self-pulsations is via either a Hopf bifurcation or a

saddle homoclinic bifurcation [66]. The authors suggest that in this setup, the transition is via a saddle homoclinic bifurcation which means that the neuron exhibits integrate and fire dynamics. These dynamics are presented in the case of the excitatory neuron in Figure 3-19. In Figure 3-19.(a) a mode-locked pulse is presented which triggers the SL. In Figure 3-19.(b) the output of the excitatory neuron is shown with an inter-spike period equal to 4 ns for 20 GHz repetition frequency of the mode – locked pulses. In Figure 3-19.(c) another ML is used that produces mode-locked pulses with 10 GHz thus leading to the generation of spike events with an inter-spike period equal to 8 ns. In this case, the increase by a factor of two of the mode-locked frequency leads to the decrease by the same factor of the inter-spike period. Thus, the system exhibits rate encoding. In Figure 3-19(d), a spike event is presented of 4 ns temporal width. The spike event is the envelope of mode-locked pulses generated by the SL. In Figure 3-19.(e) the mean amplitude of the spike events is presented as a function of the mean injected optical power. The neural threshold is observed at an optical power slightly below 1 mW. In Figure 3-19.(f) a time trace of both the GS and the ES emission is presented during the generation of a spike event. It can be seen that external GS triggering suppresses ES emission and leads to the onset of GS emission in the form of a spike event.
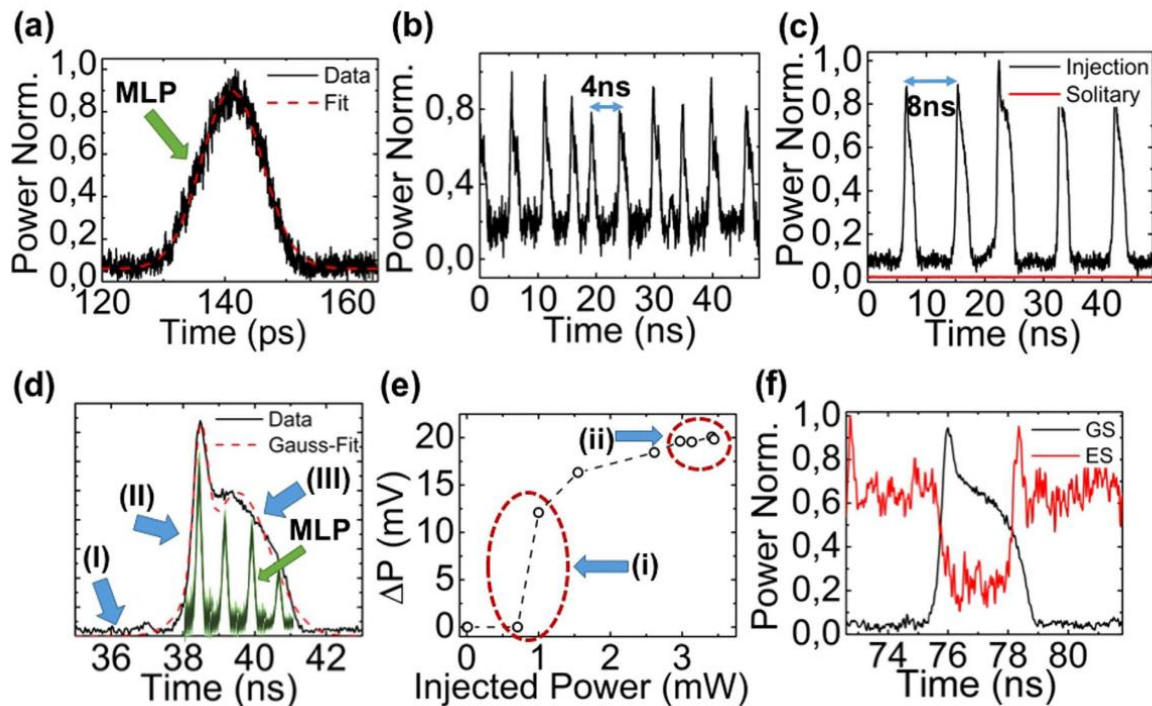
Figure 3-19: (a) Mode – locked GS pulse of 10.6 ps duration. (b) Time trace of an excitatory neuron under GS external optical injection from a ML producing mode-locked pulses with 20 GHz repetition frequency. (c) Time trace from the same excitatory neuron under external GS optical injection from a different ML which produces mode-locked pulses with 10 GHz repetition frequency. (d) Magnification of a single spike event which highlights the different regimes and which included the underlying mode-locked pulses. (e) The spike amplitude as a function of the average injected power. (f) Time trace revealing the suppression of ES emission and the generation of a GS spike event as a result when the SL is triggered by GS mode-locked pulses [42].

In the next chapter, the dual-waveband dynamics of the QD laser will be analyzed by simulating a single section device under optical injection similarly to [65]. The goal is to present for the first time a full study of the spiking dynamics from a QD device emitting from both the GS and the ES state. This analysis will reveal the physical mechanism

behind the inhibitory and excitatory dynamics presented in [42] and will shed additional light in hidden capabilities of the QD laser as a neuromorphic node.

4. DYNAMICAL ANALYSIS OF A SINGLE SECTION QUANTUM DOT LASER UNDER OPTICAL INJECTION

4.1 The Quantum Dot Laser Model

In this chapter simulation results are provided for the operation of a single section QD laser. For simplicity, only a single lasing mode per state is considered which can be easily achieved by adding suitable Bragg grating on the device [53]. Additionally, the inhomogeneous broadening is ignored since in the case of single mode lasing per state, it describes only the lowering of the maximum gain which can be also regulated through other parameters in the simulation environment, while at the same time preserving the simplicity of the system. The topology is a master – slave (ML, SL) optical injection scheme similar to the one presented in [65]. However, in our case we study lasing from both the GS and the ES levels. The equations describing the QD laser carrier dynamics are:

$$\frac{dN_{WL}}{dt} = \frac{I}{qV_w} + \frac{N_{ES}(1 - f_{WL})}{\tau_{ES \to WL}} - \frac{N_{WL}(1 - f_{ES})}{\tau_{WL \to ES}} - \frac{N_{WL}}{\tau_{spon}^{GS}} \qquad (4\text{-}1)$$

$$\frac{dN_{ES}}{dt} = \frac{N_{WL}(1 - f_{ES})}{\tau_{WL \to ES}} + \frac{N_{GS}(1 - f_{ES})}{\tau_{GS \to ES}} - \frac{N_{ES}(1 - f_{WL})}{\tau_{ES \to WL}} \qquad (4\text{-}2)$$
$$- \frac{N_{ES}(1 - f_{GS})}{\tau_{ES \to GS}} - \frac{N_{ES}}{\tau_{spon}^{ES}} - \frac{g_{ES}^0(2f_{ES} - 1)}{1 + \epsilon_{ES}S_{ES}} S_{ES}$$

$$\frac{dN_{GS}}{dt} = \frac{N_{ES}(1 - f_{GS})}{\tau_{ES \to GS}} - \frac{N_{GS}(1 - f_{ES})}{\tau_{GS \to ES}} - \frac{N_{GS}}{\tau_{spon}^{GS}} - \frac{g_{GS}^0(2f_{GS} - 1)}{1 + \epsilon_{GS}S_{GS}} S_{GS} \qquad (4\text{-}3)$$

In these equations N_{WL}, N_{ES}, N_{GS} are the carrier densities at the WL, the ES and the GS levels respectively. The occupation probabilities $f_{x=WL,ES,GS}$ are given by $f_x = N_x/N_{cx}$, where N_{cx} is the total carrier density in each state. In the QD states (GS, ES) the total carrier density is $N_{cx} = 2D_n^x N_D/H_{WL}$, where D_n^x is the degeneracy of each state, N_D is the surface density of QDs per QD layer and H_{WL} is the height of the QW. The number 2 accounts for the electron spin. In the WL the total carrier density is given by the density of states of the 2-dimensional QW structure, namely $N_{cx} = (m^* K_b T)/(\pi \hbar^2 H_{WL})$ where m^* is the exciton effective mass, K_b is the Boltzmann constant, T the temperature and $\hbar$ the bar Planck constant. In (4-8) the first term corresponds to the pumping rate, where I is the applied current, q is the electron charge and $V_w = n_l W H_w L$ is the total volume of the QWs. Here n_l is the number of QD layers, W is the device width and L is the length of the device.

The scattering rates between the X and Y states are given by $N_X(1 - f_Y)/\tau_{X \to Y}$. The time constants referring to the transition from a high energy state to a lower energy state are known as the relaxation time constants and are experimentally measured. They range from 0.1 – 10 ps. The time constants that refer to the opposite transitions are known as the capture rates and they are computed by the thermal equilibrium condition as $\tau_{X \to Y} = \tau_{Y \to X} \frac{N_c^X}{N_c^Y} e^{\Delta E_{X \to Y}/(K_B T)}$. In this relation, $\Delta E_{X \to Y}$ refers to the energy distance between the energy levels X and Y. The time constants τ_{spon}^X are the carrier lifetimes, accounting for the non-radiative recombination process. The last two terms at the right-hand side

(RHS) of the GS and ES carrier equations are describing the stimulated emission process. The parameter g_X^0 is the small signal gain, ϵ_X is the gain suppression factor [67] and S_X is the photon density at each state. The small signal gain is computed as:

$$g_X^0 = \frac{c}{n} \frac{\Gamma_X (2\pi q^2)}{cn\epsilon_0 m_0^2} \frac{P_{cv}^2 D_n^X N_D / H_{WL}}{\hbar \omega_X} \left[\frac{1}{2\pi} \frac{\Delta\omega_{homo}}{(0.5\Delta\omega_{homo})^2} \right] \qquad (4\text{-}4)$$

The quotient c/n is the group velocity where n is the refractive index and c is the speed of light. The term Γ_X is the optical confinement factor, ϵ_0 is the vacuum permittivity, m_0 is the exciton mass, P_{cv}^2 is the transition matrix element and ω_X is the angular frequency associated with the emitted photons. The term in the brackets refers to the peak of the Lorentzian since for simplicity it is assumed that the frequency of the cavity mode matches the central frequency of the Lorentzian. The FWHM of the Lorentzian, known also as the homogeneous broadening, is given in angular frequency units as $\Delta\omega_{homo}$.

The rate equations for the electric fields E_{GS}, E_{ES} are given by:

$$\frac{dE_{GS}}{dt} = \frac{1}{2}(1 + jLEF_{GS}) \left(\frac{g_{GS}^0 (2f_{GS} - 1)}{1 + \epsilon_{GS} s_{GS}} - \frac{1}{\tau_{ph}} \right) E_{GS} + j\Delta\omega_{GS} E_{GS} \qquad (4\text{-}5)$$
$$+ \frac{k_{inj}^{GS}}{\tau_{in}} E_{GS}^m + \sqrt{\frac{b_{sp} N_{GS}}{2dt}} \exp(j\Delta\omega_{GS} t)\, (\chi_1 + j\chi_2)$$

$$\frac{dE_{ES}}{dt} = \frac{1}{2}(1 + jLEF_{ES}) \left(\frac{g_{ES}^0 (2f_{ES} - 1)}{1 + \epsilon_{ES} s_{ES}} - \frac{1}{\tau_{ph}} \right) E_{ES} + j\Delta\omega_{ES} E_{ES} \qquad (4\text{-}6)$$
$$+ \frac{k_{inj}^{ES}}{\tau_{in}} E_{ES}^m + \sqrt{\frac{b_{sp} N_{ES}}{2dt}} \exp(j\Delta\omega_{ES} t)\, (\chi_3 + j\chi_4)$$

Each RHS contains four terms: (a) the first term accounts for the stimulated emission rate, (b-c) the second and third terms for the external optical injection and (d) the last term for the spontaneous emission process. The parameter LEF_X stands for the linewidth enhancement factor (LEF), b_{sp} is the noise coupling factor, χ_{1-4} are random numbers drawn by a normal distribution $\mathcal{N}(0,1)$ and dt is the simulation step. Regarding optical injection, $\Delta\omega_X$ is the angular frequency detuning between the ML and the SL, k_{inj}^X is the optical injection strength, $\tau_{in} = 2Ln/c$ is the round-trip time and E_X^m is the external field. The photon density is calculated as $S_X = |E_X|^2$. The injection strength k_{inj}^X can be derived by:

$$k_{inj}^X = \frac{r_{inj}^X}{\sqrt{r_1}} \sqrt{\frac{1 - r_1}{n}} \qquad (4\text{-}7)$$

In (4-7), r_{inj}^X is the injection ratio which expresses the ratio of the field from the ML that is injected in the SL and r_1 is the low reflectivity. The photon lifetime is computed as in (3-7). The parameters used for the simulations are shown in Table 1.

Table 1 : Model Parameters

Simulation Parameters		
Parameter	**Description**	**Value**
n_l	Number of QD layers	3
$\Gamma_{GS,ES}$	Confinement Factor	0.06
n	Refractive Index	3.5
T	Temperature	295 K
L	Device Length	500 µm
W	Device Width	6 µm
H_{WL}	Height of the WL	10 nm
N_D	Surface Density of QDs	$3 \times 10^{10}\ cm^{-2}$
r_1, r_2	High and Low Reflectivity	0.32, 0.32
a_{loss}	Propagation Losses	$200\ m^{-1}$
D_n^{GS}, D_n^{ES}	GS / ES degeneracy	1, 2
P_{cv}^2	Transition Matrix Element	$2.7 \times 10^{-49}\ eV \times kg$
L_{cn}^{GS}, L_{cn}^{ES}	GS / ES emission wavelength	1275 nm, 1185 nm
$\tau_{WL \rightarrow ES}$	Relaxation time from the WL to the ES	10 ps
$\tau_{ES \rightarrow GS}$	Relaxation time from the ES to the GS	7 ps
$\tau_{spon}^{WL}, \tau_{spon}^{ES}, \tau_{spon}^{GS}$	Carrier Lifetime	2 ns, 2 ns, 2 ns
$\epsilon_{GS}, \epsilon_{ES}$	Gain Suppression Factor	$2 \times 10^{-22}\ m^3, 2 \times 10^{-22}\ m^3$
b_{sp}	Noise Coupling Factor	10^{-4}
$\Delta E_{WL \rightarrow ES}$	Average Energy Distance Between WL and ES	85 meV
ΔE_{homo}	FWHM of the Lorentzian	10 meV

4.2 The Normalized Quantum Dot Laser Model

Although the set of equations (4-1) - (4-6) describes adequately the operation of a single mode QD laser under optical injection, they are too complicated to be used for bifurcation analysis. In order to simplify the dynamical analysis of the system, the set of equations is normalized with respect to the photon lifetime. The normalized carrier equations are:

$$\frac{df_{WL}}{d\tau} = \eta[K + r_{WL}^{ES}C_{ew}f_{ES}(1 - f_{WL}) - r_{WL}^{ES}B_{ew}f_{WL}(1 - f_{ES}) - f_{WL}] \tag{4-8}$$

$$\frac{df_{ES}}{d\tau} = \eta\left[B_{ew}f_{WL}(1 - f_{ES}) + C_e f_{GS}(1 - f_{ES}) - C_{ew}f_{ES}(1 - f_{WL})\right.$$
$$\left. - B_e f_{ES}(1 - f_{GS}) - f_{ES} - \frac{\hat{g}_{ES}(2f_{ES} - 1)}{1 + \hat{\epsilon}_{ES}\, s_{ES}}s_{ES}\right] \tag{4-9}$$

$$\frac{df_{GS}}{d\tau} = \eta\left[2B_e f_{ES}(1 - f_{GS}) - 2C_e f_{GS}(1 - f_{ES}) - f_{GS}\right.$$
$$\left. - \frac{\hat{g}_{GS}(2f_{GS} - 1)}{1 + \hat{\epsilon}_{GS}s_{GS}}s_{GS}\right] \tag{4-10}$$

In these equations, $\tau = t\,\tau_{ph}^{-1}$ is the normalized time. The evolution of the carrier dynamics is expressed here in terms of the occupation probabilities instead of the carrier densities. The coefficient $\eta = \tau_{ph}/\tau_{spon}^x$ is the ratio between the photon lifetime and the carrier lifetimes. Here η is identical for all the carrier equations since a common carrier lifetime 2 ns is used for all the states (see Table 1). The pumping rate is rewritten as $K = I\,\tau_{spon}^{WL}/(qV_{WL}N_c^{WL})$. The relaxation rates from the WL to the ES and from the ES to the GS are written as B_{ew} and B_e respectively, where $B_{ew} = \tau_{spon}^{ES}/\hat{\tau}_{WL\to ES}$ and $B_e = \tau_{spon}^{ES}/\tau_{ES\to GS}$. The capture rates from the ES to the WL and from the GS to the ES are written as $C_{ew} = \tau_{spon}^{ES}/\tau_{ES\to WL}$ and $C_e = \tau_{spon}^{ES}/\hat{\tau}_{GS\to ES}$ respectively. The transformed time constants are given by $\hat{\tau}_{WL\to ES} = \frac{N_c^{ES}}{N_c^{WL}}\tau_{WL\to ES} = r_{WL}^{ES}\tau_{WL\to ES}$ and $\hat{\tau}_{GS\to ES} = \frac{N_c^{ES}}{N_c^{GS}}\tau_{GS\to ES} = 2\tau_{GS\to ES}$. The normalized gain is $\hat{g}_x = \tau_{ph}g_x$ and the normalized gain compression factor is $\hat{\epsilon}_x = \epsilon_x\eta N_c^x$. The normalized field is written as $e_x = E_x/\sqrt{\eta N_c^x}$ and consequently the normalized photon density is $s_x = S_x/(\eta N_c^x)$. The normalized field equations for GS and ES emission are given by:

$$\frac{de_{GS}}{d\tau} = \frac{1}{2}(1 + jLEF_{GS})\left(\frac{\hat{g}_{GS}(2f_{GS} - 1)}{1 + \hat{\epsilon}_{GS}s_{GS}} - 1\right)e_{GS} + j\delta\omega_{GS}e_{GS}$$
$$+ \frac{k_{inj}^{GS}}{\hat{\tau}_{in}}e_{GS}^m + \sqrt{\frac{b_{sp}f_{GS}}{2d\tau}}\exp(j\delta\omega_{GS}\tau)(\chi_1 + j\chi_2) \tag{4-11}$$

$$\frac{de_{ES}}{d\tau} = \frac{1}{2}(1 + jLEF_{ES})\left(\frac{\hat{g}_{ES}(2f_{ES} - 1)}{1 + \hat{\epsilon}_{ES}s_{ES}} - 1\right)e_{ES} + j\delta\omega_{ES}e_{ES}$$
$$+ \frac{k_{inj}^{ES}}{\hat{\tau}_{in}}e_{ES}^m + \sqrt{\frac{b_{sp}f_{ES}}{2d\tau}}\exp(j\delta\omega_{ES}\tau)(\chi_3 + j\chi_4) \tag{4-12}$$

In these equations the round-trip time is normalized as $\hat{\tau}_{in} = \tau_{in}\tau_{ph}^{-1}$, whereas the frequency detuning is normalized as $\delta\omega_x = \Delta\omega_x\tau_{ph}$. The new simulation step $d\tau = \tau_{ph}^{-1}dt$ is used for the spontaneous emission rate. The set of equations (4-8)- (4-12) are in a form that is suitable for bifurcation analysis.

4.3   Solitary Laser Operation

First, the operation of the solitary QD laser is examined. For this reason, the injection ratio r_{inj}^x is set to 0 for both states. The laser output is computed for various current injection conditions in order to investigate the threshold current for GS and ES lasing. The normalized photon density versus current injection diagram (LI diagram) is shown in Figure 4-1.
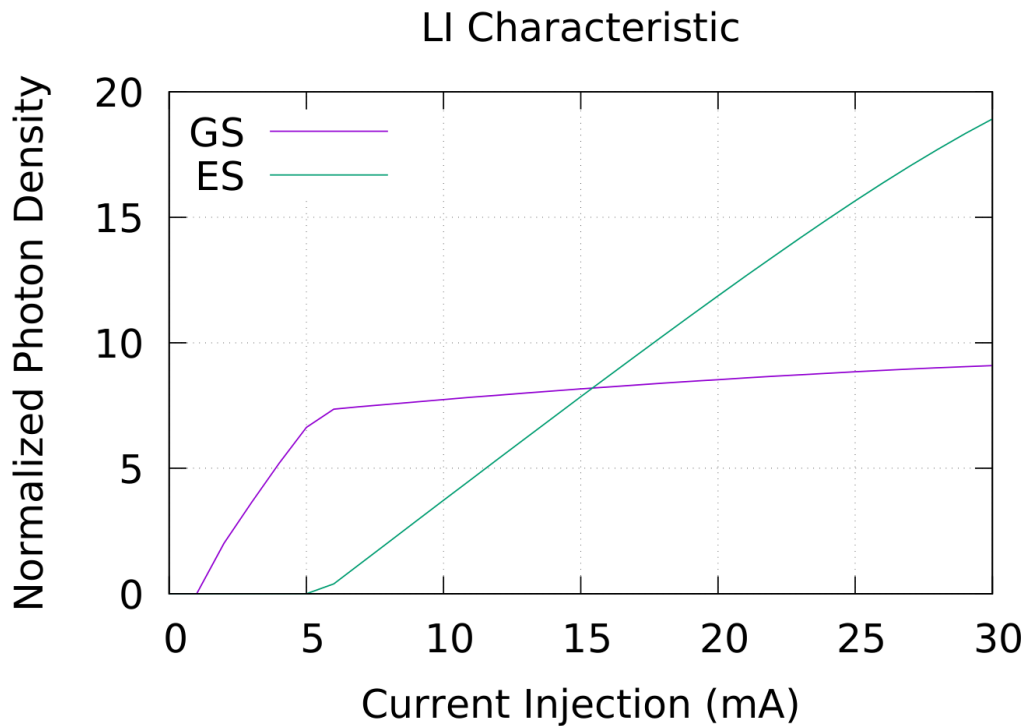
Figure 4-1 : Light - Current injection characteristic of the simulated device.

The GS threshold is detected at $I_{GS}^{thr} = 1$ mA, whereas the ES threshold is observed at $I_{ES}^{thr} = 5$ mA. The LI diagram is similar to the experimental results in Figure 3-12 except from the GS quenching effect which cannot be observed due to the excitonic approach [52] and the ignoring of the homogeneous broadening mechanism [60]. However, the dual-state dynamics are still well described by this simplified model [68].

The evolution of the photon density with the gain current is determined by the role of the different QD states. As the current injection is increased, the number of carries in the WL is increased. These carriers relax at the ES but due to the additional fast relaxation rate from the ES to the GS, the occupation probability at the ES when the steady state is reached is not high enough for ES lasing to occur. The increased accumulation of carriers at the GS results in the onset of GS lasing. At around 5 mA, the occupation probability at the GS is saturated due to the Pauli blocking effect ($f_{GS} \cong 1$). At this point, the transition rate from the ES to the GS is very low ($B_e(1 - f_{GS}) \cong 0$) and additional carriers from the WL due to increased carrier injection end up almost solely at the ES. The ES is able then to satisfy the lasing threshold condition and ES lasing occurs. Due to the very high number of vacant states available at the ES, the saturation of the ES

due to the Pauli blocking effect is theoretically observed for very high current injection [69].

Wetting Layer
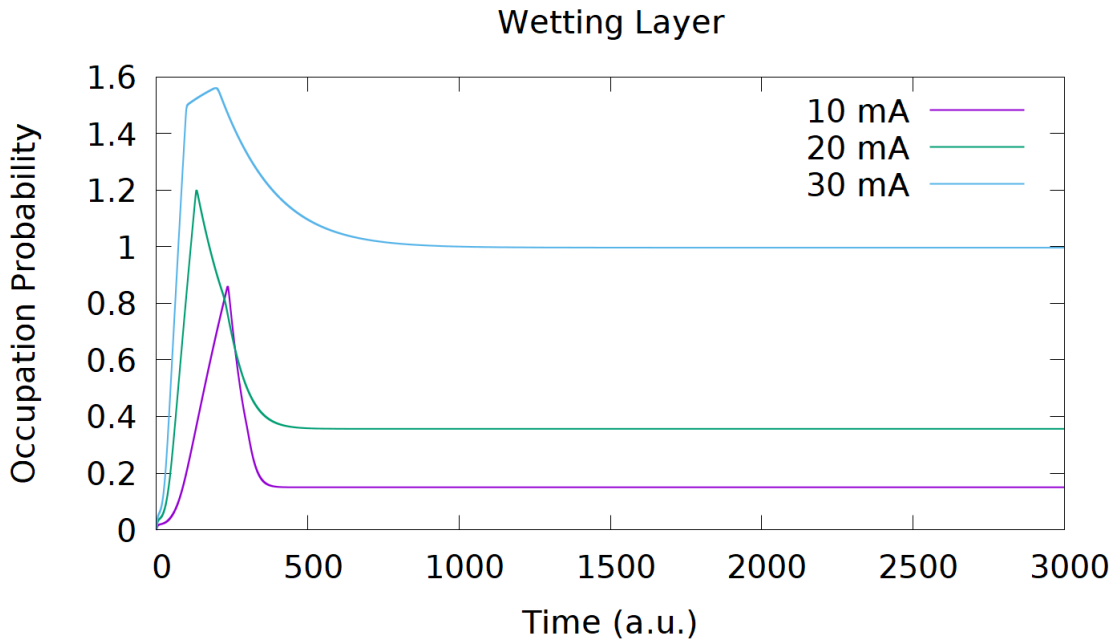
Figure 4-2 : The occupation probability of the WL versus the simulation time for three different bias conditions: 10, 20 and 30 mA.

The occupation probability at the WL for 10, 20 and 30 mA are shown in Figure 4-2. As the current injection is increased, the occupation probability at the WL is also increased. The turn-on dynamics are highly dumped which is an important characteristic of QD lasers compared to other semiconductor lasers. The reason for the highly dumped dynamics stems mainly from the high gain suppression factor which is caused by the 0-d structure of the QD energy band [70].

The occupation probabilities for the ES and the GS for the 10, 20 and 30 mA are shown in Figure 4-3 and Figure 4-4. Again, it can be seen that the turn-on dynamics are highly dumped. With respect to the steady state values, the occupation probability at the ES is increased from 0.7 to a value close to 1 for 10 mA and 30 mA respectively. It is seen that although the ES is beyond its threshold condition, its occupation probability is not clamped. This behavior can be explained by the large gain suppression factor, since the threshold condition is given by:

$$\frac{\hat{g}_{ES}(2f_{ES} - 1)}{1 + \hat{\epsilon}_{ES}s_{ES}} - 1 = 0$$

As a result, the increase of the photon density with current injection results in an increase of the steady state value of the occupation probability at the ES. With respect to the GS, it is well beyond its threshold value at the examined current injection values. The GS as in the case of the ES emission is not completely clamped but its occupation probability varies very weakly with increased current injection due to the Pauli blocking effect – the GS is saturated. The additional carriers that are injected at the WL end up almost exclusively at the ES level. These observations are in agreement with the plateau at the GS emission beyond the ES threshold (5 mA) in Figure 4-1.

A complete view of the occupation probabilities at the GS and the ES as a function of the current injection is given in Figure 4-5.
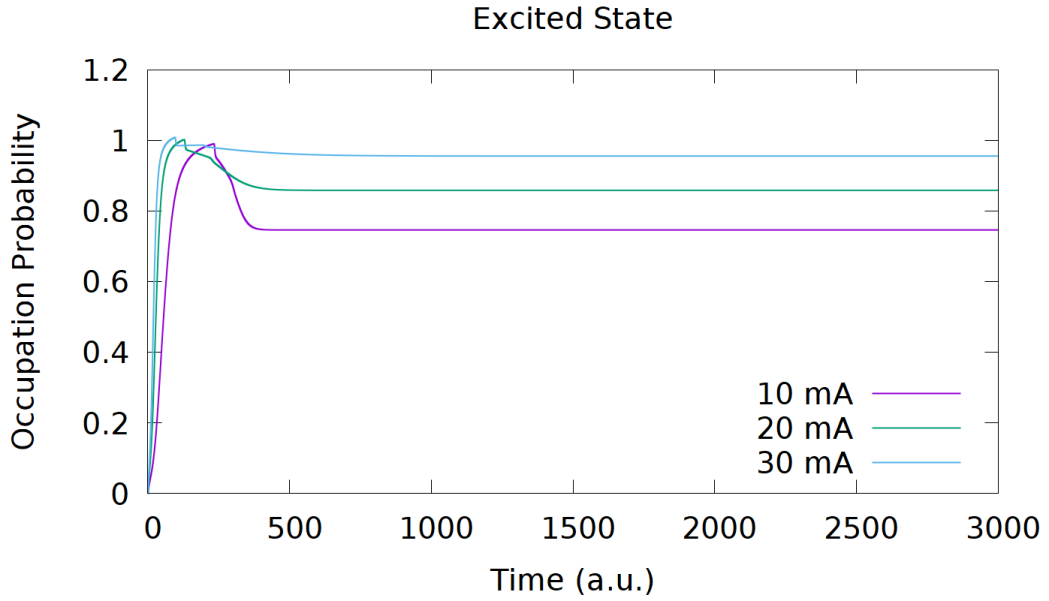
Figure 4-3: The occupation probability of the ES versus the simulation time for three different bias conditions: 10, 20 and 30 mA.
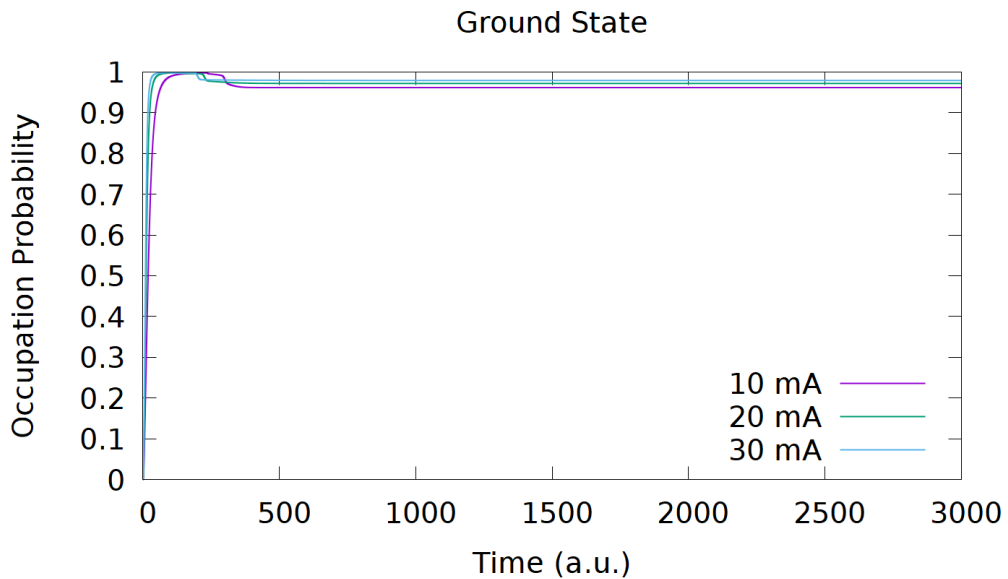
Figure 4-4: The occupation probability of the GS versus the simulation time for three different bias conditions: 10, 20 and 30 mA.

4.4 Dynamics of the optically injected Quantum Dot Laser

In order to examine the dynamics of the Quantum Dot Laser under external optical injection, the co-dimension 2 bifurcation diagrams are calculated by using the Matcont continuation software [71]. The scenarios depicted in **Error! Reference source not found.** will be considered so as to fully examine the multi-waveband capabilities of the QD laser. The ML is a QD Laser which is identical to the SL.

Table 2 : The various bias scenarios that are considered for the interaction between a master and

a slave laser

Case	Master Laser	Slave Laser

1	GS emission	GS emission
2	GS emission	ES emission
3	ES emission	GS emission
4	ES emission	ES emission
5	GS emission	Dual State emission
6	ES emission	Dual State emission
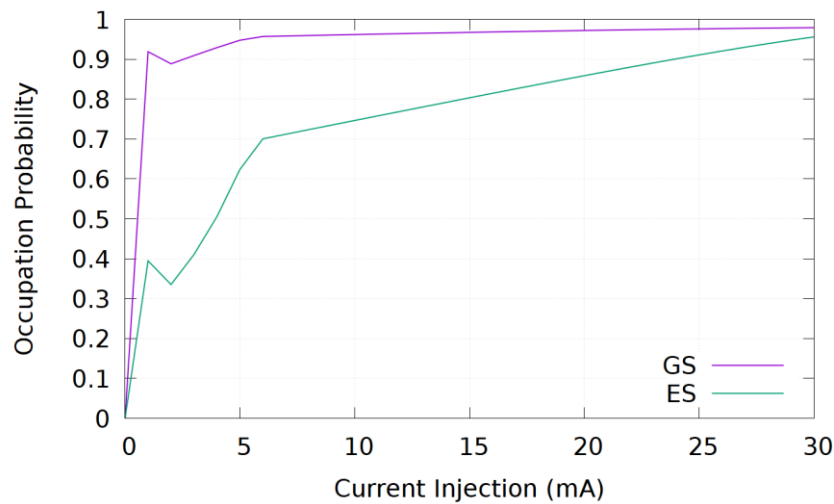
Figure 4-5 : The occupation probabilities at the GS and ES level as a function of the bias current.

Case 1: Slave Laser biased for GS emission under GS optical injection.

For all cases, the ML is biased at 25 mA where it emits both from the GS and the ES. In the first case, the injection ratio associated with ES emission is set to 0 ($r_{inj}^{ES} = 0$), whereas the injection ratio associated with the GS emission is treated as a control parameter. The SL is biased at 4 mA so as to emit only from the GS (see Figure 4-1). The dynamics of the SL are analyzed in terms of two parameters; (a) the injection ratio r_{inj}^{GS} , (b) the frequency detuning δf^{GS}.

Figure 4-6 shows the bifurcation curves for different detuning and injection ratio values. In this scheme, the solid black lines correspond to the SN bifurcation, whereas the dashed lines correspond to the Hopf bifurcation. Inside the grey region the SL is frequency locked to the ML and its output is a continuous wave (CW). Outside the grey region the SL is frequency unlocked and it may reveal complex dynamics ranging from simple periodic oscillations to chaotic dynamics [72]. According to Chapter 2 only the bifurcations that correspond to simple LCs are of interest when spiking dynamics are considered. The Zero Hopf points (ZH) and Cusp points (CP) are codim-2 bifurcations since they involve two parameters. In a ZH point a SN curve and a Hopf curve meet each other, whereas at a CP two SN curves meet. The CPs mark the limits of the SN curves. The ZH points are important regulating points separating the map in regions where the oscillatory dynamics stem from a Hopf bifurcation and regions where these dynamics originate from a SN bifurcation.
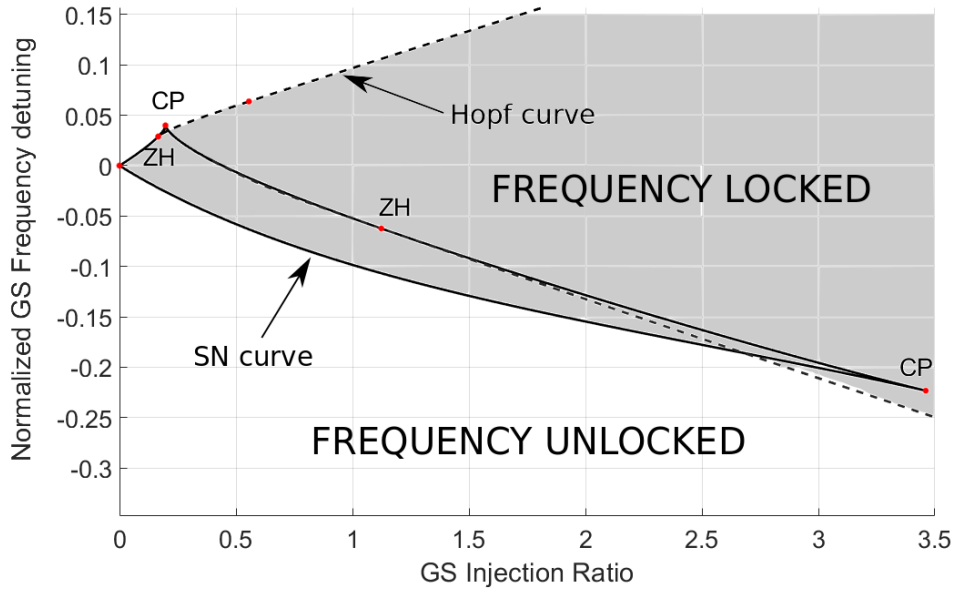
Figure 4-6 : The bifurcation diagram of the optically injected SL for GS optical injection and $I_{bias} = 4\ mA < I_{bias,th}^{ES}$ as a function of the normalized GS frequency detuning and the injection strength.

For fixed $\delta f_{GS} = -0.0047$(corresponds to -1 GHz), the single parameter (codim-1) diagram is shown in Figure 4-7. In this diagram, the amplitude of the GS field is illustrated as a function of the injection ratio. The dynamics of the system are described by following the black graph from the upper right point where the injection ratio is 1.2 up to the down left point where the injection ratio is 0.

For high enough injection ratio ($r_{inj}^{GS} = 1.2$), the system is stable. At this point, the SL is injection locked to the ML. As the injection ratio decreases, the field amplitude is also decreased up to a critical point where the injection ratio is 0.032. This point is marked as limit point (LP) which is also known as a SN bifurcation. At this point, a real negative eigenvalue becomes zero. By continuing upon the branch, the injection ratio is increased and this eigenvalue becomes negative. This means that at the LP a saddle point and a stable point (associated with injection locking) appear.

By following the branch of the saddle point as the injection ratio is increased, it can be seen that it passes through two neutral saddle point (NE) where two eigenvalues have the relation $|\lambda_i| = -|\lambda_j|$ so that their sum is zero. These points don't change the overall behavior of the system so they are of secondary importance and will be not commented for the rest of this study. At 0.4782 the saddle point passes through a Hopf bifurcation. Since the first Lyapunov coefficient is positive, this bifurcation is subcritical. At this point, two complex eigenvalues with negative real part pass to the right-hand plane and they become unstable. As the branch continuous, it meets one additional LP where an additional eigenvalue becomes positive. No other important turning points are met, as the branch ends at 0.

In general, we are interested only in stable points and stable limit cycles since only they describe the steady state behavior of the system. From injection ratio equal to 1.2 up to the LP it is known that the system has a stable node equilibrium. For $r_{inj}^{GS} = 0.02$ it can be seen in Figure 4-8 that the trajectory of the system follows a stable LC. In Figure 4-9, the period of the LC as a function of the injection ratio is shown. It is observed that as the injection ratio approaches the bifurcation point at 0.032 the period of the LC is dramatically increased. The increase in the period is linked to the bottleneck caused by

the SN bifurcation on the limit cycle – the ghost region. As a result, it can be deduced that the described bifurcation is a SNLC.
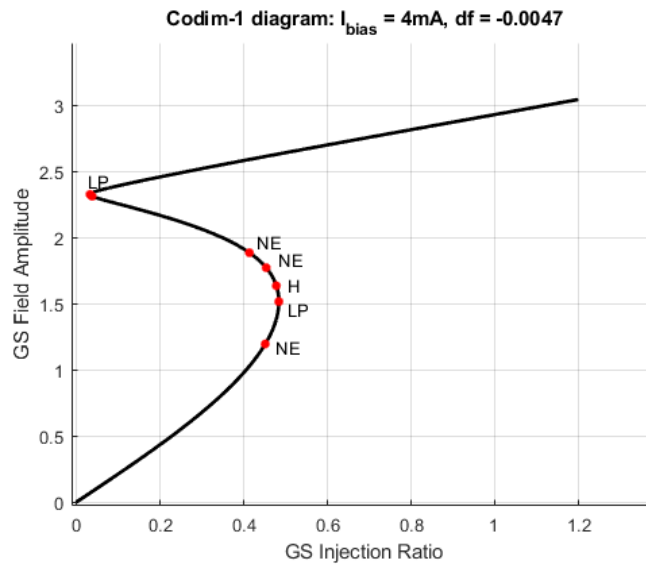
Figure 4-7: The bifurcation diagram depicting the GS field amplitude versus the injection ratio at the GS. The loss of stability takes place via a limit point (saddle node) bifurcation at 0.032.
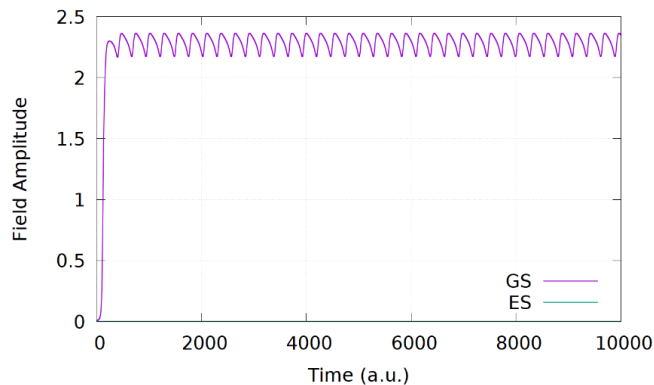
Figure 4-8: Stable Limit Cycle for $r_{inj}^{GS} = 0.02$, when SL is biased at 4 mA and the ML emits only from the GS.
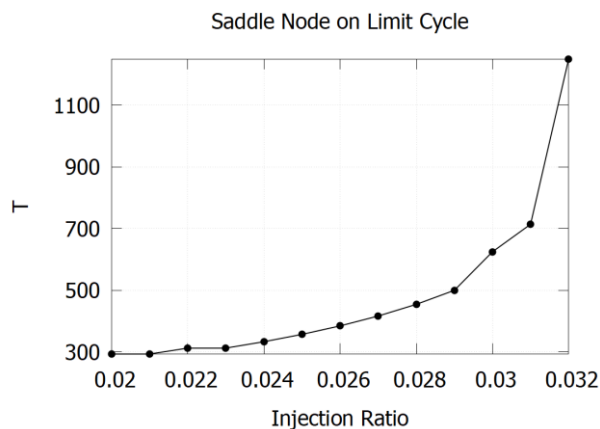
Figure 4-9: The period of the stable limit cycle versus the injection ratio. This relation shows that the system at 0.032 is close to a Saddle Node on Limit Cycle bifurcation.

For the fixed positive detuning $f_{GS} = 0.0047$(corresponds to +1 GHz), the single parameter bifurcation diagram is shown in Figure 4-10 . Again, it can be seen that the

stable equilibrium becomes unstable at 0.0315 via a SN bifurcation (same as LP), where one negative and real eigenvalue becomes positive. It is interesting to notice that there is a new bifurcation marked as BP (branch point) which occurs at the saddle point. The BP bifurcation is associated with the pitchfork bifurcation which is linked to the lasing threshold. From this point, an additional curve is created (the blue curve). By examining the equilibrium points on this curve, it can be seen that the points upon the blue curve have a non-zero value at the ES state emission. However, there are two positive real eigenvalues which means that these equilibrium points are unstable.
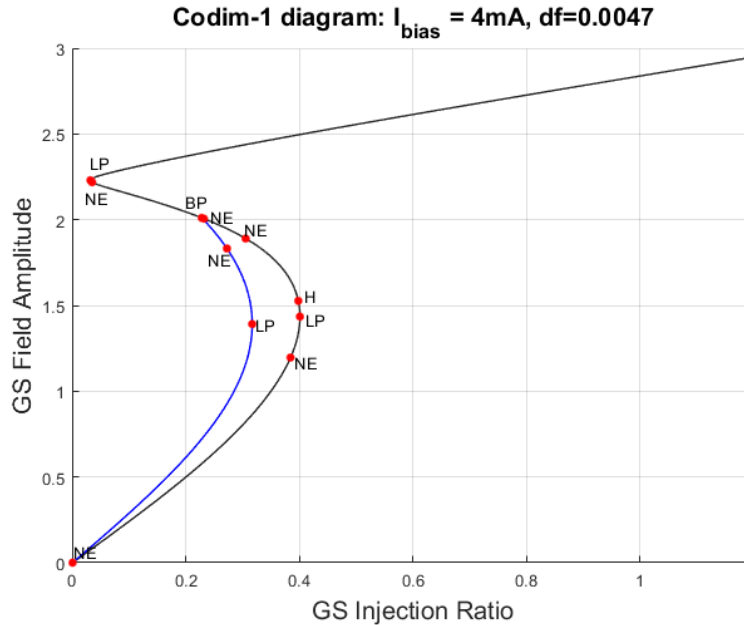
Figure 4-10: The codimension one bifurcation diagram, when the SL is biased at 4 mA and the detuning between the GS emission from the ML and the SL is equal to df = 0.0047, that corresponds to +1 GHz.

Below the critical point 0.0315, the system follows again a stable LC as in the case of δf = -0.0047. The LC is shown for $r_{inj}^{GS} = 0.028$ in Figure 4-11 . The relation between the period of the LC and the injection ratio is shown in Figure 4-12, which is similar to the case of SNLC presented for the case of negative detuning. No bi-stability is observed close to the bifurcation point so it can be deduced that the bifurcation is a SNLC.
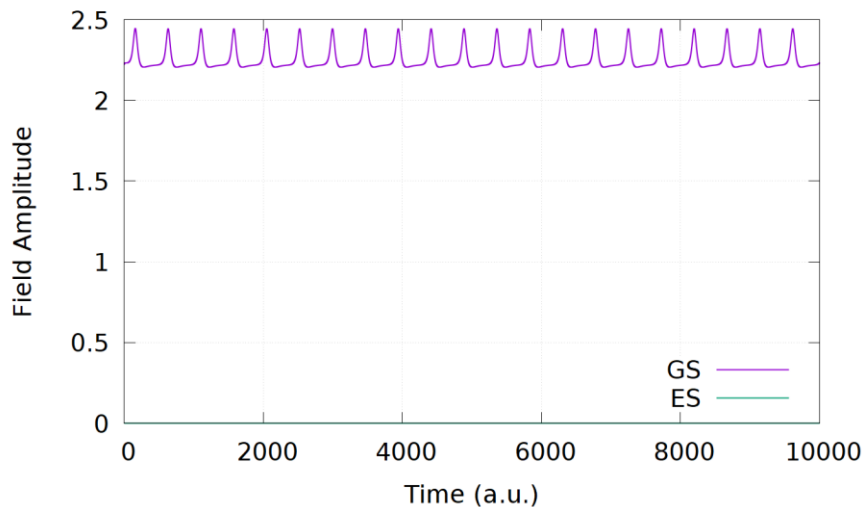
Figure 4-11: The LC that is presented at the output of GS when the detuning between the SL (biased at 4 mA) and the ML is equal to df = 0.0047 (+1 GHz) and the injection strength is set to $r_{inj}^{GS} = 0.028$.
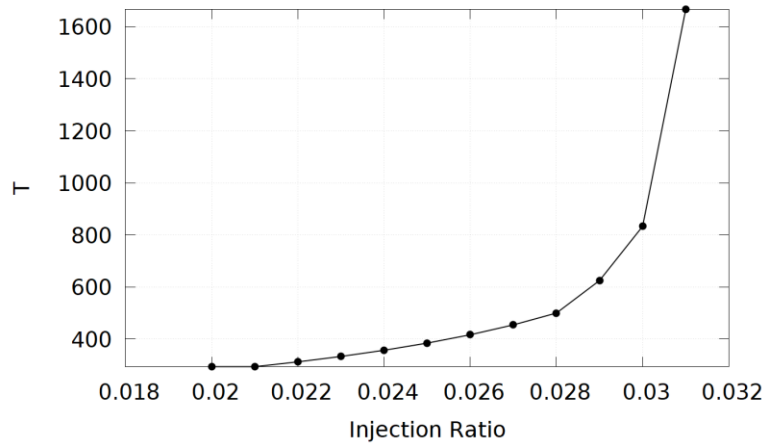
Figure 4-12 : The period of the LC as the injection ratio is increased, when the SL is biased at 4 mA and its detuning for the ML is equal to df = 0.0047 (+1 GHz).

The last bifurcation scenario that is linked to the transition from a stable point to a LC is observed for a detuning df that is higher than $df_{ZH} = 0.028$ (6 GHz). In this case according to Figure 4-6, this transition is via a Hopf Bifurcation. In Figure 4-13, it can be seen that when the injection ratio is higher than 0.19 then the system is stable with the stable state corresponding to CW GS emission. When the injection ratio is lower than 0.19 then the equilibrium becomes unstable through a Hopf bifurcation whose first Lyapunov coefficient is negative and consequently the bifurcation is supercritical. As it has been described in Chapter 2, such a bifurcation is linked to the transition of two complex eigenvalues (the one being the conjugate of the other) from the left plane corresponding to negative real parts to the right plane that corresponds to positive real parts. Therefore, the equilibrium is not a characterized by a stable node, but by a stable focus.
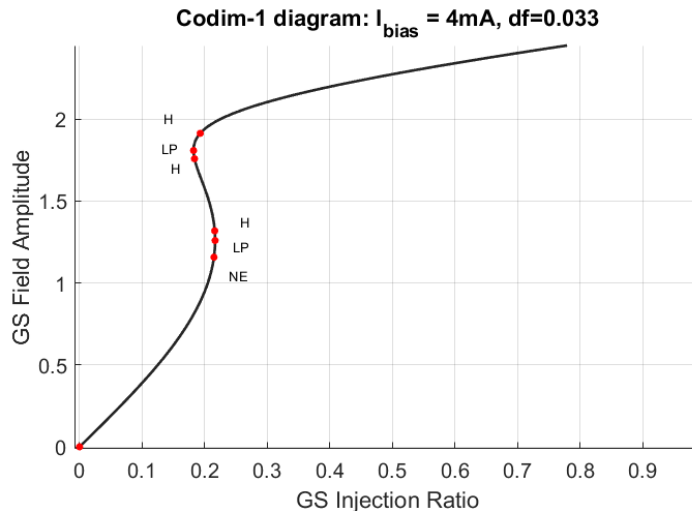
Figure 4-13: The codimension one bifurcation diagram, when the SL is biased at 4 mA and the detuning between the GS emission from the ML and the SL is equal to df = 0.033, that corresponds to +7 GHz.

In Figure 4-14 the relation between the period of the LC and the injection ratio is presented. Although again the period increases as the injection ratio converges to the bifurcation point (0.19), it does not increase as abruptly as in the case of SN bifurcation. Consequently, this graph cannot be linked to a ghost region close to a SN and therefore it is linked to a supercritical Hopf bifurcation.
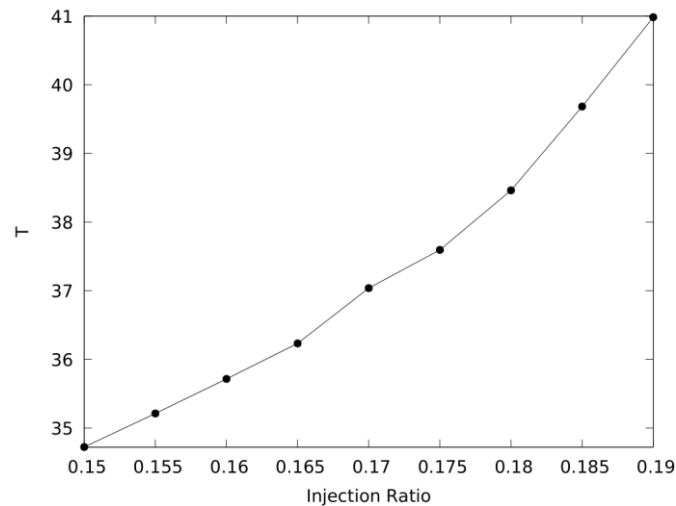
Figure 4-14: The period of the LC as the injection ratio is weakly increased, when the SL is biased at 4 mA and its detuning for the ML is equal to df = 0.033 (+7 GHz).

With respect to the negative detuning region, although a SN point is observed upon the Arnold Tongue, there are regions of detuning values where the LC associated with spiking dynamics does not cease to exist as a stable trajectory beyond the SN bifurcation point. In particular, a bistability is observed between the stable equilibrium and the spiking dynamics. This case is described in Figure 4-15. As the injection ratio is increased and the system enters the Arnold Tongue, a SN bifurcation takes place and a saddle and a node appear. However, the LC still exists and therefore the bifurcation is not a SNLC, meaning that the saddle and the node do not appear on the LC. The saddle acts as a barrier between the resting equilibrium and the spiking dynamics. Thus, bistability is observed depending on whether the initial conditions set the system at the region dictated by the node point or at the region dictated by the stable LC. As the injection is further increased a homoclinic bifurcation inside the Arnold Tongue leads to the disappearance of the LC. Beyond this point the only attractor is the equilibrium. These observations are in agreement with the bifurcation diagrams of conventional QW devices [73]. These regions are not suitable for neuromorphic encoding due to the bistability, which can abruptly change due to noise effects the dynamics from spiking to resting.

Case 2: Slave Laser biased for ES emission under GS optical injection.

In order to achieve solely ES emission, the slave laser whose LI relation is depicted in Figure 4-1 cannot be used since in this case ES lasing co-exists with GS lasing. For this reason, we reduce the cavity length from 500 μm to 350 μm. This choice reduces the photon lifetime as it is shown in (3-7). The GS due to a lower number of QD states cannot achieve a gain higher than the cavity losses, whereas ES since it has the double number of states is able to satisfy the lasing condition. Thus, only ES emission is possible. This relation is in accordance with experimental results in Figure 3-11. The LI characteristic for a cavity with length equal to 350 μm is shown in Figure 4-16.

The SL is biased at 4 mA and as in case 1 only injection from the GS is considered. As it is shown in Figure 4-17, external GS injection leads to only a single bifurcation scenario, namely a BP bifurcation. This is the point where the ES emission switches off due to increased GS injection strength. As the carriers in the GS level are radiatively recombined due to stimulated emission, the flow of carriers from the ES to the GS increases since GS has more unoccupied states. Thus, the carriers at the ES are reduced and along with it the gain at the ES. Thus, when the injection strength is strong

enough then the threshold condition for ES is not satisfied and ES switches off. The minimum GS injection strength required to turn off the ES emission is observed for low negative detuning values around $\delta f = -0.05$ (- 10 GHz).
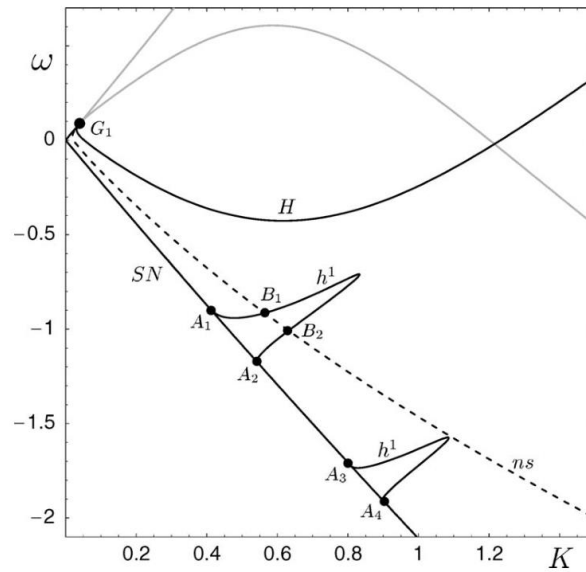
Figure 4-15: The bistability regions $A_1 - A_2$ and $A_3 - A_4$. Inside the curves h^1 the system is bi-stable between a resting point and spiking dynamics. On the curves h^1 a homoclinic bifurcation takes place between the saddle point and the stable LC, where the LC vanishes. The only resting state, outside the h^1 regions, is the stable equilibrium associated with the frequency locking condition [73].
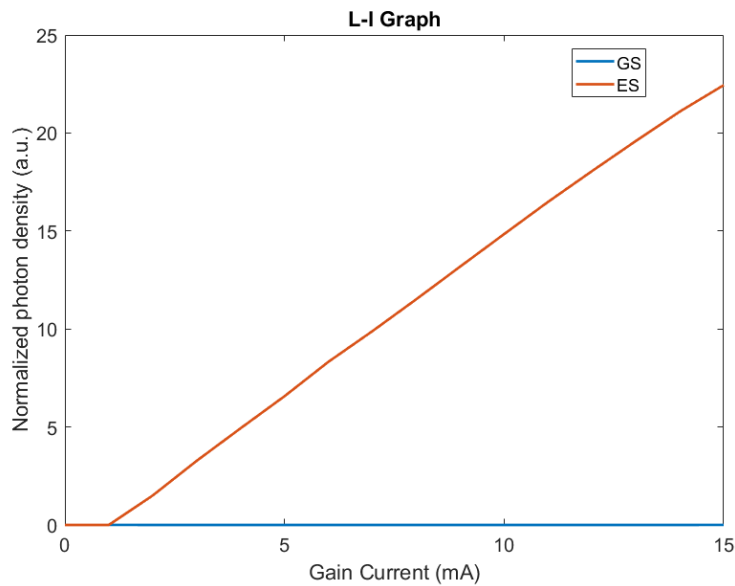
Figure 4-16: The L-I characteristic of a QD laser device with cavity length equal to 350 µm and the other parameters provided by Table 1.

At this stage it should be noted that experimental and numerical results exist stating that increasing the GS injection suppressed the GS emission and at a specific injection ratio result in an injection locked GS mode [74]. The system there is excitable and follows the SNLC scheme, since strong enough perturbations in the phase difference between the two lasers results in GS dropouts and ES spike events as it is shown in Figure 4-18. The reason behind the non-agreement between these two simulations can be found in the excitonic approach. Since electron and holes present different dynamics due to their different effective mass, the excitonic approach that is used in our case, which considers the same dynamics for both electron and holes, is too simplistic. A model

where the electrons and holes are described by different equations is out of the scope of this work.
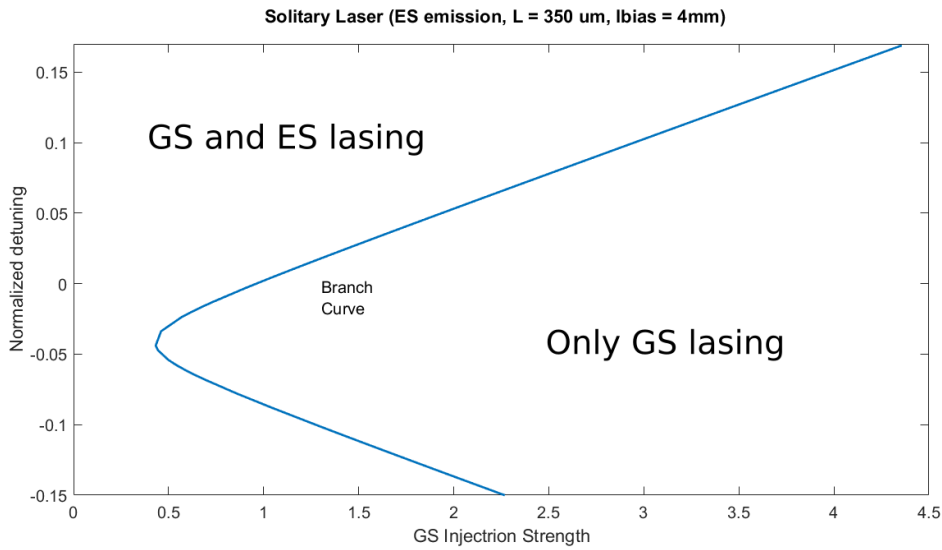
Figure 4-17: The codim-2 bifurcation diagram for the case where a SL that emits only from the ES is injected with emission from the GS.
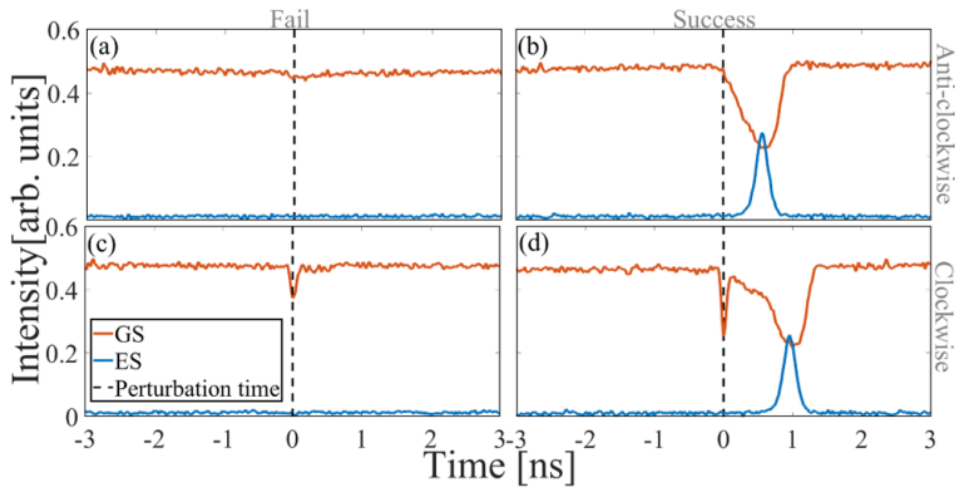
Figure 4-18: ES spikes induced due to GS dropouts in an experimental setup where, the solitary laser emits from the ES and it is biased close to a SN bifurcation caused by the GS injection from the ML. The attractor describes emission only from the GS due to injection locking condition Figure 4-18.

Case 3: Slave Laser biased for GS emission under ES optical injection.

In this case, a SL with cavity length equal to 500 μm is used again so as to be able to emit solely from the GS. With respect to the ML, the injection ratio r_{inj}^{GS} is set equal to zero, whereas the injection term r_{inj}^{ES} is used as a bifurcation parameter.

First the SL is biased at 4 mA, where it is close to the ES threshold (5 mA). In this case, the GS emission is almost saturated due to the Pauli blocking effect. The occupation probability of ES carriers is close to 0.5 namely close to the transparency condition. At this point ES injection can neither be absorbed nor amplified and as a result the injected ES emission simply passes attenuated through the cavity due to cavity losses. As a result, no bifurcation is observed.

When the SL is biased at 2 mA, the ES is far below the transparency and therefore the ES of the SL behaves as an absorber for incoming optical injection at the ES. Injected ES photons are absorbed and as a result the free carriers at the ES are increased. This outcome leads to an increased flow of carriers from the ES to the GS, where the GS has many vacant excitonic states and as a result the GS emission is enhanced. As before, in this case no bifurcation is observed.

When the SL is biased at 5 mA, the ES is above the transparency but still slightly below the lasing threshold. As a result, the laser has a positive ES gain and the optically injected ES radiation is increased since the ES level of the SL acts as an amplifier. This leads to a decrease of the flow from the ES to the GS level and consequently GS emission is decreased. In this case, we again observe no bifurcations.

Case 4: Slave Laser biased for ES emission under ES optical injection.

In this case the cavity length of the SL is again set equal to 350 μm so as to emit only from the ES. Again, only the injection ratio r_{inj}^{GS} is used as a bifurcation parameter. The SL is biased at 4 mA.

The co-dimension 2 bifurcation map that is derived in this case is analogous to the one observed in case 1 where the SL is biased at GS with under GS optical injection. This diagram is depicted in Figure 4-19. No GS emission is observed in this case. The spiking dynamics and the resting states are associated only with ES emission.

The case of a SNLC bifurcation when a negative detuning is introduced between the two lasers is presented in Figure 4-20.
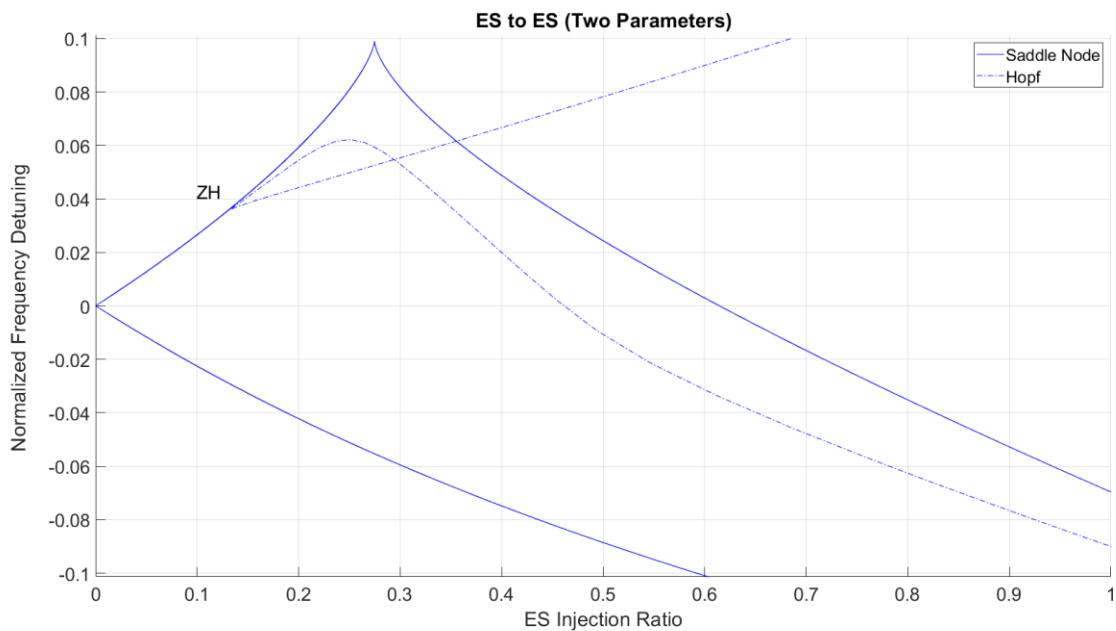
Figure 4-19: The two-parameter bifurcation diagram for the case when the solitary SL emits only from the ES and it receives ES optical injection.

Case 5: Slave Laser biased for dual-state emission under GS optical injection.

The cavity of the SL is again set equal to 500 μm and it is biased at 7 mA where according to its L-I relation, dual-state emission takes place. The ML is tuned so as to emit only from the GS and thus r_{inj}^{GS} is used as the bifurcation parameter. The two-parameter bifurcation diagram is similar to the one acquired in the previous cases. It

includes a BP bifurcation that is associated with the switch-off of ES emission due to increased GS injection. This is presented in Figure 4-21.

ES injection to ES emitting laser (L=350 um, Ibias= 4 mA)
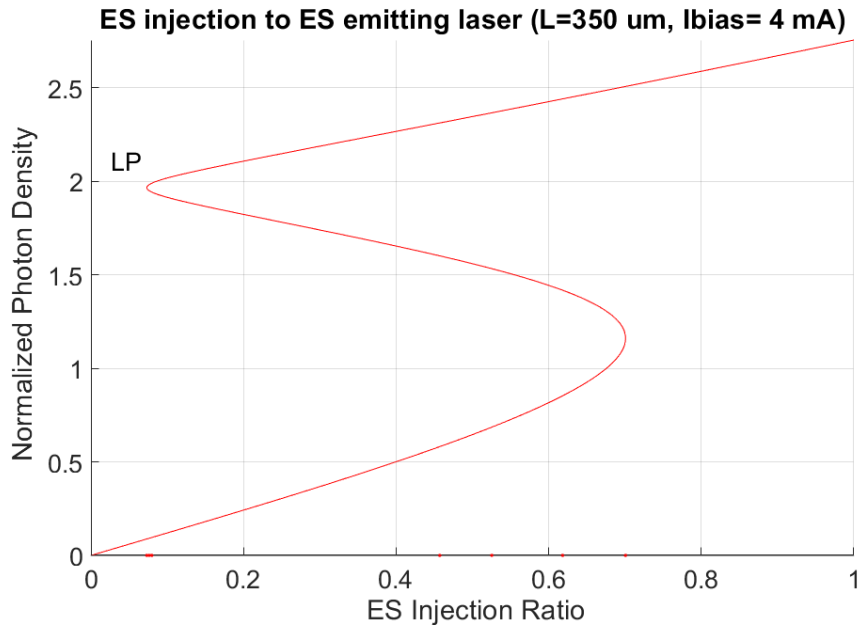
Figure 4-20: The LP close to $r_{inj}^{ES} = 0.09$ is associated with a SNIC bifurcation marking the transition for ES spiking dynamics to ES CW emission due to frequency locking.

Two-parameter bifurcation: GS to dual state
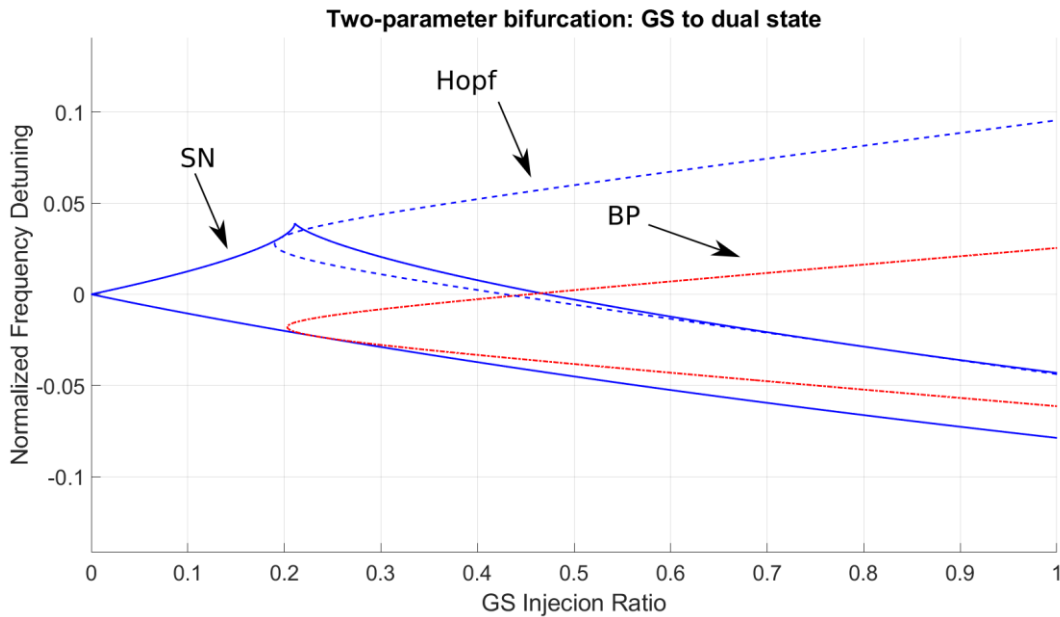
Figure 4-21: The two-parameter bifurcation diagram for the case when the SL emits from both GS and ES and is subject to GS optical injection.

First, we consider the case when $df = 0.033$ (+7 GHz). In this case the stable equilibrium is associated with CW lasing from both GS and ES when $r_{inj}^{GS} > 0.19$. For $r_{inj} < 0.19$ spiking dynamics from both GS and ES emission are observed. Once such example is depicted in Figure 4-22. The continuation process reveals that at injection ratio equal to 0.19, a supercritical Hopf bifurcation takes place.
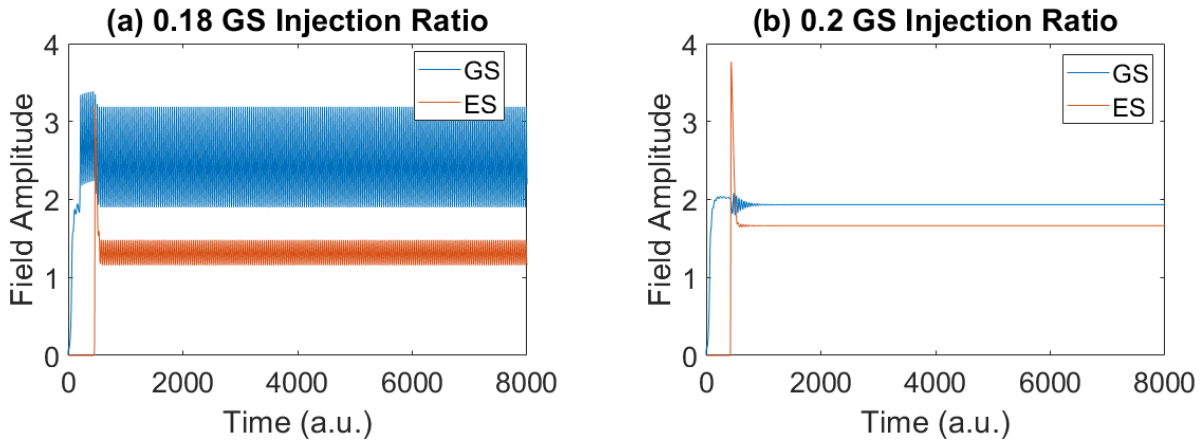
Figure 4-22 : The SL is biased at 7 mA to emit from both GS and ES and is subject to external GS injection. The detuning between the internal and external GS fields is equal to +7 GHz. In (a) The injection ratio is 0.18 and oscillatory dynamics are observed. In (b) the injection ratio is 0.2 and a resting state is observed. At 0.19 a supercritical Hopf bifurcation is observed.

Next, we consider the case when $df = 1$ GHz. In this case, instead of a Hopf bifurcation, the spiking dynamics are associated with a SNLC bifurcation that is spotted with respect to the bifurcation parameter at $r_{inj}^{GS} = 0.036$. This SNLC is shown in Figure 4-24. It is noted that dropouts from the ES are associated with increments of GS.

Figure 4-23: The SL is biased at 7 mA to emit from both GS and ES and is subject to external GS injection. The detuning between the internal and external GS fields is equal to +1 GHz. In (a) The injection ratio is 0.03 and oscillatory dynamics are observed. In (b) the injection ratio is 0.04 and a resting state is observed. At 0.036 a SNLC bifurcation is observed.

With respect to negative detuning between the internal and external injection, when $df = -1$ GHz, then at $r_{inj}^{GS} = 0.404$ a SNLC bifurcation is observed as it is depicted in Figure 4-24. Contrary to the case of $df = 1$ GHz, dropouts in GS cause spikes characterized by increased amplitude in the ES.

For $df = -5$ GHz it is noted that the system has a SNLC bifurcation close to $r_{inj}^{GS} = 0.238$. Interestingly, this point is close to a BP bifurcation where the ES switches off due to increased optical injection at the GS. The transition dynamics are depicted in Figure 4-25. These dynamics are similar to the experimental recordings presented in Figure 4-18 [74].

Case 6: Slave Laser biased for dual-state emission under ES optical injection.

The SL has a cavity length equal to 500 μm and it is biased at 7 mA so as to achieve dual-state emission.

The two-parameter bifurcation diagram is presented in Figure 4-26. This bifurcation diagram is similar to those presented in cases 1, 4, 5 (see **Error! Reference source not found.**). Contrary to the case 5, no BP curve is observed.

Figure 4-24: The SL is biased at 7 mA to emit from both GS and ES and is subject to external GS injection. The detuning between the internal and external GS fields is equal to -1 GHz. In (a) The injection ratio is 0.04 and oscillatory dynamics are observed. In (b) the injection ratio is 0.041 and a resting state is observed. At 0.0404 a SNLC bifurcation is computed.

Figure 4-25: The SL is biased at 7 mA to emit from both GS and ES and is subject to external GS injection. The detuning between the internal and external GS fields is equal to -5 GHz. In (a) The injection ratio is 0.237 and oscillatory dynamics are observed. In (b) the injection ratio is 0.24 and a resting state is observed. At 0.238 a SNLC bifurcation is computed.

When the detuning is $df = 7$ GHz, a supercritical Hopf bifurcation is observed at $r_{inj}^{ES} = 0.13$. This bifurcation is demonstrated in Figure 4-27. As opposed to the previous case where GS injection induced notable variations in the ES emission due to the anti-phase dynamics between GS and ES, here the impact of ES oscillatory dynamics at the GS emission is negligible.

When the detuning is $df = 1$ GHz, a SNLC bifurcation at $r_{inj}^{ES} = 0.0115$ is observed as it is depicted in Figure 4-28. Again, it can be seen that although the ES emission presents spiking dynamics for r_{inj}^{ES}, the GS is only weakly affected. Moreover, anti-phase

dynamics are shown since ES of increasing amplitude cause GS spikes of decreasing amplitude.
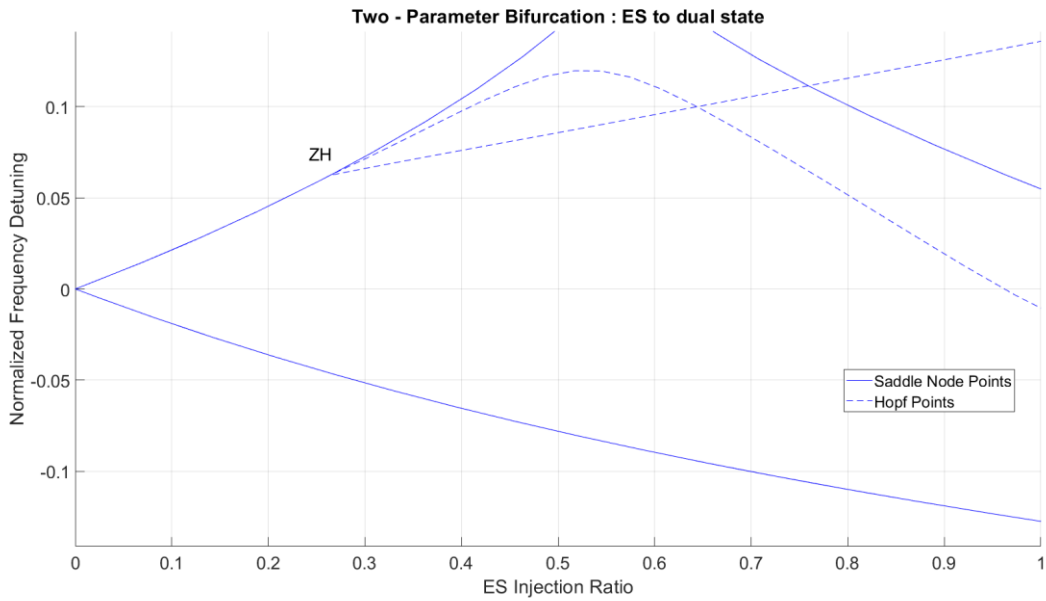
**Figure 4-26: The two-parameter bifurcation diagram for ES injection to a SL that emits from both GS and ES.**
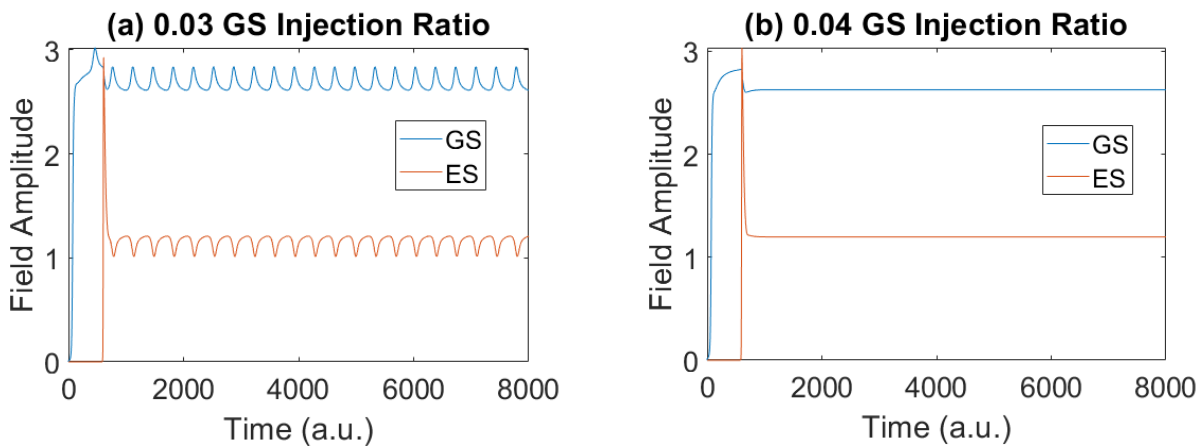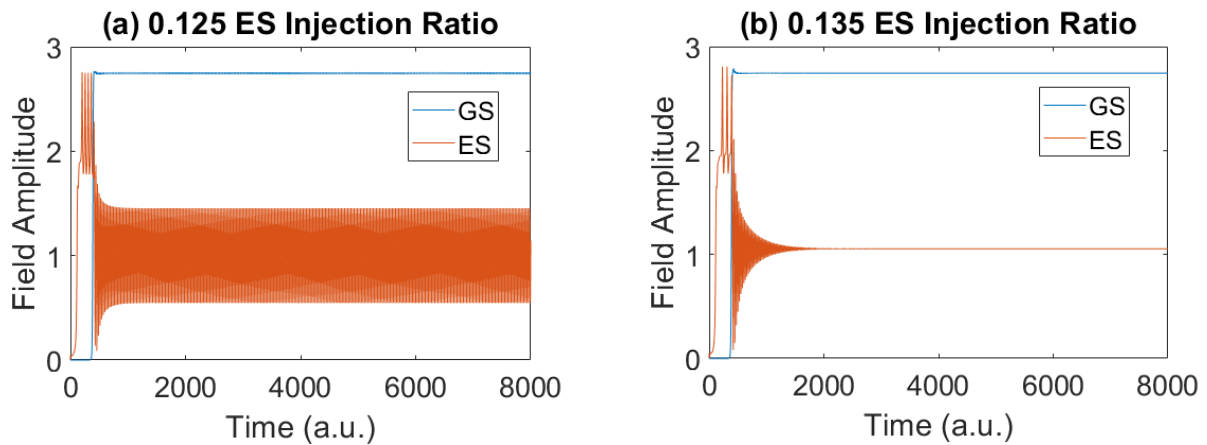

Figure 4-27: The SL is biased at 7 mA to emit from both GS and ES and is subject to external ES injection. The detuning between the internal and external ES fields is equal to 7 GHz. In (a) The injection ratio is 0.125 and oscillatory dynamics are observed. In (b) the injection ratio is 0.135 and a resting state is observed. At 0.13 a supercritical Hopf bifurcation is computed.

With respect to negative detuning values, the detuning is set at -1 GHz. The observed bifurcation is a SNLC at $r_{inj}^{ES} = 0.012$. This bifurcation scenario is presented in Figure 4-29.

For increased negative detuning at $df = $ - 4.25 GHz a SN bifurcation is observed for $r_{inj}^{ES} = 0.055$. In this region, a bistability is observed between spiking dynamics and stable dynamics. In this case the bifurcation is a saddle node off LC bifurcation [15], similar to the ones observed in the homoclinic regions defined in case 1 (see Figure 4-15). Multiple cases of negative detuning values have been studied ranging from $df = -0.06$ up to $df = -0.12$. These cases are all associated with a saddle node off LC, which renders them inefficient as bias points for neuromorphic processing due to the involved bistability.
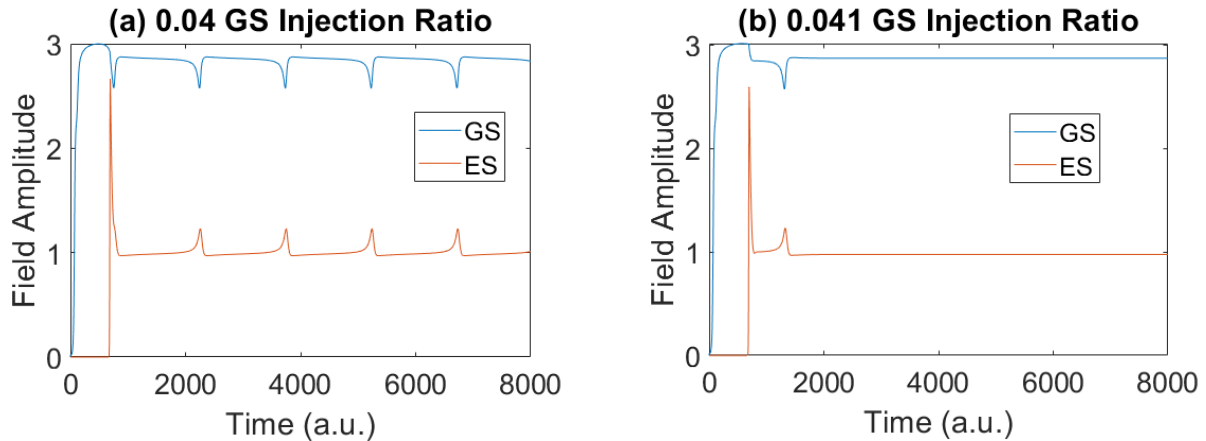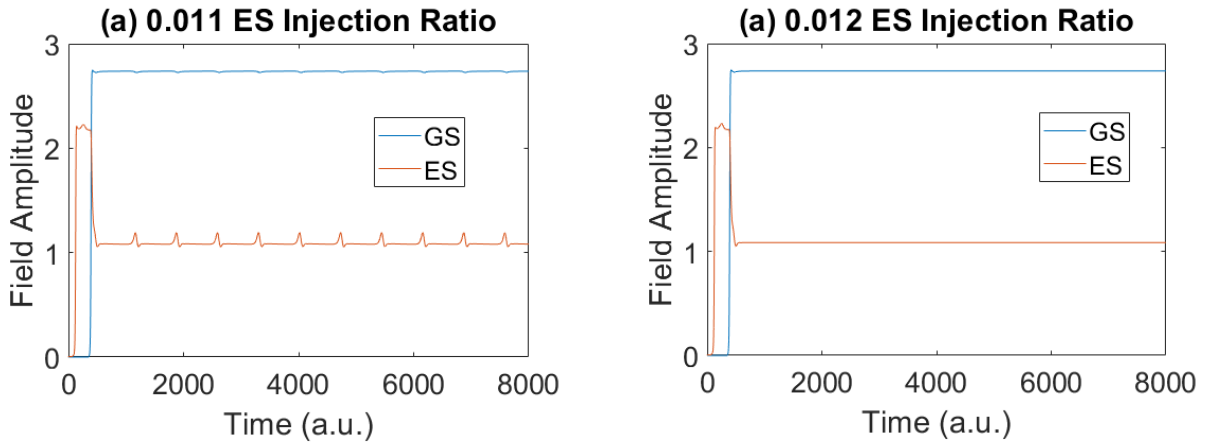
Figure 4-28: The SL is biased at 7 mA to emit from both GS and ES and is subject to external ES injection. The detuning between the internal and external ES fields is equal to 1 GHz. In (a) The injection ratio is 0.011 and oscillatory dynamics are observed. In (b) the injection ratio is 0.012 and a resting state is observed. At 0.0115 a SNLC bifurcation is computed.
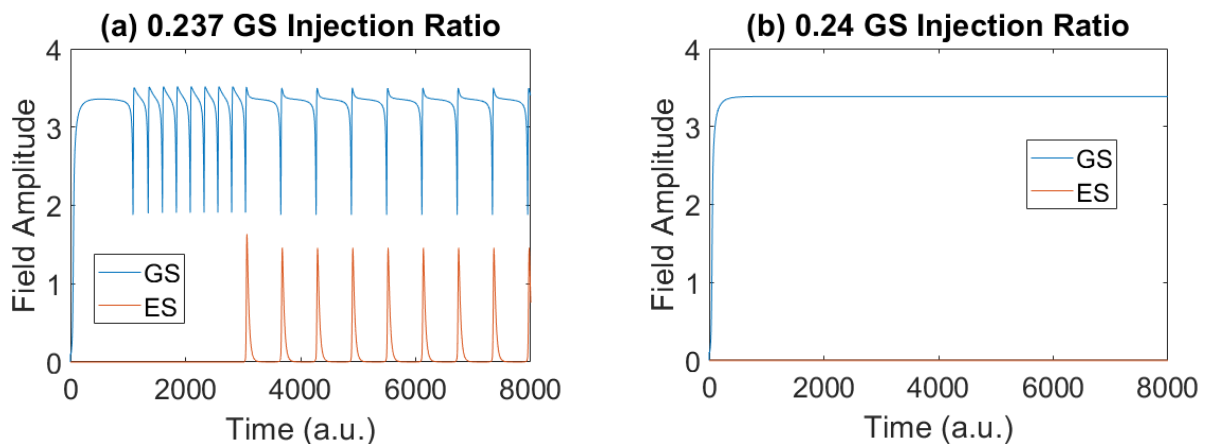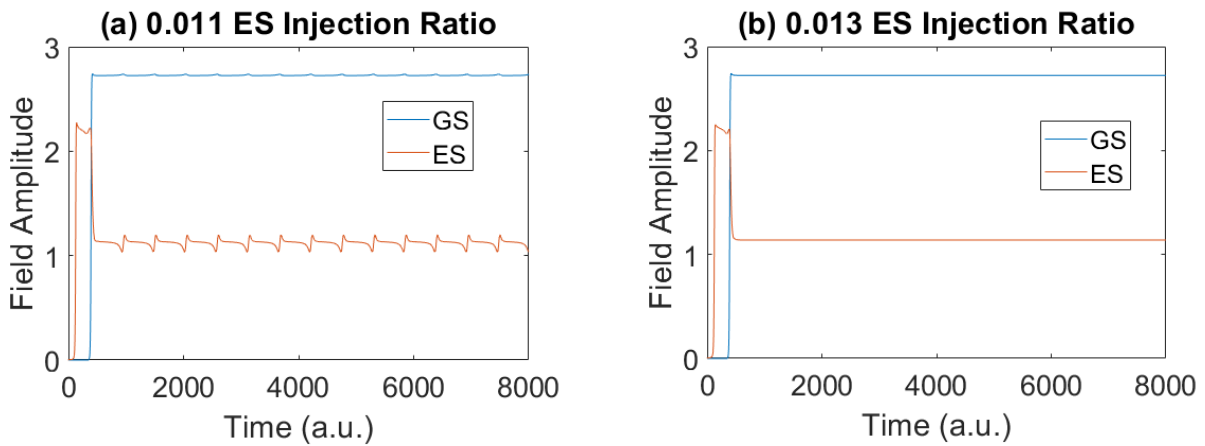

Figure 4-29: The SL is biased at 7 mA to emit from both GS and ES and is subject to external ES injection. The detuning between the internal and external ES fields is equal to -1 GHz. In (a) The injection ratio is 0.011 and oscillatory dynamics are observed. In (b) the injection ratio is 0.013 and a resting state is observed. At 0.012 a SNLC bifurcation is computed.

4.5   The Optically Injected QD Laser as an optical neuron

In the previous section, a detailed analysis has been performed for a QD laser under optical injection from an external source. It is obvious that the QD laser has the ability to generate optical spikes either from the GS or the ES emission and as a consequence it is a more flexible device compared to conventional QW neurons. We focused only in two types of bifurcations, namely the SNLC and the supercritical Hopf bifurcation since according to the theoretical description provided in Chapter 2, these are the two most important bifurcation scenarios in terms of excitability.

In terms of integrate and fire dynamics, the QD Laser can be biased so as to be frequently locked but close to a SNLC bifurcation. On the other hand, if the QD laser is biased close to a Hopf bifurcation then it can exhibit resonate and fire dynamics. It is interesting that both integrate and fire and resonate and fire operations have been demonstrated for both GS and ES spikes. If the SL is biased beyond the ES threshold lasing condition so as to perform dual-state emission (cases 5,6), then by using a suitable optical filter at the output of the laser, we can isolate GS or ES spikes to inject a post-synaptic neuron.

Additionally, as it is shown in cases 5,6, by inducing GS spiking through GS optical injection one can generate ES spiking and vice-versa. Thus, a nonlinear transformation is imposed at information encoded at one band by collecting photons generated at the other band. These results are important when the realization of all-optical neural motifs is targeted since according to experimental results [42] , ES emission can be linked to inhibitory dynamics and GS emission to excitatory dynamics.

5. CONCLUSIONS AND SUGGESTIONS FOR FUTURE RESEARCH

5.1 Conclusions

In this work, a detailed theoretical analysis of a Quantum Dot (QD) Laser under optical injection is presented for the first time from the scope of photonic neuromorphic processing. In particular, the theory of bifurcations is utilized as a mathematical tool to describe the dynamics of this device. The QD Laser is analyzed with regard to its dual-state dynamics. The dual-state dynamics are caused due to the 3D confinement of InAs dots that is achieved by the Stranski-Krastanov process, yielding atomic-like properties to the lasing device. The laser can emit from two different energy regions, one associated with ground state (GS) radiative transitions and the other associated with radiative transition from the first excited state (ES).

In order to analyze this device, a set of differential equations is used that describes the non-linear dynamics of the optically injected QD laser. The two parameters that are examined are the strength of the optical injection that is introduced to the QD laser by an external QD lasing source and the frequency detuning between the external and internal radiation. Six cases are examined. In the first case, the QD laser is biased so as to emit from the GS only and it is subject only to GS optical injection. In the second case, the QD laser is biased again so as to emit from the GS and it is subject to ES optical injection. In the third and fourth cases we use a smaller cavity so as to permit only ES emission from the solitary QD device and we examine the case of external GS injection and that of external ES injection. Last in the fifth and sixth cases, the solitary QD device is biased so as to emit from both GS and ES and we examine again the case when GS or ES external injection is introduces to the device.

For all these scenarios, bifurcation diagrams are created with emphasis given to these bifurcations that are related to the excitability which is the central property of neurons and it is the reason behind its spike dynamics. Spiking dynamics from both GS and ES are observed with anti-phase relation due to the internal scattering processes in the QD device. This device is shown to be versatile since by placing a suitable optical filter at its output we can isolate either GS or ES spike events that in turn can be introduced in other post-synaptic QD neurons.

The QD neuron can be as an integrate and fire neuron that encodes information at the firing rate of sike events. This functionality is connected to a bifurcation scheme known as saddle node on limit cycle (SNLC) that is presented also in biological neurons. This type of information encoding is presented both in spiking from the GS and the ES. Additionally, the QD neuron can be used also as a resonate and fire neuron that acts as a thresholder that generates spikes when a certain event is detected. This functionality is associated with a Hopf bifurcation that marks the transition from an equilibrium to spiking dynamics of a firing rate that is restricted to a certain frequency range. Again, this functionality is observed both from the GS and the ES.

Last, we detect a QD related property where variations to GS injection can induce ES spike events and vice-versa. This property is extremely important when neural motifs are to be implemented. It has been shown that if GS is associated with excitatory dynamics and ES with inhibitory dynamics then QD lasers can operate as either an all-optical excitatory neuron or as an inhibitory neuron [42]. Neural motifs are clusters of these types of neurons, able to co-operatively achieve advanced cognitive operations. Excitatory neurons produce spikes that enhance the spiking activity in post-synaptic

neurons, whereas inhibitory neurons produce spikes that inhibit the spiking activity in post-synaptic neurons. In mammalian brain a significant portion of neurons are inhibitory neurons and play an essential part in cognitive properties like imaging and sensory-motor reflexes [75].

5.2 Suggestions for further research

The theoretical analysis presented in this work has an important caveat. In some cases, it does not describe successfully experimentally recorded results as in the case when the solitary QD laser produces ES emission and it is optically injected with GS emission. Although experimental results demonstrated ES spiking along with GS dropouts [74], the presented model does not find any spiking dynamics. The reason behind this issue might be related with the excitonic approach. In our case we treat the electrons and the holes as a pair that is called an exciton and is described by a single rate-equation. In reality, due to different effective mass properties the holes and the electrons present different types of dynamics. Since this effect correctly describes the GS quenching effect where increased current injection results at the onset of ES emission and suppression of GS emission, a property that is not observed with our model, we deduce that perhaps the excitonic approach is behind the discrepancy between our analysis and experimental results. Since the examination of a more realistic model is more complex and it is out of the scope of this work, a similar analysis is important in terms of the bifurcation scenarios of a QD optically injected device, where electrons and holes are described by different rate - equations.

Additionally, it is observed that variations at the ES are only weakly affecting the GS emission, which is contrary to experimental results that demonstrate a QD neuron where ES acts as an inhibitory signal that suppressed GS emission. In this experiment however, the laser was a two-section device where a portion of the active material (75 %) has been biased so as to act as a gain and the other portion (15 %) as a saturable absorber. This device has different properties than the one analyzed in this work due to the different dynamics of the saturable absorber. Moreover, since its neural properties stem not only from the frequency detuning between the external injection and the internal field as in our case, but they are significantly affected by the dynamics of the saturable absorber, the bifurcation maps that will be created will be significantly different. Research on modelling of such two-section devices will shed light to their functionality as neuromorphic nodes, whereas the interaction between the dynamics of the saturable absorber and the ES might be able to induce a suppression at the GS dynamics.

Last, the QD neuron has been analyzed in isolation from other optical neurons. Future work can analyze clusters of QD neuron implementing more advanced neural motifs by harnessing the dual-waveband dynamics. In this case, the presented analysis will be of major importance as a guideline by determining the injection strength and frequency detuning needed to connect two QD neurons in a large neural population.

References

[1] S. H. Strogatz, "Exploring complex networks," *nature*, vol. 410, no. 6825, pp. 268–276, 2001.

[2] T. Vicsek, "Complexity: The bigger picture," *Nature*, vol. 418, no. 6894, pp. 131–131, 2002.

[3] A.-L. Barabási and R. Albert, "Emergence of scaling in random networks," *science*, vol. 286, no. 5439, pp. 509–512, 1999.

[4] P. Crescenzi, D. Goldman, C. Papadimitriou, A. Piccolboni, and M. Yannakakis, "On the complexity of protein folding," *J. Comput. Biol.*, vol. 5, no. 3, pp. 423–465, 1998.

[5] H. Markram *et al.*, "Introducing the human brain project," *Procedia Comput. Sci.*, vol. 7, pp. 39–42, 2011.

[6] R. C. Merkle, "Energy limits to the computational power of the human brain," 2007.

[7] J. Von Neumann, "First Draft of a Report on the EDVAC," *IEEE Ann. Hist. Comput.*, vol. 15, no. 4, pp. 27–75, 1993.

[8] J. Backus, "Can programming be liberated from the von Neumann style? A functional style and its algebra of programs," *Commun. ACM*, vol. 21, no. 8, pp. 613–641, 1978.

[9] G. E. Moore, M. D. Hill, N. P. Jouppi, and G. S. Sohi, "Readings in computer architecture," *San Franc. CA USA Morgan Kaufmann Publ. Inc*, pp. 56–59, 2000.

[10] J. Koomey, S. Berard, M. Sanchez, and H. Wong, "Implications of historical trends in the electrical efficiency of computing," *IEEE Ann. Hist. Comput.*, vol. 33, no. 3, pp. 46–54, 2010.

[11] J. Hasler and H. B. Marr, "Finding a roadmap to achieve large neuromorphic hardware systems," *Front. Neurosci.*, vol. 7, p. 118, 2013.

[12] P. R. Prucnal and B. J. Shastri, *Neuromorphic photonics*. CRC Press, 2017.

[13] B. Marr, B. Degnan, P. Hasler, and D. Anderson, "Scaling energy per operation via an asynchronous pipeline," *IEEE Trans. Very Large Scale Integr. VLSI Syst.*, vol. 21, no. 1, pp. 147–151, 2012.

[14] W.-C. Lee and C. Hu, "Modeling CMOS tunneling currents through ultrathin gate oxide due to conduction-and valence-band electron and hole tunneling," *IEEE Trans. Electron Devices*, vol. 48, no. 7, pp. 1366–1373, 2001.

[15] E. M. Izhikevich, *Dynamical systems in neuroscience*. MIT press, 2007.

[16] M. Anthony, *Discrete mathematics of neural networks: selected topics*. SIAM, 2001.

[17] W. Maass, "Networks of spiking neurons: the third generation of neural network models," *Neural Netw.*, vol. 10, no. 9, pp. 1659–1671, 1997.

[18] S. Thorpe, A. Delorme, and R. Van Rullen, "Spike-based strategies for rapid processing," *Neural Netw.*, vol. 14, no. 6–7, pp. 715–725, 2001.

[19] A. L. Hodgkin, "The local electric changes associated with repetitive action in a non-medullated axon," *J. Physiol.*, vol. 107, no. 2, p. 165, 1948.

[20] P. A. Merolla *et al.*, "A million spiking-neuron integrated circuit with a scalable communication network and interface," *Science*, vol. 345, no. 6197, pp. 668–673, 2014.

[21] B. V. Benjamin *et al.*, "Neurogrid: A mixed-analog-digital multichip system for large-scale neural simulations," *Proc. IEEE*, vol. 102, no. 5, pp. 699–716, 2014.

[22] J. Schemmel, D. Briiderle, A. Griibl, M. Hock, K. Meier, and S. Millner, "A wafer-scale neuromorphic hardware system for large-scale neural modeling," in *Proceedings of 2010 IEEE International Symposium on Circuits and Systems*, 2010, pp. 1947–1950.

[23] S. B. Furber, F. Galluppi, S. Temple, and L. A. Plana, "The spinnaker project," *Proc. IEEE*, vol. 102, no. 5, pp. 652–665, 2014.

[24] H. Markram, "The human brain project," *Sci. Am.*, vol. 306, no. 6, pp. 50–55, 2012.

[25] E. Magesan, J. M. Gambetta, A. D. Córcoles, and J. M. Chow, "Machine learning for discriminating quantum measurement trajectories and improving readout," *Phys. Rev. Lett.*, vol. 114, no. 20, p. 200501, 2015.

[26] A. Radovic *et al.*, "Machine learning at the energy and intensity frontiers of particle physics," *Nature*, vol. 560, no. 7716, pp. 41–48, 2018.

[27] J. Duarte *et al.*, "Fast inference of deep neural networks in FPGAs for particle physics," *J. Instrum.*, vol. 13, no. 07, p. P07027, 2018.

[28] J. Kates-Harbeck, A. Svyatkovskiy, and W. Tang, "Predicting disruptive instabilities in controlled fusion plasmas through deep learning," *Nature*, vol. 568, no. 7753, pp. 526–531, 2019.

[29] T. F. De Lima *et al.*, "Machine learning with neuromorphic photonics," *J. Light. Technol.*, vol. 37, no. 5, pp. 1515–1534, 2019.

[30] J. Han, A. Jentzen, and E. Weinan, "Solving high-dimensional partial differential equations using deep learning," *Proc. Natl. Acad. Sci.*, vol. 115, no. 34, pp. 8505–8510, 2018.

[31] Y. Shen *et al.*, "Deep learning with coherent nanophotonic circuits," *Nat. Photonics*, vol. 11, no. 7, p. 441, 2017.

[32] N. P. Jouppi *et al.*, "In-datacenter performance analysis of a tensor processing unit," in *Proceedings of the 44th Annual International Symposium on Computer Architecture*, 2017, pp. 1–12.

[33] T. W. Hughes, M. Minkov, Y. Shi, and S. Fan, "Training of photonic neural networks through in situ backpropagation and gradient measurement," *Optica*, vol. 5, no. 7, pp. 864–871, 2018.

[34] A. N. Tait *et al.*, "Demonstration of multivariate photonics: blind dimensionality reduction with integrated photonics," *J. Light. Technol.*, vol. 37, no. 24, pp. 5996–6006, 2019.

[35] S. Zhang *et al.*, "Field and lab experimental demonstration of nonlinear impairment compensation using neural networks," *Nat. Commun.*, vol. 10, no. 1, pp. 1–8, 2019.

[36] J. Feldmann, N. Youngblood, C. D. Wright, H. Bhaskaran, and W. H. P. Pernice, "All-optical spiking neurosynaptic networks with self-learning capabilities," *Nature*, vol. 569, no. 7755, Art. no. 7755, May 2019, doi: 10.1038/s41586-019-1157-8.

[37] Q. Wang *et al.*, "Optically reconfigurable metasurfaces and photonic devices based on phase change materials," *Nat. Photonics*, vol. 10, no. 1, pp. 60–65, 2016.

[38] W. W. Chow and F. Jahnke, "On the physics of semiconductor quantum dots for applications in lasers and quantum optics," *Prog. Quantum Electron.*, vol. 37, no. 3, pp. 109–184, 2013.

[39] S. S. Mikhrin *et al.*, "High power temperature-insensitive 1.3 µm InAs/InGaAs/GaAs quantum dot lasers," *Semicond. Sci. Technol.*, vol. 20, no. 5, p. 340, 2005.

[40] J. K. Mee *et al.*, "A passively mode-locked quantum-dot laser operating over a broad temperature range," *Appl. Phys. Lett.*, vol. 101, no. 7, p. 071112, 2012.

[41] S. Chen *et al.*, "Electrically pumped continuous-wave III–V quantum dot lasers on silicon," *Nat. Photonics*, vol. 10, no. 5, p. 307, 2016.

[42] C. Mesaritakis, A. Kapsalis, A. Bogris, and D. Syvridis, "Artificial Neuron Based on Integrated Semiconductor Quantum Dot Mode-Locked Lasers," *Sci. Rep.*, vol. 6, no. 1, Art. no. 1, Dec. 2016, doi: 10.1038/srep39317.

[43] G. Sarantoglou, M. Skontranis, A. Bogris, and C. Mesaritakis, "Temporal Resolution Enhancement in Quantum-Dot Laser Neurons due to Ground State Quenching Effects," in *Optical Fiber Communication Conference*, 2020, pp. M2K-1.

[44] S. Grill, V. S. Zykov, and S. C. Müller, "Spiral wave dynamics under pulsatory modulation of excitability," *J. Phys. Chem.*, vol. 100, no. 49, pp. 19082–19088, 1996.

[45] G. Indiveri, E. Chicca, and R. Douglas, "A VLSI array of low-power spiking neurons and bistable synapses with spike-timing dependent plasticity," *IEEE Trans. Neural Netw.*, vol. 17, no. 1, pp. 211–221, Jan. 2006, doi: 10.1109/TNN.2005.860850.

[46] M. A. Nahmias, B. J. Shastri, A. N. Tait, and P. R. Prucnal, "A Leaky Integrate-and-Fire Laser Neuron for Ultrafast Cognitive Computing," *IEEE J. Sel. Top. Quantum Electron.*, vol. 19, no. 5, pp. 1–12, Sep. 2013, doi: 10.1109/JSTQE.2013.2257700.

[47] H. K. Khalil and J. W. Grizzle, *Nonlinear systems*, vol. 3. Prentice hall Upper Saddle River, NJ, 2002.

[48] S. H. Strogatz, *Nonlinear dynamics and chaos with student solutions manual: With applications to physics, biology, chemistry, and engineering*. CRC press, 2018.

[49] E. M. Izhikevich, "Resonate-and-fire neurons," *Neural Netw.*, vol. 14, no. 6–7, pp. 883–894, 2001.

[50] D. G. Deppe, K. Shavritranuruk, G. Ozgur, H. Chen, and S. Freisem, "Quantum dot laser diode with low threshold and low internal loss," *Electron. Lett.*, vol. 45, no. 1, pp. 54–56, 2009.

[51] A. Röhm, *Dynamic scenarios in two-state quantum dot lasers: Excited state lasing, ground state quenching, and dual-mode operation.* Springer, 2015.

[52] M. Gioannini, "Ground-state power quenching in two-state lasing quantum dot lasers," *J. Appl. Phys.*, vol. 111, no. 4, p. 043108, 2012.

[53] J. Wilson and J. F. Hawkes, "Optoelectronics-an introduction," *Optoelectron.- Introd. 2nd Ed.*, 1989.

[54] P. W. Milonni and J. H. Eberly, *Laser Physics.* John Wiley & Sons, 2010.

[55] B. Lingnau, *Nonlinear and nonequilibrium dynamics of quantum-dot optoelectronic devices.* Springer, 2015.

[56] D. Bimberg, M. Grundmann, and N. N. Ledentsov, *Quantum dot heterostructures.* John Wiley & Sons, 1999.

[57] V. M. Ustinov, A. E. Zhukov, A. E. Zhokov, N. A. Maleev, and A. Y. Egorov, *Quantum dot lasers*, vol. 11. Oxford University Press on Demand, 2003.

[58] L. Goldstein, F. Glas, J. Y. Marzin, M. N. Charasse, and G. Le Roux, "Growth by molecular beam epitaxy and characterization of InAs/GaAs strained-layer superlattices," *Appl. Phys. Lett.*, vol. 47, no. 10, pp. 1099–1101, 1985.

[59] K. Akahane, N. Ohtani, Y. Okada, and M. Kawabe, "Fabrication of ultra-high density InAs-stacked quantum dots by strain-controlled growth on InP (3 1 1) B substrate," *J. Cryst. Growth*, vol. 245, no. 1–2, pp. 31–36, 2002.

[60] M. Sugawara *et al.*, "Modeling room-temperature lasing spectra of 1.3-µm self-assembled InAs/GaAs quantum-dot lasers: Homogeneous broadening of optical gain under current injection," *J. Appl. Phys.*, vol. 97, no. 4, p. 043523, 2005.

[61] A. Roehm, B. Lingnau, and K. Luedge, "Understanding ground-state quenching in quantum-dot lasers," *IEEE J. Quantum Electron.*, vol. 51, no. 1, pp. 1–11, 2014.

[62] A. Markus, J. X. Chen, C. Paranthoen, A. Fiore, C. Platz, and O. Gauthier-Lafaye, "Simultaneous two-state lasing in quantum-dot lasers," *Appl. Phys. Lett.*, vol. 82, no. 12, pp. 1818–1820, 2003.

[63] A. Markus, J. X. Chen, O. Gauthier-Lafaye, J.-G. Provost, C. Paranthoën, and A. Fiore, "Impact of intraband relaxation on the performance of a quantum-dot laser," *IEEE J. Sel. Top. Quantum Electron.*, vol. 9, no. 5, pp. 1308–1314, 2003.

[64] *Ultrafast Lasers Based on Quantum Dot Structures: Physics and Devices*, 1 edition. Weinheim, Germany: Wiley-VCH, 2011.

[65] D. Goulding *et al.*, "Excitability in a quantum dot semiconductor laser with optical injection," *Phys. Rev. Lett.*, vol. 98, no. 15, p. 153903, 2007.

[66] J. L. Dubbeldam and B. Krauskopf, "Self-pulsations of lasers with saturable absorber: dynamics and bifurcations," *Opt. Commun.*, vol. 159, no. 4–6, pp. 325–338, 1999.

[67] Y. Zhou, J. Duan, F. Grillot, and C. Wang, "Optical noise of dual-state lasing quantum dot lasers," *IEEE J. Quantum Electron.*, vol. 56, no. 6, pp. 1–7, 2020.

[68] E. A. Viktorov *et al.*, "Dynamics of a two-state quantum dot laser with saturable absorber," *Appl. Phys. Lett.*, vol. 90, no. 12, p. 121113, 2007.

[69] Z. Y. Zhang, Q. Jiang, and R. A. Hogg, "Simultaneous three-state lasing in quantum dot laser at room temperature," *Electron. Lett.*, vol. 46, no. 16, pp. 1155–1157, 2010.

[70] M. Gioannini, P. Bardella, and I. Montrosset, "Time-domain traveling-wave analysis of the multimode dynamics of quantum dot Fabry–Perot lasers," *IEEE J. Sel. Top. Quantum Electron.*, vol. 21, no. 6, pp. 698–708, 2015.

[71] A. Dhooge, W. Govaerts, and Y. A. Kuznetsov, "MATCONT: a MATLAB package for numerical bifurcation analysis of ODEs," *ACM Trans. Math. Softw. TOMS*, vol. 29, no. 2, pp. 141–164, 2003.

[72] J. Ohtsubo, *Semiconductor lasers: stability, instability and chaos*, vol. 111. Springer, 2012.

[73] S. Wieczorek, B. Krauskopf, T. B. Simpson, and D. Lenstra, "The dynamical complexity of optically injected semiconductor lasers," *Phys. Rep.*, vol. 416, no. 1–2, pp. 1–128, Sep. 2005, doi: 10.1016/j.physrep.2005.06.003.

[74] M. Dillane, B. Lingnau, E. A. Viktorov, I. Dubinkin, N. Fedorov, and B. Kelleher, "Asymmetric excitable phase triggering in an optically injected semiconductor laser," *Opt. Lett.*, vol. 46, no. 2, pp. 440–443, 2021.

[75] N. Soures and D. Kudithipudi, "Spiking Reservoir Networks: Brain-inspired recurrent algorithms that use random, fixed synaptic strengths," *IEEE Signal Process. Mag.*, vol. 36, no. 6, pp. 78–87, 2019.